A Single-Photon Source for Quantum Networking

Jerome Dilley
Exeter College, Oxford



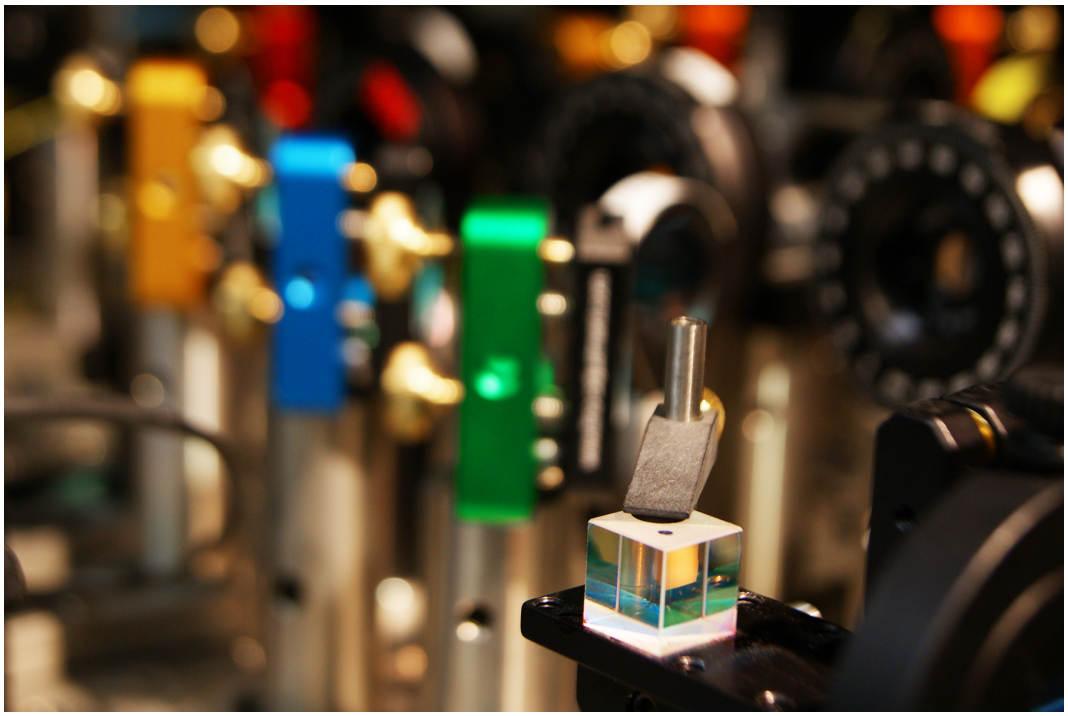
Submitted for the degree of Doctor of Philosophy
Hilary Term 2012

Supervised by
Dr. Axel Kuhn

Clarendon Laboratory
University of Oxford
United Kingdom

Abstract

Cavity quantum electrodynamics (cavity QED) with single atoms and single photons provides a promising route toward scalable quantum information processing (QIP) and computing. A strongly coupled atom-cavity system should act as a universal quantum interface, allowing the generation and storage of quantum information. This thesis describes the realisation of an atom-cavity system used for the production and manipulation of single photons. These photons are shown to exhibit strong sub-Poissonian statistics and indistinguishability, both prerequisites for their use in realistic quantum systems. Further, the ability to control the temporal shape and internal phase of the photons, as they are generated in the cavity, is demonstrated. This high degree of control presents a novel mechanism enabling the creation of arbitrary photonic quantum bits.



Publications

[∗ denotes equal contribution]

P.B.R. Nisbet-Jones*, **J. Dilley***, A. Holleczek, O. Barter, A. Kuhn. "Quantum Homodyning of Photonic Qubits, Qutrits and Ququads Emitted on Demand from an Atomic Source" [arXiv:1203.5614v1], (2012)

J. Dilley, P.B.R. Nisbet-Jones, B.W. Shore, A. Kuhn. "Single-Photon Absorption in Coupled Atom-Cavity Systems" *Phys. Rev. A* **85** 23834, (2012)

P.B.R. Nisbet-Jones*, **J. Dilley***, D. Ljunggren, A. Kuhn. "Highly Efficient Source for Indistinguishable Photons of Controlled Shape" *New Journal of Physics* **13** 103036, (2011)

M. Himsworth, P.B.R. Nisbet, **J. Dilley**, G. Langfahl-Klabes, A. Kuhn. "EIT-based quantum memory for single photons from cavity-QED" *Applied Physics B* **103** (3) 579-589, May 2011.

Acknowledgements

First and foremost, thanks must be given to Axel for his unwavering patience, excellent guidance and encyclopedic knowledge. Peter Nisbet, one of my contemporaries, deserves great credit and thanks, as it was he with whom I worked very closely in building the experiment. Postdocs Daniel Ljunggren (who helped greatly in the initial stages of this work), Matt Himsworth and Genko Vasilev all contributed significantly. Finally, thanks to the new students Annemarie Holleczek and Oliver Barter, who have been brave enough to take over the apparatus.

Contents

1 Introduction **1**

2 Atom-Cavity Interactions **7**
2.1 Coupled Atom-Cavity Systems 8
2.1.1 Light-Matter Interactions and Cavity Quantisation 8
2.2 Atom-Cavity Interactions 9
2.2.1 The Jaynes-Cummings Model 9
2.2.2 The Three Level Atom 12
2.2.3 Photon Emission from the Atom-Cavity System 13

3 Recipe for an ^{87}Rb Atom-Cavity System **15**
3.1 The Magneto-Optical Trap 16
3.2 Experimental Overview 17
3.2.1 Laser Locking Scheme 17
3.2.2 Laser Set-Up 18
3.3 Vacuum Chamber 18
3.3.1 Magnetic Field 20
3.3.2 Compensation Coils 21
3.3.3 Rubidium Source 22
3.3.4 Atomic Fountain 22
3.3.5 Experimental Control 24
3.4 High-Finesse Cavity 25
3.4.1 Cavity Locking 26

4 Single Photons from a Coupled Atom-Cavity System **28**
4.1 Single-Photon Production 28
4.2 Optimisation of the Photon Source 29
4.2.1 Launch Velocity 29
4.2.2 Pump Beam 29
4.2.3 Zeroing of the Magnetic Field 31
4.3 Correlation Measurements 32
4.4 Photon Statistics in Experiment 34
4.4.1 Dark Count Subtraction 35
4.4.2 Conditioning on Single Atoms 36

4.4.3 Discriminated Data . . . 39
4.4.4 Photon Production Efficiency . . . 40
4.5 Indistinguishability . . . 41
4.5.1 Two-Photon Interference . . . 42
4.5.2 Time-Resolved Two-Photon Interference . . . 43
4.5.3 Well-Defined Frequency Offset . . . 45
4.5.4 Jitter . . . 46
4.6 Demonstrating Indistinguishability with Real Photons . . . 47
4.7 The Quantum Beat between Two Photons . . . 51
4.8 Conclusion . . . 53

5 Photon Shaping **54**
5.1 Photon Shaping . . . 54
5.2 Efficiency . . . 57
5.3 Variation of g . . . 58
5.4 Experimental Verification . . . 59
5.5 Conclusion . . . 62

6 Phase **63**
6.1 Two-Photon Interference with Variable Phase . . . 64
6.2 Results . . . 65
6.2.1 Qubits . . . 65
6.2.2 Fidelity . . . 69
6.2.3 Qutrits . . . 70
6.2.4 Ququads . . . 73
6.3 Conclusion . . . 73

7 Single-Photon Absorption **76**
7.1 Input-Output Coupling . . . 77
7.2 Impedance Matching . . . 78
7.3 Single-Photon Absorption . . . 79
7.3.1 Quantum Memory . . . 82

8 Outlook **84**
8.1 Outlook . . . 84

A Photons of Alternating Polarisation **87**
A.1 Photons of Alternating Polarisation . . . 87

List of Figures

2.1 Levels scheme showing states involved in the single photon production. 7
2.2 Ideal cavity transmission for a Fabry-Pérot type cavity. 9
2.3 Atom-cavity coupling and decay rates 11

3.1 ^{87}Rb levels scheme. 17
3.2 Laser schematic 19
3.3 AOM driver electrical schematic 20
3.4 An illustration of the vacuum chamber and cavity 21
3.5 Atomic desorption and loading rates 22
3.6 Image of the ^{87}Rb MOT with circa 10^7 atoms. 23
3.7 Fountain velocity 24
3.8 High-finesse optical cavity 25
3.9 Cavity locking beam and cavity output 26
3.10 Atomic fountain and optical cavity 27

4.1 The experimental sequence for producing single photons 29
4.2 Atom cloud interaction times 30
4.3 Pump beam position 30
4.4 Magnetic sub-level contributions to the photon production 31
4.5 Photon statistics 33
4.6 Visualisation of photon stream distributions 33
4.7 Hanbury Brown and Twiss interferometer 34
4.8 Experimentally measured cross-correlation function for a Hanbury Brown and Twiss-type interferometer 35
4.9 Single atom transits of the optical cavity 37
4.10 Relative photon and dark count distributions 38
4.11 Retrieval of the sub-Poissonian nature of the single photon source. . 40
4.12 Comparative $g^{(2)}(\tau)$ cross-correlation plots 40
4.13 A $g^{(2)}(\tau)$ correlation function calculated with a rolling filter. 41
4.14 Two photon interference on a beam splitter. 43
4.15 Two-photon coincidences for photons of different frequencies 45
4.16 Joint detection probability for photons with frequency jitter 46
4.17 A schematic of the HOM interferometer. 48
4.18 Calibration of the repetition rate. 48

4.19 HOM interference of identical single photons 49
4.20 Experimentally measured correlation plots for parallel and perpendicular polarised photons. 50
4.21 Levels schematic depicting the potential variation in photon frequency. 52
4.22 HOM interference of photons with differing frequencies. 52

5.1 Analytically calculated driving pulses for a selection of photon shapes 57
5.2 Variation in driving pulse with specified efficiency 58
5.3 Variation in photon shape as a function of g 59
5.4 Experimental photon shaping results I 60
5.5 Experimental photon shaping results II 61

6.1 Twin-peak time bins 64
6.2 Experimentally measured $\Omega(t)$ phase 66
6.3 Two photon interference for photons with applied phase 67
6.4 Normalised peak height as a function of phase 68
6.5 Equivalent quantum circuit for twin-peak photons 69
6.6 Twin peak photon bar charts. 69
6.7 Triple peak photons and calculated driving pulse 70
6.8 Triple peak photon with relative phases 71
6.9 Equivalent circuit for the time-resolved two-photon interference of triple peak photons. 72
6.10 Triple peak photon bar charts 72
6.11 Quad peak photon correlations 74

7.1 Depiction of the quantum internet 76
7.2 Coupling Schemes 77
7.3 Single-Photon Absorption 80
7.4 Rabi frequency, $\Omega(t)$ as a function of t and ρ_0. 81
7.5 Quantum State Mapping 82
7.6 Atomic State Populations 83

8.1 Single Photon absorption schematic 85

A.1 Count rate with pump frequency for sequential photon generation . 88

Chapter 1

Introduction

> Consequently he who wishes to attain to human perfection, must therefore first study Logic, next the various branches of Mathematics in their proper order, then Physics, and lastly Metaphysics. **Maimonides**

Thomas Kuhn posited that paradigm shifts occur when revolutionary scientific ideas replace existing hegemonies, heralding the inception of novel scientific frameworks [1]. It is through this very mechanism that science indefatigably progresses and the scientific method advances. Quantum mechanics is regarded as an archetypal scientific paradigm, and is presently driving a revolution in the way with which we deal with information. This new conceptual framework is known as quantum information processing (QIP) and is a burgeoning area of contemporary physics.

The research described in this thesis deals directly with QIP, and is concerned with the ultimate control over the fundamental building blocks of light and matter. Its foundations are deeply entrenched in quantum mechanics, with an ontology comprising single atoms and single photons. The conceptual beginnings of these photons, or light quanta, and indeed the beginnings of quantum mechanics, can generally be traced back to Einstein's annus mirabilis and his publication, "On a Heuristic Viewpoint Concerning the Production and Transformation of Light" [2]. Planck had, in 1900, posited that black-body radiation was emitted in discrete energy packets. Einstein, in seeking to explain the photoelectric effect, used this same idea and hypothesised that these quanta of light were capable of being absorbed and emitted only as wholes, with an energy dependant upon their frequency. Although making a very strong case for the validity of his hypothesis, it was, at inception, an idea almost universally rejected by the community at large. Evidence and opinion began to sway in favour of the light quanta hypothesis, however, and Einstein was ultimately awarded the Nobel Prize in 1921 "for his services to Theoretical Physics, and especially for the discovery of the law of the photoelectric effect". From this treatment of the indivisible nature of photons arose the the ideas of wave-particle duality: if one accepted Maxwell's electromagnetic wave theory *and* the existence of light quanta, then one's hand was forced into accepting that these quantum enti-

ties can exhibit both wave-like and particle-like behaviours. This became ever more apparent with de Broglie's seminal thesis ascribing wave-like properties to matter. In time, these ideas were more formally developed and subsumed into the newly emerging theory of quantum mechanics.

Experimentally, it was not until the late 1950s and the work of Hanbury Brown and Twiss that the field of quantum optics began to emerge, along with the possibility of probing the quantum mechanical nature of light more rigorously in the laboratory. The advent of the laser in the 1960s accelerated this process, and soon experimentalists were witnessing photon statistics which could only be suitably interpreted within the framework of quantum physics [3, 4]. This photon *anti-bunching*, investigated by examining the second-order intensity correlation function of a photon stream, $g^{(2)}(\tau)$, remains one of the litmus tests for those sources purporting to emit single photons. True single-photon states were not produced in the laboratory until 1986, when groups on both sides of the Atlantic achieved this feat simultaneously [5, 6].

At around this time, proposals for the exploitation of these quantum phenomena were made. The concept of 'quantum money' was first propounded in the 1970s, although it remained unpublished until 1983 [7]. In 1984, a protocol describing the transmission of random numbers using single photons was made [8], known as BB84. This seminal paper, amoung others, signalled the beginning of a new topic of research known as *quantum key distribution* (QKD), or *quantum cryptography*. QKD essentially strives to ensure secure communication between two parties, and as protocols have become more sophisticated, so too has experimental progress been rapid. Thus far, quantum keys have been transmitted successfully over optical fibers and through free space over long distances [9–11], with some real world networks in use [12] and commercial systems even available to purchase. See [13, 14] for reviews of the subject.

The establishment of a quantum network is a further topic of current research, and one which is very closely aligned to QKD. In QKD, the aim is simply to securely and robustly transmit keys for encryption, although it should actually be possible to transmit and process quantum information over some distributed network. Conceptually, a number of quantum systems might be connected together via some quantum 'channels', along which quantum information (encoded on single photons, for example) could be sent. The universal quantum nodes comprising the network could be used to generate, receive, store and process quantum information, with the quantum channels both transporting quantum states and distributing entanglement. The properties of such a system would differ greatly from those of its classical equivalent: quantum entanglement and non-local correlations would allow for dynamical phenomena currently unattainable in classical networks, with the added benefit of a state space increasing exponentially with the number of nodes. Further, quantum networks could also be used to simulate many-body systems [15].

There are a number of candidates purporting to be suitable for constituting such a network, with single atoms and single photons of particular interest at the current time. A seminal networking paper by Cirac et al. [16] proposed the use of neutral

atoms in optical cavities as the building blocks for QIP. In the proposal, the quantum state of an atom is mapped onto a photon, which transmits the quantum state over the network link to a second atom in a separate cavity. The absorption of the photon by the second atom completes the state mapping procedure.

The most fundamental unit of quantum information, the qubit, can generally be expressed by $|\psi\rangle = \alpha|0\rangle + \beta|1\rangle$, where $|0\rangle$ and $|1\rangle$ are the states of a two-level quantum system. In contrast to its classical analogue, the bit, the quantum bit can be in a superposition of its two basis states at the same time, a phenomena which is fundamental to quantum mechanics. Patently, a prerequisite for the establishment of a quantum network is the ability to map the quantum state of a single node, or stationary qubit, onto a flying qubit, the information carrier. Neutral atoms and optical photons offer myriad attractive qualities for these purposes. Optical photons are perhaps the best medium for transporting quantum information and entanglement over significant distances [10]: optical fiber technology is very mature, for instance, and they are potentially very robust against decoherence. They also offer a number of degrees of freedom in which it is possible to encode information, e.g. polarisation, time-bin and number state. Single atoms, meanwhile, may be isolated and trapped without too great an exertion, and offer the ability to store information for long periods of time. However, the relatively weak interaction between photons and single atoms in free space necessitates, in the general case, the use of an optical cavity. Not only does a cavity enhance the light-matter interaction, but it may also create a well-defined spatial mode into which the atom can emit.

The modification of the coupling of an atom to the electromagnetic continuum of free space modes was first documented by Purcell [17], who described how the rate of spontaneous emission could be altered if an atom was placed inside a resonant cavity. The Purcell effect is of great importance for the realisation of many single photon sources, as it allows for the efficient collection of photons emitted into a well-defined mode [18]. The probability of an atom emitting into the cavity mode can be greatly enhanced (by what is known as the *Purcell* factor), and if the cavity is sufficiently small, this probability can greatly exceed the likelihood that it emits into free space [19]. The regime in which a photon emitted from the atom can be reabsorbed before it decays from the cavity is known as the *strong coupling regime*. Mirrors with reflectivities capable of reaching the strong-coupling regime have only been available for a decade or two, and the field is one which is rapidly expanding with new technological capabilities. The challenge which so presents itself is thus often that of isolating single atoms and locating them in the mode of a sufficiently small optical cavity, resonant with the atomic transition. Once this is accomplished, one is charged with the task of deterministically controlling the interaction between the two. This thesis deals with the establishment of both of these criteria: building a deterministic atom-cavity system, and attempting to control completely its coherent dynamics during both the emission and absorption of single-photon wavepackets.

Up until this point, good progress has been made experimentally toward implementing the constituents of a quantum network: entanglement mapping mediated by photons with atomic ensembles [20, 21], cavity QED atom-photon state mapping

[22–24], single-atom single-photon absorption in ion traps [25] and single-photon absorption by a coupled atom-cavity system [26, 27] have all been demonstrated. The transmission of entanglement and quantum teleportation have also been demonstrated over long distance free space channels [28, 29], albeit without using atom-cavity systems. In addition, the first recent demonstration of the interface between a photon and solid-state qubit has recently been documented [30]. Very recently, an elementary network consisting of two atoms was demonstrated [31], paving the way for future networks of increasing complexity.

At the heart of any realistic network are likely to be quantum repeaters. Any long-distance communication will have a significant inherent attenuation of signal, and, because the *no-cloning theorem* forbids the copying of unknown quantum states, the possibility of the standard amplification of states is negated. In deference to this fundamental aspect of quantum mechanics, quantum repeaters posit the utilisation of *entanglement swapping* to create a chain of nodes, which, taken together, allow quantum state transfer over long distances. For a recent review, see [32]. Many possible implementations of these repeaters incorporate quantum memories in atomic ensembles [33, 34, 34, 35], with proposals existing for the conjunction of atom-cavity systems and EIT based memory schemes [36]. Storage times for light pulses exceeding 200 ms have been demonstrated for ultracold atoms [37]. The possibility of implementing such a scheme with the current source is discussed at the end of this thesis.

Initial proposals regarding computation based on the tenets of quantum mechanics were put forward by Feynman [38] and Benioff [39]. Feynman was contemplating the simulation of physics using quantum computers, and noted that classical computers simulate these problems in an exponentially long time. Deutsch developed these ideas and posited the possibility of a universal quantum computer [40]. At the heart of the quantum computer lie the phenomena of entanglement and superposition, whose capacity to solve certain problems much more quickly can be thought of as a result of quantum parallelism. Essentially, information may be encoded in the state of a quantum system and a series of operations (or gates) carried out in the form of a sequence of controlled interactions. It was soon shown that the ability to manipulate two qubits simultaneously is a *sufficient* requirement for the implementation of a universal quantum computer [41]. For a current overview of the field, see [42].

There have been a number of proposed algorithms which could be run on a quantum computer and which could offer exponentially quicker solutions to certain problems than their fastest classical counterparts; that proposed by Deutsch and Jozsa was perhaps the first [43]. Grover's search algorithm [44, 45] was proposed in 1996 and promised a quadratic gain in speed for searching an unsorted database. Shor's algorithm [46] deals with integer factorisation, and is well known for the promise of its ability to be able to crack RSA encryption, given a large enough quantum computer. In fact, experimental realisations of the algorithm have been implemented in NMR [47] and photonic systems [48–50], albeit managing only to factor the number 15.

There are, unsurprisingly for a field still in its infancy, a number of contenders and proposals for how to physically implement a quantum computer. Cirac and Zoller proposed a scheme for quantum computing using trapped ions in 1995 [51], with interactions between the ions mediated by phonons. Schemes to implement fast quantum gates using trapped neutral atoms have also been proposed [52]. Arrays of trapped neutral atoms [53–55] also exhibit great potential as a physical system for quantum computing. Other contenders include low temperature superconducting qubits [56], quantum dots, ultracold quantum gases and NMR.

Thus far one of the most successful physical architectures for quantum computation is the use of trapped ions, where quantum gates have been demonstrated by a number of groups [57–59], and up to eight trapped atoms have been entangled in a single trap [60]. Segmented ion traps promise to circumvent the difficulties associated with scaling in the more traditional traps [61, 62], and also permit the deterministic shuttling of ions from place to place, a feature potentially very useful for generating deterministic interactions between ions. Quantum simulations have also been demonstrated with the use of trapped ions [63]. A review of the whole field is found in [64], with a review of ion based quantum simulations given in [65].

One field which has generated particular interest in recent times is all-optical quantum computing. It was shown in 2001 [66] that linear optical elements, coupled with feed-forward, are sufficient to perform quantum computation with photons. In this linear optics quantum computing (LOQC), photons are used to encode qubits, with linear elements (such as beam splitters and waveplates) used to perform gate operations. The original proposal has been supplanted by numerous others requiring significantly fewer resources [67, 68], with a number of experiments showing the implementation of quantum gates. A particularly attractive feature of LOQC is the promise of the ability to integrate the requisite optical elements and detectors onto monolithic chips [50, 69–71]. In this way, it should be possible to write entire quantum circuits onto single chips using existing and mature technology, promising excellent scalability and performance. The potential for the integration of atom-cavity based single-photon sources and integrated quantum circuit technology is somewhat attractive.

This thesis demonstrates the realisation of one of the building blocks of quantum networking, in the form of a strongly coupled atom-cavity system with the ability to produce single photons. A single atom in the cavity represents a single stationary node of a quantum network, and careful control over the atom-cavity interaction allows for the production of single photons with highly tailorable properties - ideal for use as flying qubits within a quantum network, or within LOQC. The system is based upon a cold atom source and high-finesse optical cavity, with atoms launched upwards from a magneto-optical trap (MOT) using an atomic fountain. The zenith of the atom cloud's position intersects with the cavity mode, a mechanism intended to lengthen the atom-cavity interaction time without introducing perturbative atom traps. Single photons are then generated from the system by applying successive laser pulses to the atom as it interacts with the cavity mode. The thesis is laid out as follows:

Chapter 2 describes the theoretical foundations of the atom-cavity system. The basic interaction between a single atom and single photon in an optical cavity is explored, and the principles behind the photon production process explicated. **Chapter 3** then describes the necessary experimental constituents of the atom-cavity system, with a recipe for its construction. Characterisation of the photon source is described in **Chapter 4**, with the single-photon nature of the emission and the indistinguishability of the photons being investigated. It is shown that long interaction times ($t > 100\,\mu$s) can be achieved, along with a high photon production efficiency ($\approx 85\%$). An experiment detailing the generation of photons with arbitrary temporal shape is then demonstrated in **Chapter 5**, along with the corresponding analytical recipe. It is shown that it is possible to precisely tailor the amplitude of the photon wave packets during the emission process, through careful control of the time-varying control field used to drive the STIRAP process. Attention in **Chapter 6** is then turned to control over the relative phase within a single photon wave packet. Using the same experimental set-up used to test indistinguishability, single-photon quantum homodyning is employed. The first results demonstrating the ability to control the phase of single photons during the production process are presented. Together with the photon shaping, this represents a novel method for the production of arbitrary photonic qudits from atom-cavity systems. **Chapter 7** then addresses the situation of single-photon absorption by a single atom coupled to the cavity. An analytical method is developed, following the photon shaping mechanism [72], which ensures full impedance matching when absorbing a single photon of arbitrary temporal shape by the atom-cavity system. Finally, **Chapter 8** places the work in some perspective, and contemplates the future direction of similar endeavours.

Chapter 2

Atom-Cavity Interactions

This chapter describes the theoretical basis of the experimental atom-cavity system described later in this thesis. The atom-cavity system consists of a pseudo-three-level atom interacting with the electromagnetic field mode inside an optical cavity, driven by some classical laser light field. Before embarking on a detailed theoretical description of the 'photon pistol', it is perhaps appropriate to include a short precis of its operating principles (illustrated in Fig. 2.1).

The single photon generation technique to be explicated here is based upon a coherent Raman process, and was pioneered by Kuhn et al. [73–75]. It is known as vacuum-stimulated Raman adiabatic passage, or V-STIRAP, and in contrast to standard STIRAP (where one has control over the time-varying amplitudes of both the pump and the Stokes laser), V-STIRAP utilises the bare mode of a high finesse optical cavity to couple one of the branches of the Raman transition. The three

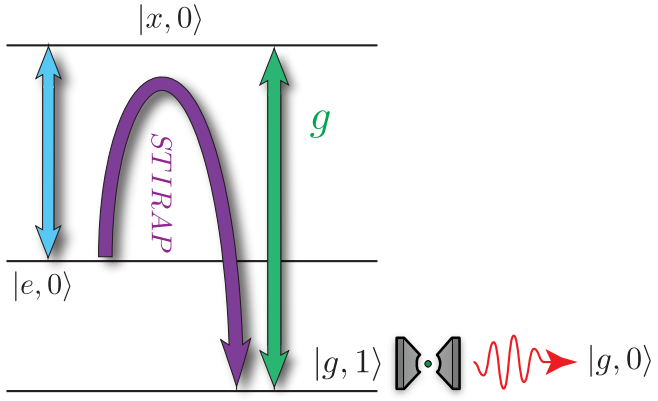


Figure 2.1 Levels scheme showing states involved in the single photon production.

atomic levels may consist of two electronically stable ground states and one electronically excited state. One of the ground states is coupled to the excited state by an optical cavity with coupling strength $2g$, and the other via a laser pulse with Rabi

frequency $\Omega(t)$. The cavity and the laser pulse are generally co-resonant to achieve Raman resonance although there may be some joint detuning from the excited state. If the atom-cavity system is initialised in one of the ground states with no photon in the cavity mode, the application of some properly chosen time-varying control field can coherently transfer the atom between ground states without populating the excited state. This population transfer results in the creation of one and only one photon in the cavity mode, which is then emitted from the cavity.

Firstly in this chapter then, a brief description of optical cavities is given, and some of their key parameters are introduced. A model of the interaction between a single atom and an electromagnetic cavity field mode is then introduced in the form of the ubiquitous Jaynes-Cummings model. Following this, the extension of the model to three-level atoms is described in section 2.2.2, and the mechanism for the production of single photons (based on stimulated Raman adiabatic passage) is then explicated.

2.1 Coupled Atom-Cavity Systems

2.1.1 Light-Matter Interactions and Cavity Quantisation

Let us briefly consider the optical cavity before progressing any further onto the dynamics of the atom-cavity system. One of the primary roles of the cavity is to enhance the interaction between light and matter. A Fabry-Pérot type optical cavity will generally consist of two reflecting surfaces, either curved or flat, which will only support the transmission of light of particular frequencies. The condition for transmission is that the wavelength of light impinging on the cavity is such that the small fraction of light not reflected from the first mirror circulates inside the cavity and sums constructively in phase to ensure transmission through the cavity. This effect increases the intensity of any beam at resonance inside the cavity by some factor relating to the reflectivities of the mirrors.[1]

The mirrors may be curved to aid the stability of the cavity (i.e. to ensure it supports only geometrically stable eigenmodes) and its alignment; those in the present apparatus have radii of curvature $R_{curv} = 50\,\mathrm{mm}$, which are much longer than the cavity length, $L = 75\,\mu\mathrm{m}$. We neglect consideration of the multiplicity of transverse Hermite-Gaussian and Laguerre-Gaussian modes which are possibly supported by such a cavity, and consider only the TEM_{00} mode with Gaussian profile.

The frequency separation between the adjacent axial modes supported by the cavity is known as the free spectral range, and is given by $\Delta\omega_{fsr} = 2\pi.\frac{c}{2nL}$, with n the refractive index and L the cavity length. For simplicity, we shall consider a cavity with mirrors of equal reflectivity, $R_1 = R_2 = 1 - T_{1,2}$. The finesse of the

[1] This factor has a maximum given by $\mathcal{T}/(1-R)^2$, where $\mathcal{T}$ is the mirror transmissivity and R the reflectivity, and can be larger than 10^5 for modern mirrors of suitable quality.

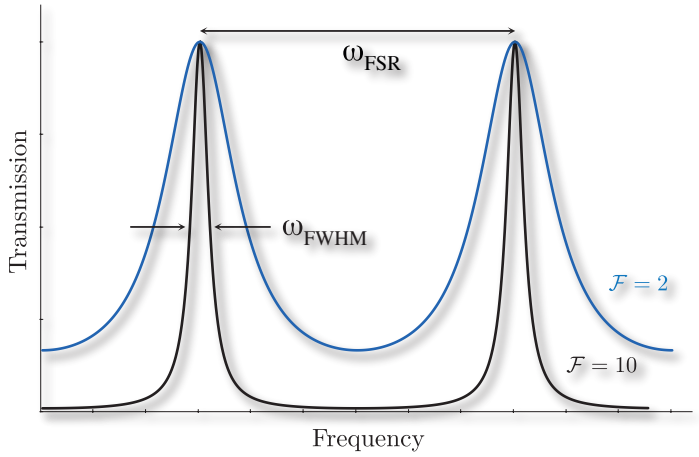


Figure 2.2 Ideal cavity transmission for a Fabry-Pérot cavity.

cavity is then defined as

$$\mathcal{F} = \frac{\pi\sqrt{R}}{(1-R)}, \tag{2.1}$$

from which we can obtain the full width at half maximum (FWHM) of the Lorentzian transmission peak, 2κ, around resonance:

$$2\kappa = \frac{c\pi}{L\mathcal{F}} = \frac{\Delta\omega_{fsr}}{\mathcal{F}}. \tag{2.2}$$

Fig. 2.2 demonstrates these parameters.

2.2 Atom-Cavity Interactions

2.2.1 The Jaynes-Cummings Model

It is instructive to now examine the description of the interaction between the cavity field mode and an atom. The simplest possible situation we can envisage is that consisting of the dipole approximation and a two level-atom at rest, interacting with a single electromagnetic field mode. We take the atom to have ground and excited states denoted by $|g\rangle$ and $|x\rangle$ respectively, connected by an electric dipole transition with a transition moment given by μ and a transition energy of $\hbar\omega_{xg}$. The single cavity mode with which the atom interacts has a resonance frequency given by ω_c. The cavity field is quantised, and can in general be described by a superposition of photon number states $|n\rangle$. As this leads to a set of states spaced equally in energy, we may treat the mode as a quantum harmonic oscillator. The interaction between the quantised light field and atom is described by the eponymously named Jaynes-Cummings Hamiltonian [76]:

$$H = \hbar\omega_c\hat{a}^\dagger\hat{a} + \hbar\omega_{xg}\sigma_+\sigma_- + \hbar g_0(\hat{a}^\dagger\sigma_- + \sigma_+\hat{a}). \tag{2.3}$$

The first term in the above expression describes the cavity field Hamiltonian, with photon annihilation and creation operators $\hat{a}$, $\hat{a}^\dagger$ obeying the canonical commutation relation

$$[\hat{a}, \hat{a}^\dagger] = 1. \tag{2.4}$$

It is worth noting that the formalism here is for a lossless cavity, i.e. one constructed with perfect mirrors with reflectivities equal to unity. With n photons in the cavity mode the total energy is given by $\hbar\omega_c(n + \frac{1}{2})$, and thus the cavity field Hamiltonian is given by

$$H_C = \hbar\omega_c \left(\hat{a}^\dagger\hat{a} + \frac{1}{2}\right), \tag{2.5}$$

which simplifies to

$$H_C = \hbar\omega_c\hat{a}^\dagger\hat{a} \tag{2.6}$$

upon dropping the zero-point energy term.

The second term describes the atomic Hamiltonian in a formulation analogous to the photonic annihilation and creation operators. The atomic raising and lowering operators are defined as:

$$\begin{aligned} \sigma_+ &= |x\rangle\langle g| \\ \sigma_- &= |g\rangle\langle x|. \end{aligned} \tag{2.7}$$

This atomic Hamiltonian can also be expressed in terms of the projection operators for the excited and ground states as $\hbar\omega_{xg}(|x\rangle\langle x| - |g\rangle\langle g|)/2 = \hbar\left(\omega_x|x\rangle\langle x| + \omega_g|g\rangle\langle g|\right)$, where the energy difference between the ground and excited states of the atom is given by $\hbar\omega_{xg}$.

The third term in the Hamiltonian describes the interaction between atom and cavity mode. The reference frame of the system has been translated to one rotating at the laser frequency ω_c, and the *rotating wave approximation* has been made: terms oscillating very rapidly in the Hamiltonian have been neglected, i.e. those corresponding to $\sigma_+\hat{a}^\dagger$ and $\sigma_-\hat{a}$ which rotate at roughly twice the optical frequency. It is apparent from the interaction terms that the cavity photon number and atomic state are indubitably linked; the atom moving from the ground to the excited state and vice versa is accompanied by the corresponding annihilation or creation of a single photon in the cavity mode.

The parameter g describes the atom-cavity coupling rate. At an antinode of the cavity, it can be be well described by:

$$g_0 = \sqrt{\frac{\omega_c}{2\epsilon_0 V\hbar}}\mu_{ge}. \tag{2.8}$$

The position dependent form of the atom-cavity coupling can be expressed as $g(\mathbf{r}) = g_0\, f_{cav}(\mathbf{r})$, where $f_{cav}(\mathbf{r})$ represents the electric field distribution of the mode inside the cavity. For the situation when there is exactly one quantum of excitation in the atom-cavity system, the rate at which the energy is coherently exchanged between the atom and the cavity field is given by $2g$, the single-photon or vacuum Rabi

frequency.[2] Obviously, an atom moving through the cavity (as is the case for the experiment here presented), will experience a range of coupling strengths from $g = 0 \longrightarrow g_0$. For the timescale of production of a single photon however ($\approx 1\mu s$), the atom is treated as a stationary object experiencing only a fixed value of g.[3]

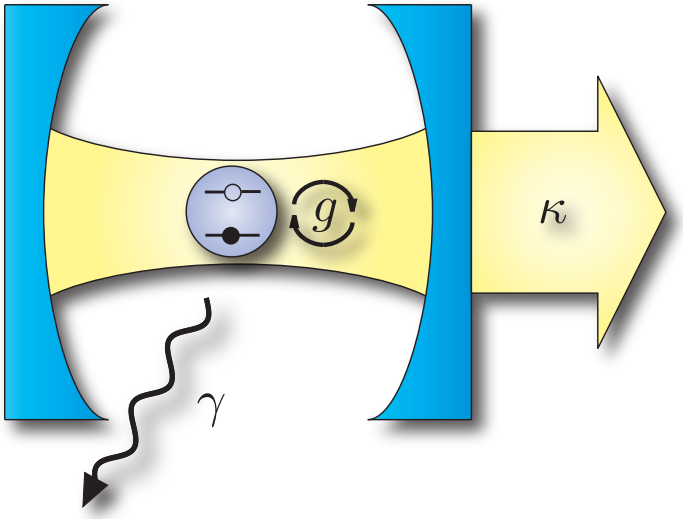


Figure 2.3 Atom-cavity coupling with the relevant g, κ and γ parameters.

The Jaynes-Cummings Hamiltonian can thus be written as the combination of the non-interacting atom and cavity field, $H_0 = \hbar\omega_c\hat{a}^\dagger\hat{a} + \hbar\omega_{xg}\sigma_+\sigma_-$, and the interaction Hamiltonian, $H_I = \hbar g_0(\hat{a}^\dagger\sigma_- + \sigma_+\hat{a})$. The eigenstates of H_0 are constructed simply from the atom and cavity states, with the energies of the new eigenstates simply a summation of their constituents. The interaction, however, results in a new set of eigenstates describing the full system, known as dressed states. The eigenfrequencies of the total Hamiltonian can be discerned, and are given by

$$\omega_n^{\pm} = \omega_c\left(n + \frac{1}{2}\right) + \frac{1}{2}\left(\Delta_C \pm \sqrt{4ng_0^2 + \Delta_C^2}\right), \tag{2.9}$$

where $\Delta_C = \omega_{xg} - \omega_c$ is the detuning between the atom and the cavity. The ground state energy is given simply by $\frac{1}{2}\hbar\omega_c$, whilst it is clear that states with $n \geq 1$ have eigenenergies which form a ladder of doublets. The splitting of these doublets is given by $\Omega_{eff} = \sqrt{\Omega_R^2 + \Delta_C^2}$.

[2] The atom-cavity coupling for higher quanta of excitation states is given by $\Omega_R = 2\sqrt{n}g(\mathbf{r})$.

[3] Justification for this assumption, and further discussion of the implication of variations in the atom-cavity coupling are presented in section 5.3.

2.2.2 The Three Level Atom

It is now pertinent to extend the basic Jaynes Cummings model to describe a three level Λ-type atom interacting with the optical cavity. We introduce an $|e\rangle \leftrightarrow |x\rangle$ transition with transition frequency ω_{xe}, driven by a laser field with Rabi frequency $\Omega(t)$. The interaction Hamiltonian of the three level system is then given by

$$H_{int} = \frac{\hbar}{2}\left[2\Delta|e\rangle\langle e| + 2\Delta\hat{a}^\dagger\hat{a} - 2g_0(|x\rangle\langle g|\hat{a} + \hat{a}^\dagger|g\rangle\langle x|) - \Omega(t)\left(|x\rangle\langle e| + |e\rangle\langle x|\right)\right] \tag{2.10}$$

where $\Delta \equiv \omega_{xe} - \omega_L = \omega_{xg} - \omega_c$ is the Raman-resonant detuning from the excited state.

Solving to find the corresponding eigenfrequencies once again, we find

$$\omega^0 = -\Delta\omega^\pm = \frac{1}{2}\left(-\Delta \pm \sqrt{4g_0^2 + \Omega^2 + \Delta^2}\right), \tag{2.11}$$

with eigenstates given by:

$$\begin{aligned} |\phi^0\rangle &= \cos\Theta|e,0\rangle - \sin\Theta|g,1\rangle \\ |\phi^+\rangle &= \sin\Phi\sin\Theta|e,0\rangle - \cos\Phi|x,0\rangle + \sin\Phi\cos\Theta|g,1\rangle \\ |\phi^-\rangle &= \cos\Phi\sin\Theta|e,0\rangle + \sin\Phi|x,0\rangle + \cos\Phi\cos\Theta|g,1\rangle. \end{aligned} \tag{2.12}$$

The mixing angles of the states, Θ and Φ, are given by

$$\tan\Theta = \frac{\Omega}{2g_0}, \qquad \tan\Phi = \frac{\sqrt{4g_0^2 + \Omega^2}}{\sqrt{4g_0^2 + \Omega^2 + \Delta^2} + \Delta}. \tag{2.13}$$

It is immediately apparent that the state $|\phi^0\rangle$ contains no component of the state $|x,0\rangle$ and is therefore impervious to spontaneous emission. In the absence of a decay channel other than excited state loss, a system prepared in this state will therefore remain there indefinitely; it is thus often referred to as a 'dark state'. For the case when $\Omega = 0$, the dark state reduces to exactly equal the $|e,0\rangle$ state. The application of a non-zero Rabi frequency leads to some mixture of $|e,0\rangle$ and $|g,1\rangle$, and in the limit of $\Omega \gg 2g$, the state $|\phi^0\rangle \approx |g,1\rangle$. As discussed in section 2.2.3, it is possible, with a suitably chosen laser pulse with some time-dependent Rabi frequency $\Omega(t)$, to transfer the state of the atom from $|e,0\rangle$ to $|g,1\rangle$ without populating the excited state $|x,0\rangle$. This is achievable if the process is adiabatic, with the system remaining in the dark eigenstate throughout.

There has thus far been no consideration of any dissipative processes which might contribute to the system dynamics. Specifically, we have considered an unphysical lossless cavity and neglected the polarisation decay rate of the atom. Spontaneous emission from the excited state of the atom, γ (which can be thought of as the coupling of the atom to the continuum of free-space modes), and the decay rate (see Eq. (2.2)) of the cavity, κ, perspicuously serve to dampen any coherent Rabi oscillations the system might undergo. The addition of these non-unitary processes

necessitates a description of the system using the reduced density operator, $\hat{\rho}$, and Master equation formalism. The full description of this lies outside the scope of this thesis, although for completeness we include the resultant Master equation [77]:

$$\frac{d}{dt}\hat{\rho} = -\frac{i}{\hbar}\left[H_{int}, \hat{\rho}\right] + \mathcal{L}[\hat{\rho}]. \tag{2.14}$$

The Liouville operator, $\mathcal{L}$, describes the non-Hermitian dynamics, and can be written in Lindblad form as

$$\begin{aligned}\mathcal{L}[\hat{\rho}] = \gamma_{ex}((2|x\rangle\langle e|\hat{\rho}|e\rangle\langle x| - |e\rangle\langle e|\hat{\rho} - \hat{\rho}|e\rangle\langle e| \\ + \gamma_{eg}(2|g\rangle\langle e|\hat{\rho}|e\rangle\langle g| - |e\rangle\langle e|\hat{\rho} - \hat{\rho}|e\rangle\langle e| \\ + \kappa(2\hat{a}\hat{\rho}\hat{a}^\dagger - \hat{a}^\dagger\hat{a}\hat{\rho} - \hat{\rho}\hat{a}^\dagger\hat{a}).\end{aligned} \tag{2.15}$$

The relative rates of these decay processes and the atom-cavity coupling determine to a great extent the behaviour of the system. The regime which is of interest is that of *strong coupling*, in which the atom-cavity coupling parameter dominates over the other two decay rates, or more quantitatively, $g^2/\kappa\gamma \gg 1$. Any atomic emission into the cavity is then a *reversible* process, as a photon in the cavity mode may be reabsorbed by the atom before it decays from the cavity. The exchange of energy between the atom and the cavity mode may then continue, leading to Rabi oscillations. This regime of strong coupling can be compared to the situation of an atom in free space, where any atomic emission may not, in general, be reabsorbed by the atom, thus making the process irreversible. It is worth noting the conditions for adiabaticity [77], which can be expressed as

$$\frac{g^2}{\gamma} \gg \frac{d\Theta}{dt} + \frac{\kappa}{2}. \tag{2.16}$$

Essentially, a strong atom-cavity coupling is required, as is a slowly changing mixing angle of the dark state.

2.2.3 Photon Emission from the Atom-Cavity System

The relevant parameters for the cavity in the experimental set-up presented herein are $\{g, \kappa, \gamma\} = 2\pi \times \{15, 12, 3\}$ MHz, which put the atom-cavity system just into the regime of strong coupling. Generally speaking, stronger couplings lead to increased photon production efficiencies: the maximum possible production efficiency can be shown to be purely a function of the cavity cooperativity, $C = g^2/(2\kappa\gamma)$, and is given by:

$$\eta_{max} = \frac{2C}{2C+1}. \tag{2.17}$$

The relevant levels scheme is shown in Fig. 2.1. The Λ-type system is made up of two hyper-fine ground states and an excited hyper-fine state on the D_2 line. With an atom in the cavity mode and the system initialised in the state $|e, 0\rangle$ (the atom prepared in the $F = 2$ ground state), the application of a time-varying pump beam

transfers the population into the lower $F = 1$ ground state. The cavity decay rate, κ, happens on a much faster time-scale than the state transfer, entailing that the photon is immediately mapped out of the cavity upon its creation. The state $|g, 0\rangle$ is then decoupled from further evolution, i.e. the process inherently generates only a single photon, as any further application of the driving pulse leaves the system state completely unaffected. In order to prepare the system for another photon emission, the atom has to be driven from the $F = 1$ ground state to an excited state from which it can decay to the desired level.

Chapter 3

Recipe for an ^{87}Rb Atom-Cavity System

Contained in this chapter is a description of the ingredients required to build a single-atom, single-photon source. The entire source was built in conjunction with Peter Nisbet, with initial assistance from Daniel Ljunggren. It is based on a high-finesse optical cavity and single-atom source provided by a magneto-optical trap (MOT) and atomic fountain. Much of the source's operation is described in [78]. The fact that room temperature ^{87}Rb atoms have velocities of a few hundred metres per second means that some mechanism is needed to cool and localise single atoms, if they are to interact for any reasonable time with a cavity mode some tens of microns in width. The combination of MOT and atomic fountain was chosen as an experimental arrangement to allow for long atom-cavity interaction times with high single-photon production efficiencies and repetition rates. Previous experiments have often either dropped an atom cloud under gravity through the mode of the optical cavity, limiting the potentially achievable interaction times to a few tens of microseconds [79], or used intra-cavity dipole traps to localise a single atom within the cavity mode [77]. The latter is an attractive option because of the ability to controllably couple a single atom to the cavity for very long periods of time (many seconds, in some cases). However, the perturbations introduced by the trapping potentials serve to distort the atomic levels used in the photon production process (due to the Stark shift), and optical dipole traps often greatly increase the required experimental overhead and resources - there can be the requirement for additional laser cooling between photon emissions, for example, and both the photon production rate and efficiencies can be dramatically reduced.

It was therefore decided that the cavity should be located vertically above the atom-trap, with the atomic cloud launched upwards using a technique known as moving molasses. Fine control over the velocity of the fountain and the loading times of the MOT should allow for precise tunability of the atomic arrival statistics in the cavity. The optical cavity and MOT are housed inside an ultra-high vacuum chamber, with a background gas of rubidium provided by a dispenser and UV

desorption.

The first sections of this chapter put forth a short description of the magneto-optical trap, fountain and laser set-up, with the optical cavity briefly detailed in section 3.4. An overview of their synthesis and operation as a single photon source is then presented.

3.1 The Magneto-Optical Trap

The magneto-optical trap is a ubiquitous tool in contemporary physics laboratories, and has become the researchers' standard method for obtaining cold neutral atoms in the laboratory. It is indispensable as the basis for myriad experiments including atomic clocks, Bose-Einstein-condensates, cavity-QED and high-precision spectroscopy. First realised by Raab et al. [80] in 1987 (a decade before Chu, Cohen-Tannoudji and Phillips won their Nobel prizes for laser cooling), the MOT allows the trapping and cooling of greater than 10^8 neutral atoms to temperatures of around one hundred microKelvin.

A simplistic but none-the-less useful pedagogic model of the MOT considers the momentum transfer which occurs when an atom absorbs and re-emits a photon. An atom with transition frequency of ω_a, irradiated with monochromatic light of a frequency ω_l, will experience a scattering force equal to

$$F(v) = \hbar k \frac{\Gamma}{2} \frac{I/I_{sat}}{1 + I/I_{sat} + 4\frac{\delta^2}{\Gamma^2}} \tag{3.1}$$

where $\delta = \omega_l - \omega_a + kv$, Γ is the natural decay with of the excited transition, k the photon wave vector, and v the velocity of the atom [81]. The quantity δ describes the frequency detuning from the atomic resonance, given a Doppler shift kv. Detuning a laser beam to below the resonance frequency will ensure that any atom moving toward the laser will see the laser light Doppler-shifted into resonance and experience a force opposite to its direction of motion. An atom moving away from the light source will conversely be Doppler-shifted away from resonance. Arranging a pair of counter-propagating beams will therefore ensure that atoms will preferentially absorb photons from the beam towards which they are moving, resulting in a slowing force opposite to their direction of motion. Three pairs of counter-propagating beams will result in cooling along three orthogonal axes, known as an optical molasses [82].

The optical molasses, although providing a cooling mechanism, does not provide a position dependent trapping force. In order to create the trap, a spatially dependent quadrupole magnetic field is introduced. This is most often produced by a pair of circular coils arranged in an anti-Helmholtz configuration. Atoms at the centre of the trap will sit in the zero of the magnetic field. The quadrupole field ensures that atoms displaced from the zero point will experience a Zeeman shift in the cooling transition frequency, leading to splitting of the magnetic sub-levels. The coupling of the polarisation states of the cooling beams to the Zeeman sub-levels thus leads to a spatially dependent restoring force, whose vector points toward the centre of the trap.

3.2 Experimental Overview

3.2.1 Laser Locking Scheme

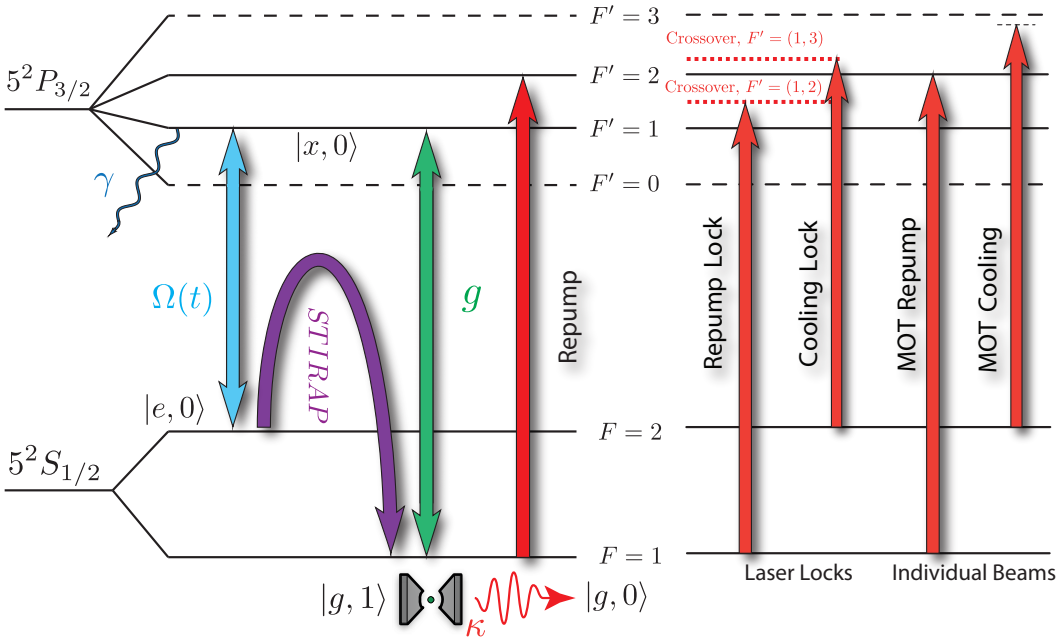


Figure 3.1 ^{87}Rb levels scheme. Left plot shows the levels involved in the photon generation, right plot shows the laser locks and MOT beams

The energy level structure of the ^{87}Rb D_2 line data is shown in Fig. 3.1. The $|F = 2\rangle \rightarrow |F' = 3\rangle$ transition is used for the cooling cycle, whose only decay channel is back to the $|F = 2\rangle$ level. However, there is a small probability that atoms will be excited to the $|F' = 2\rangle$ state from where they may decay into the dark $|F = 1\rangle$ state, which no longer interacts with the cooling laser. The 6.8 GHz hyper-fine splitting leads to the requirement for an additional laser to pump atoms on the $|F = 1\rangle \rightarrow |F' = 2\rangle$ transition. From the $|F' = 2\rangle$ level they decay probabilistically and may rejoin the cooling cycle. Thus, two lasers are required for the operation of the MOT, both of which are Toptica DL100 grating-stabilised external cavity diode lasers. The output of both lasers has significant asymmetry due to the topography of the diode facet, and has to be compressed in the horizontal axis to ensure a more rotationally symmetric beam. This is achieved through the use of anamorphic prism pairs and home-built beam profiling software to ensure maximum coupling efficiency for fibers, etc. Each laser is locked via saturated absorption spectroscopy to an ^{87}Rb vapour cell at room temperature.

To ensure that both the cooling and repump laser are running in a single frequency mode, we send around 5 mW of the beam to Fabry-Pérot interferometers,

fabricated in house. The Fabry-Pérots are constructed from two $R_{curv} = 100\,\text{mm}$ mirrors arranged in a confocal cavity. The two mirrors are attached via a piezo and Invar tube to allow scanning over several GHz using a function generator and a Piezomechanik SVR 150/3 high-voltage amplifier.

Saturated absorption spectroscopy allows for Doppler-free locking to the atomic resonances of rubidium in a vapour cell. The cooling laser is locked to the cross-over resonance $|F = 2\rangle \rightarrow |F' = 3 - 1\rangle$, while the repump is locked to the $|F = 1\rangle \rightarrow |F' = 2 - 1\rangle$ crossover. A schematic showing the laser locks and MOT beams is shown in Fig. 3.1. Both lasers are locked using Toptica Pound-Drever-Hall (PDH) modules, which add a 20 MHz modulation onto the laser supply current. The output of a fast photodiode is fed into the PDH module, creating an error signal which is input to a Proportional-Integral (PI) controller. The PI regulators are able to correct for long-term frequency drifts via adjustment of the feedback grating angle, and fast fluctuations via high-frequency modulation of the laser current, giving stabilisation to a linewidth of roughly 100 kHz.

3.2.2 Laser Set-Up

Separate acousto-optic modulators (AOMs) are used for the upper and lower cooling beams of the MOT, in order to facilitate control over the moving molasses-based atomic fountain. Each AOM is driven individually by homebuilt voltage-controlled oscillator (VCO)-based drivers (POS-100+/ POS-150+), which allow for tens of kilohertz in frequency precision and switching times on the order of $1\,\mu\,\text{s}$. The output of each driver (shown in Fig. 3.3) is sent through an RF amplifier (Minicircuits ZHL-1+, Motorolla CA2832C), giving approximately 1.6 W of power to drive the AOMs. The AOM shifted laser beams are coupled into 780 nm fibers to effectively decouple the laser and MOT optics and to provide a high degree of mode cleaning. The resulting MOT beams have a waist of $\omega = 3.5\,\text{mm}$ and a power of 5 mW per beam. A schematic of the laser set-up is shown in Fig. 3.2.

3.3 Vacuum Chamber

The high-finesse cavity and magneto-optical trap are all housed inside an ultra-high vacuum (UHV) chamber. This chamber is machined from non-magnetic stainless steel in an hexagonal configuration and is mounted vertically onto an optical table to ensure vibration isolation. Attached to the chamber are an ion getter pump, titanium sublimation pump and pressure gauge. There is additionally an ^{87}Rb dispenser and the requisite electrical feedthroughs needed for this and the cavity piezo. T-connectors and a four-way cross ensure that optical access is maintained through all sides of the hexagonal chamber. In order to reach UHV pressures (generally $< 10^{-9}$ mbar), the chamber and viewports must be rigorously cleaned and baked out to temperatures exceeding $\approx 150°\text{C}$ for a significant period of time. This bake-out serves to remove both water vapour and other contaminants present on the surface of the chamber walls and viewports. To achieve this, the bare chamber (with blank

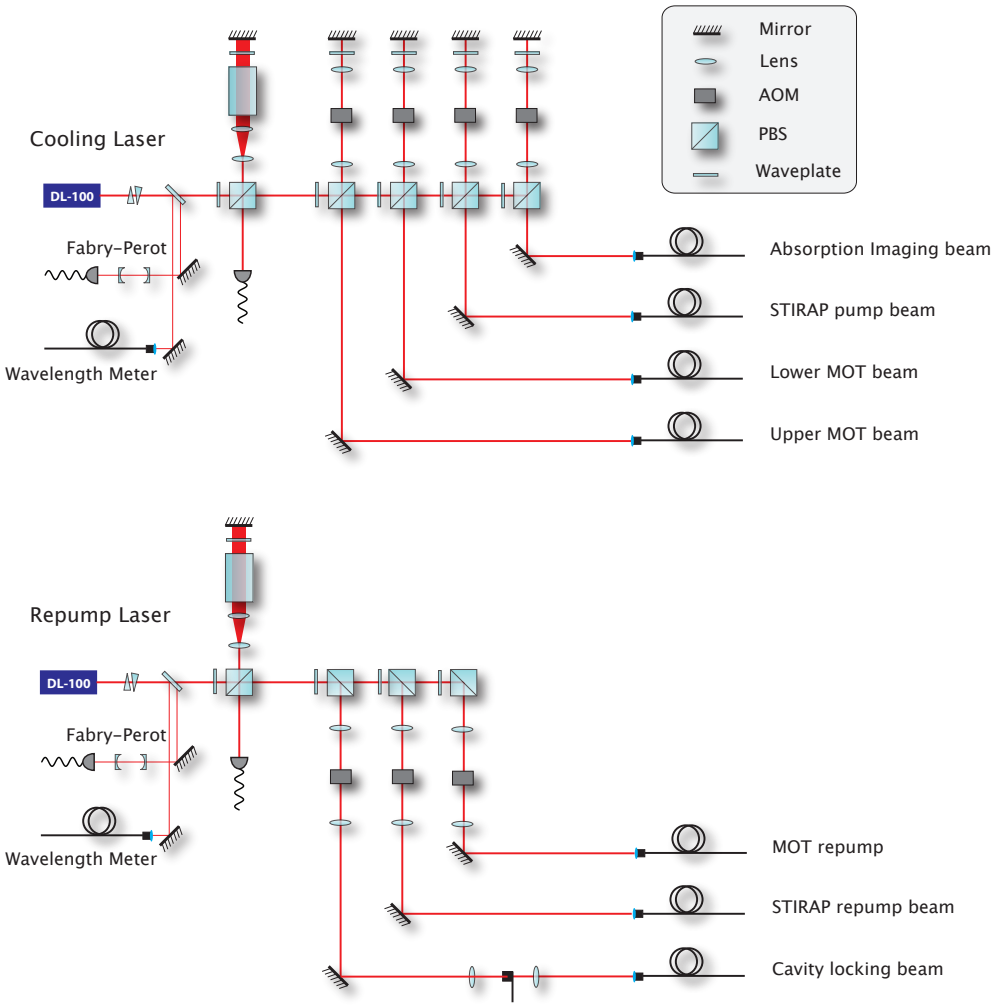


Figure 3.2 Schematic showing the laser set-up for the both diode lasers used in the experiment. The 'cooling laser' (upper) drives all of the transitions from the $|F = 1\rangle$ ground state, with the 'repump laser' (lower) driving all of those from $|F = 2\rangle$.

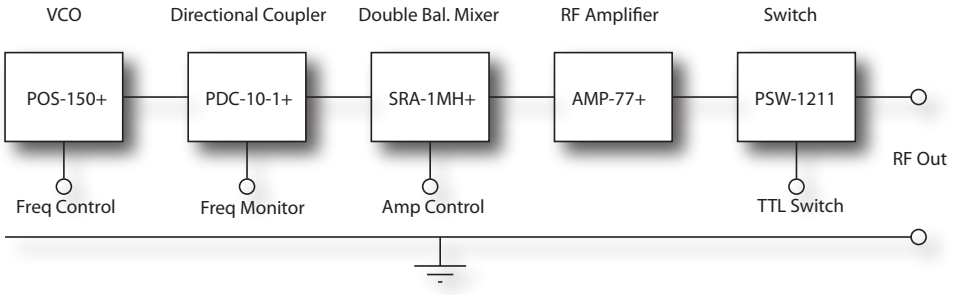


Figure 3.3 Schematic of the home-built AOM drivers. Depending on the VCO, the drivers can either output $50-100$ or $75-150$ MHz, with a modulation bandwidth of around 100 kHz. The double balanced mixer used in reverse allows for MHz switching rates of the RF output, whilst the PSW-1211 switch ensures the driver may be completely switched off if needed.

flanges present in place of viewports) was baked to a high temperature of 400°C for a number of weeks whilst attached to a turbomolecular pump. The chamber was then assembled with all pumps, gauges and viewports attached (minus the optical cavity) and baked again to a lower temperature of 200°C. After cooling, the ion getter pump was turned on and a pressure of 10^{-11} mbar obtained. The magneto-optical trap and fountain were then established, after which the chamber was opened again and the cavity and mount were installed. A tertiary bake-out was then performed. A diagram showing the arrangement of the chamber is shown in Fig. 3.4. The final pressure in the chamber (in the absence of rubidium provided by the dispenser) was around 10^{-10} mbar.

3.3.1 Magnetic Field

The magnetic field is produced by MOT coils which were fabricated in house, providing a field gradient of 0.8 G/cm/A. The coils are machined out of single pieces of aluminium, and are slotted to reduce possible eddy currents during switching of the magnetic fields. Due to the relatively high power dissipation in the coils and the sensitivity of the cavity stability to fluctuations in temperature, the coils require water cooling. This is achieved with a closed circuit CPU cooler, limiting the temperature of the coils and keeping it roughly constant to within around 0.5°C. The coil current is provided by a 20 A linear power supply (ELECTRO-AUTOMATIK EA-PS 3016-20), and is switched via a simple high-power MOSFET circuit, allowing turn off times on the order of 5 ms. A sensor monitors the coils' temperature in real time and switches off the coil current automatically should it exceed some pre-defined value.

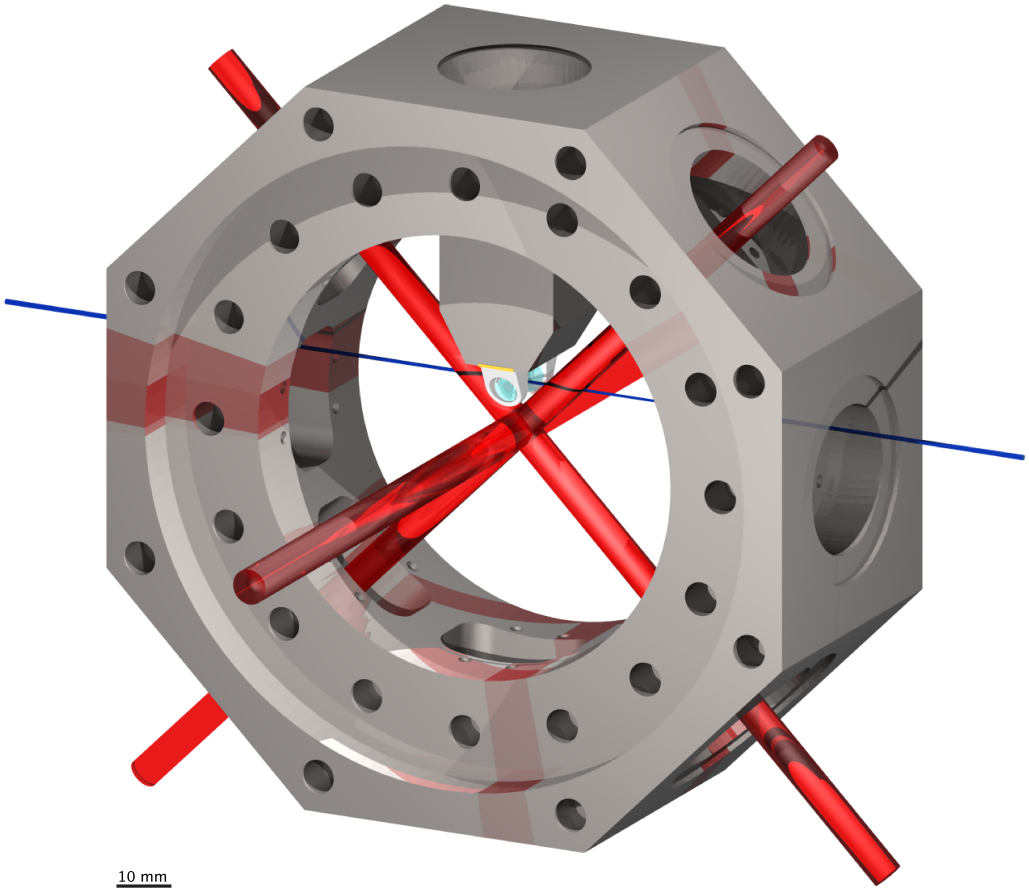


Figure 3.4 An illustration of the UHV chamber and cavity. The cavity mirrors sit on a special mount extending into the centre of the chamber. The beams for the MOT are shown in red, and the driving laser (which intersects with the cavity mode), in blue.

3.3.2 Compensation Coils

In order to compensate for the earth's magnetic field and stray fields in the laboratory, three separate pairs of compensation coils are placed on orthogonal axes around the vacuum chamber. In an ideal world, these coils would be arranged in an Helmholtz configuration to provide the most optimal magnetic field homogeneity. However, the region of interest inside the chamber that we would like to achieve good compensation for external fields covers roughly a cubic centimetre. Simulations show that a perfectly effective compensation field may be achieved over this region using coils which are arranged in a very un-Helmhotz-like configuration, but one that is very simple to implement experimentally. Thus, compensation in the X axis is provided by coils wrapped around the main MOT coil formas, whilst Y and Z directions are provided by small coils around the viewports on two axes of the

hexagonal (coil diameter $d = 80\,\text{mm}$, and separation $l = 180\,\text{mm}$).

3.3.3 Rubidium Source

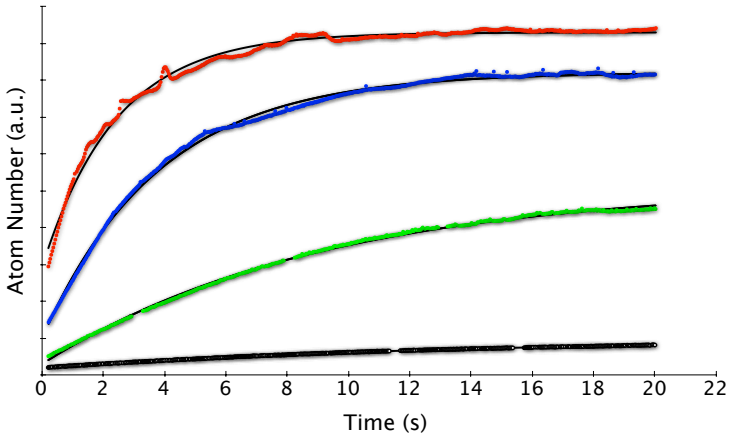


Figure 3.5 Atom number in the MOT, as measured by scattered fluorescence, for varying levels of intensity in the LIAD beam. For the {Black, Green, Blue, Red} plots, the intensity in the UV desorption beam is $I \approx \{0, 200, 300, 400\}\,\text{mW}$ respectively.

The MOT is loaded with the assistance of light-induced atom desorption (LIAD) [83, 84], which allows for fast loading of the trap coupled with rapid control over the amount of background ^{87}Rb in the UHV. The Rb in the chamber is provided by an Alvatec getter (Alvasource AS-5-Rb-160-S), and the UV light is provided through a number of high power 400 nm LEDs. A plot of the relative loading rates of the MOT for varying UV intensities is shown in Fig. 3.5. It is apparent that both the loading rate and atom number increase substantially in the presence of LIAD.

3.3.4 Atomic Fountain

The thermal rubidium atoms need to be initially cooled and trapped before they can be transported the 8 mm from the chamber centre to the cavity mode. To do this, atoms are loaded into the MOT for ≈ 200ms, after which the quadrupole MOT field is switched off and the atomic cloud held in a molasses for 10 ms. This molasses helps to further cool the atoms from the MOT and ensure that the magnetic field in the chamber has completely decayed. The frequency of the upper molasses beams is then detuned relative to that of the lower beams at a rate of 0.5 MHz/ms, cooling the atoms into a moving rest frame with a velocity given by:

$$v = \sqrt{2}\lambda\Delta f. \tag{3.2}$$

Here, λ is the wavelength of the laser and Δf the relative frequency difference between the upper and lower beams. The launch phase lasts for 20 ms, after which

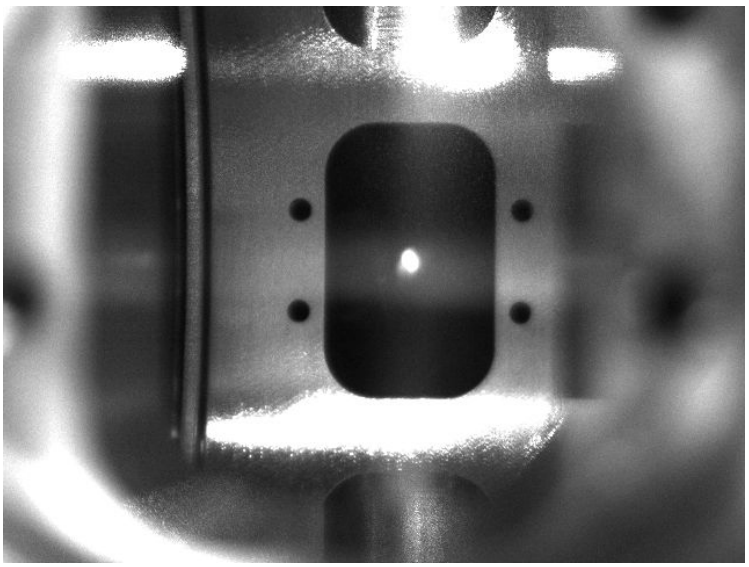


Figure 3.6 Image of the ^{87}Rb MOT with circa 10^7 atoms.

the molasses beams and repump are turned off entirely and the atoms released to continue ballistic trajectory toward the cavity. Taking a simple model of the atomic motion, we can see that the maximum possible interaction time is easily calculated for a given cavity mode diameter, d, as $t_{int} = 2\sqrt{2d/g}$, where g is the acceleration due to gravity: the maximum interaction time is thus approximately 4 ms for a 40 μm mode. However, given that the atom cloud has some initial finite spatial distribution and temperature, the achievable interaction times are limited in practice to a few hundred microseconds. The atomic fountain is very sensitive to variations in the intensities of the beams, as well as to their alignment and relative frequencies. Thus, the intensities of both the upper and lower beams are continually monitored after the output of their respective fibers by photodiodes (Thorlabs DET10A) whose output is read by a Labview control program via a data acquisition (DAQ) board. This ensures that the beam powers are stable to within a few percent. The frequencies of both AOM drivers can also be monitored via a frequency counter and RS232 interface with the main control computer, which again allows Labview to monitor the relative frequency difference between the upper and lower beams to within ≈ 1 kHz. Alignment of the atomic fountain and monitoring of the atom cloud trajectory is achieved through the use of absorption imaging, which relies on the atom cloud scattering light out of an on-resonance probe beam. A short, σ^+ polarised pulse, resonant with the cooling transition $|F = 2\rangle \rightarrow |F' = 3\rangle$ illuminates the atomic sample for 100 μs. The 'shadow' of the atom cloud is then imaged onto a CCD camera (Imaging Source DMK 21BF04). For intensities well below saturation, the intensity of the transmitted beam is given by Beer's Law, $I = I_0 e^{-OD}$, where OD is equal to the optical depth.

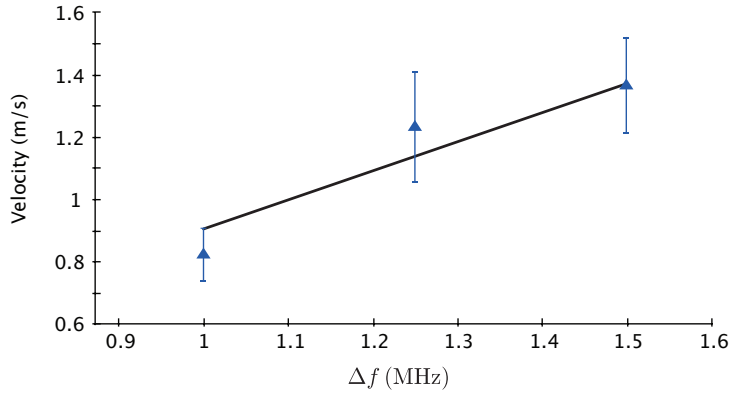


Figure 3.7 Measured fountain velocity against detuning. The best fit line gives a value of $0.9 \pm 0.2\,\mathrm{ms}^{-1}/\mathrm{MHz}$, which is reasonable in comparison to the expected $1.25\,\mathrm{ms}^{-1}/\mathrm{MHz}$.

To calculate the optical depth experimentally, three images are taken. The first of these images shows the probe beam's intensity profile with the atomic cloud present (I_{abs}), the second an image with the probe switched off (I_{dark}), and the third an image of the probe beam without the cloud present (I_{ill}), taken around 100 ms after the initial image. The dark image serves to compensate for any background and electronic noise. The optical depth is then calculated on a pixel-by-pixel basis via

$$OD = \ln\left(\frac{I_{ill} - I_{dark}}{I_{abs} - I_{dark}}\right). \tag{3.3}$$

Calculation of the total atom number within the cloud is thus a case of integrating over the entire image plane. In order to determine the central position of the atomic cloud and its radius, a two-dimensional Gaussian is fitted to the absorption image. In practice, routines calculating the atom number and cloud centre are carried out automatically using Labview software. Measuring the velocity of the cloud is thus achieved by loading and throwing the fountain a number of times, whilst taking snap-shots of the atomic cloud's position for increasing delay times after the moment the atoms are released from the fountain. The experimentally measured fountain velocity is plotted as a function of detuning in Fig. 3.7.

3.3.5 Experimental Control

The experiment is controlled via two synchronised ADLINK PCI analogue input/ output (I/O) boards. Each has 8 analogue output and 4 analogue input channels, and are run at an output update rate of 100 kHz. The inputs are used to monitor the intensity of the MOT laser beams, the temperature of the MOT coils and the pressure inside the vacuum chamber. All of the MOT, fountain and cavity control during experimental runs is done via a main Labview VI. The time dependent Rabi frequency

of the pump beam used for photon production is produced by an AOM controlled via an arbitrary-waveform-generator (AWG) (Agilent N6030A, 15 bit, 1.2 GS/s), allowing for precise control over the amplitude of the driving pulse. The AWG is triggered by a TTL signal from the I/O board after the end of the launching sequence, and the counts from the APDs are registered by an Agilent TC890 time-to-digital-converter (TDC).

3.4 High-Finesse Cavity

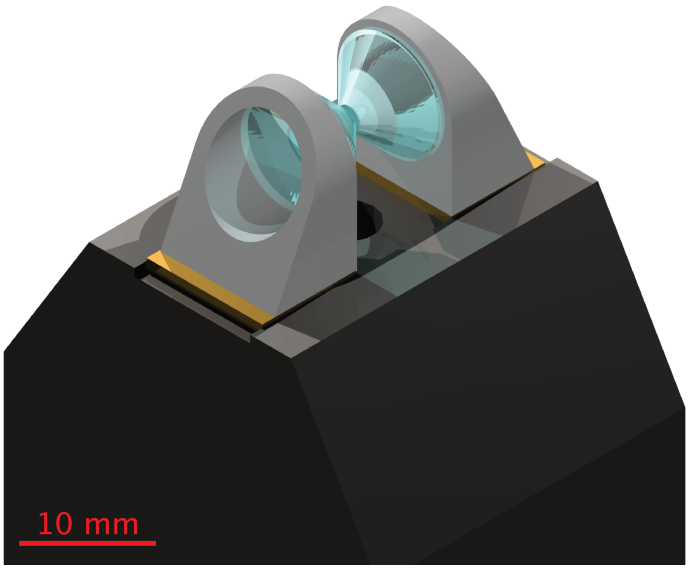


Figure 3.8 A schematic of the high-finesse optical cavity. The mirrors, ceramic mounts and shear piezos (Noliac) are glued together onto a non-magnetic stainless steel mount. The ceramic mounts were designed to be as light-weight as possible. An alignment slot aids in ensuring the motional axes of the piezos are aligned, whilst a special spacer was fabricated to allow correct alignment of the mirror mounts prior to gluing to the piezos.

The high-finesse cavity is constructed from two highly reflecting mirrors (REO, Boulder) with a length of $L \approx 75\,\mu m$, leading to a finesse of $F \approx 80,000$ and a linewidth of $\omega \approx 2\pi \times 12$ MHz.[1] It is designed to ensure excellent optical access and stability. The optical asymmetry of the cavity initially ensured that 96% of the photons emitted into the cavity leaked out of the same spatial mode. Much more

[1]The cavity had initially been constructed with mirrors of transmissivities $\{T_1, T_2\} = \{40, 1\}$ ppm, meaning that a finesse $\mathcal{F} > 100\,000$ was achieved with losses of only 2 ppm. However, during bake-out of the UHV chamber the mirror coatings were damaged, resulting in a significantly decreased finesse. This has ramifications for the efficiency of photon emission from the cavity, which is directly affected by an increase in the losses. More information about this is found in section 4.4.4.

extensive information about the cavity and its construction is found in the thesis of Peter Nisbet [85].

The science cavity is locked using the same Pound-Drever-Hall technique used to lock the lasers to the atomic resonance. In practice, the laser current is modulated via a bias-T, which allows both the laser to be locked to the atomic crossover resonance, and the cavity to be locked to the laser. The cavity exhibits excellent passive and active stability, with several seconds required in order for the cavity resonance frequency to drift by its half width at half maximum (HWHM). It is perhaps interesting to note that the relative separation of the cavity mirrors must be kept stable to within around *5 picometres* in order to keep the cavity locked to the atomic resonance.

3.4.1 Cavity Locking

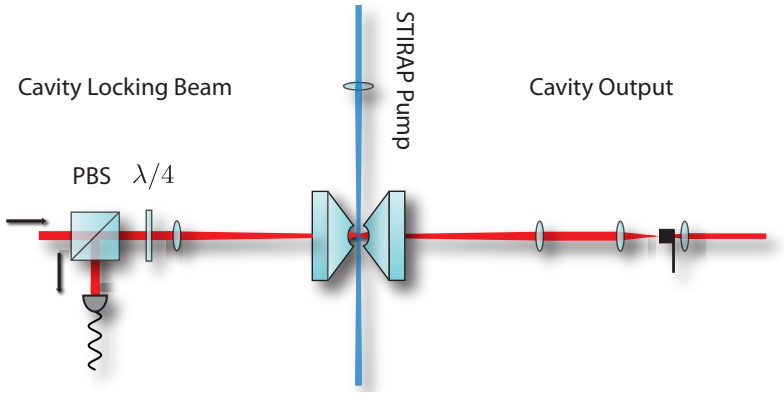


Figure 3.9 Showing the beam used for cavity locking, and the collimation and coupling of the cavity output.

The cavity locking beam is interrupted 5 ms before the atomic cloud reaches the cavity mode. A sample and hold circuit is used to keep the cavity piezo voltage stable during the time that the locking beam is off. With the piezo voltage kept stable, the passive stability of the cavity ensures that its resonant frequency drifts no more than approximately 2 MHz during the time taken for the atomic cloud to traverse the cavity mode. To ensure that absolutely no light from the locking beam impinges on the cavity during the photon production phase, the AOM is turned off and a home-built high speed shutter is used to completely block the beam. The shutter is fabricated from an electro-mechanical relay and transistor push-pull driver circuit, with switching times and jitters of a few hundred microseconds. After the atom cloud has traversed the cavity, the mechanical shutter is raised and the cavity locking beam turned back on. The sample and hold circuit then turns off and the active cavity stabilisation is re-instigated.

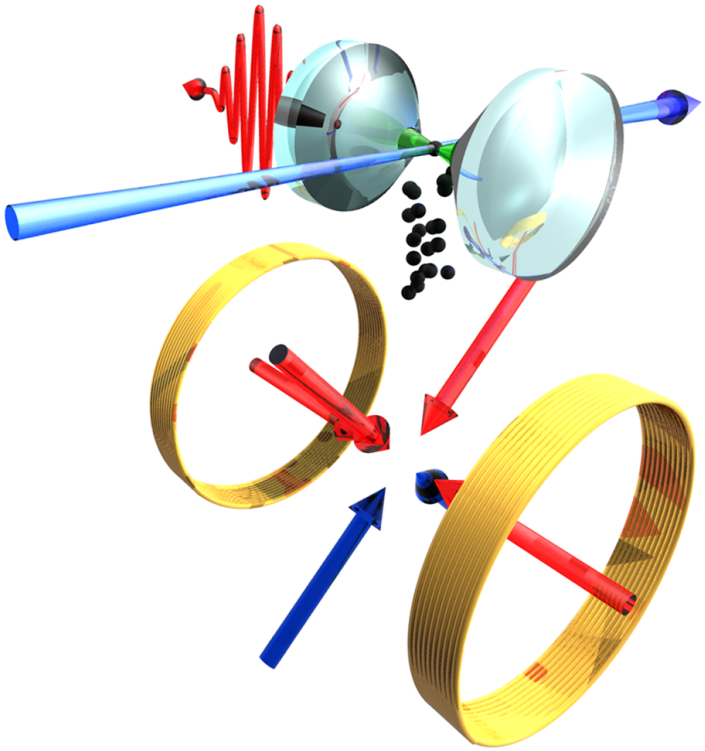


Figure 3.10 An illustration of the atomic fountain and optical cavity (not to scale). Atoms are trapped and cooled in a MOT 8 mm below the centre of the cavity. The magnetic field coils for the MOT are shown in yellow, with the beams for the moving molasses-based atomic fountain shown in red and dark blue. Atoms enter the cavity mode (green) and are driven by a classical pump beam (blue) to produce a single photon which leaks out of the cavity (red).

Chapter 4

Single Photons from a Coupled Atom-Cavity System

The preceding chapters have explained the theoretical basis and experimental components required to construct the photon pistol. This chapter examines the requirements for characterising the source, and explains how this is implemented in the laboratory. Section 4.2 describes the steps taken to optimise the atom delivery mechanism and the photon emission process. Section 4.3 deals with ensuring the singularity of photon emissions through examining second-order cross-correlations of the photon stream. The experimental attainment of this is explicated in section 4.4. Investigation into the statistics of the photons' arrival times demonstrates that one can reliably discern when one has an atom well-coupled to the cavity mode, the methodology for which is included in section 4.4.2.

Once the single emitter characteristics of the source have been established, it is vitally important to investigate the indistinguishability of the photons through two-photon interference experiments. The theory behind this is documented in section 4.5, with experimental results presented in section 4.6. Finally, section 4.7 presents results showing that control over the frequencies of the emitted photons is attainable.

4.1 Single-Photon Production

The atom-cavity system is driven by a succession of laser pulses during the time that the atom cloud traverses the cavity mode. After each application of the driving pulse, the system is reset through a secondary 'repump' pulse, reinitialising the system back in the $|e, 0\rangle$ state (assuming, that is, there is an atom in the cavity). The sequence of pulses is shown in Fig. 4.1 along with an experimental histogram of the cavity output.

Atoms begin to enter the cavity around 10 ms after having been released from the fountain. Their individual arrival times can be described by a roughly Poisson distribution, modulated by the Gaussian envelope of the atomic cloud. The finite initial radius (≈ 0.5 mm) and temperature ($70\,\mu$K) of the atom cloud mean that

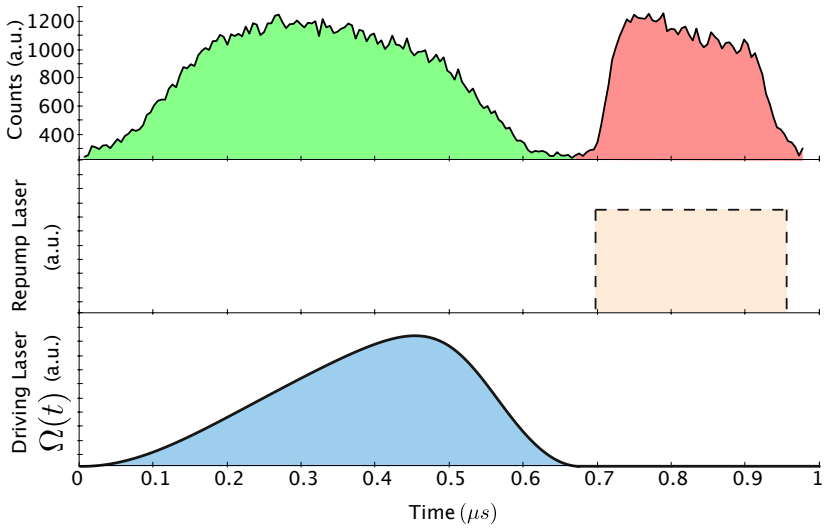


Figure 4.1 Photons are emitted from the cavity (upper plot, green) upon the application of a driving pulse (bottom plot). The atom-cavity system is then reset through a suitable repump pulse (middle plot, not to scale). Scatter from the repump pulse is visible in the upper plot and is shaded red. The photons here have a roughly Gaussian temporal distribution.

it takes around 20 ms to fully traverse the cavity. These factors limit the cavity interaction time to roughly 100 μs, but also ensure that several well coupled atoms interact with the cavity per launch.

4.2 Optimisation of the Photon Source

4.2.1 Launch Velocity

The launch velocity of the fountain has to be optimised in order to maximise the atom cloud transit time. Fig. 4.2 shows a plot of the cloud-cavity interaction times for three values of launch velocity.

4.2.2 Pump Beam

As has been mentioned previously, the pump pulse which drives the STIRAP process is generated by a double-passed AOM controlled by the arbitrary waveform generator (AWG). The maximum bandwidth of the AOM is fundamentally limited to around 6 MHz, which in turn limits the modulation bandwidth of the driving pulse and thus the photon production. The repump pulse used to reinitialise the atom-cavity system in the state $|e, 0\rangle$ is generated by the second channel on the AWG. The beams are coupled into the inputs of a 2×2, 50/50 fiber-based beam splitter for simplicity. One of the outputs of the beam splitter ($d = 7$ mm) is then focussed and aligned

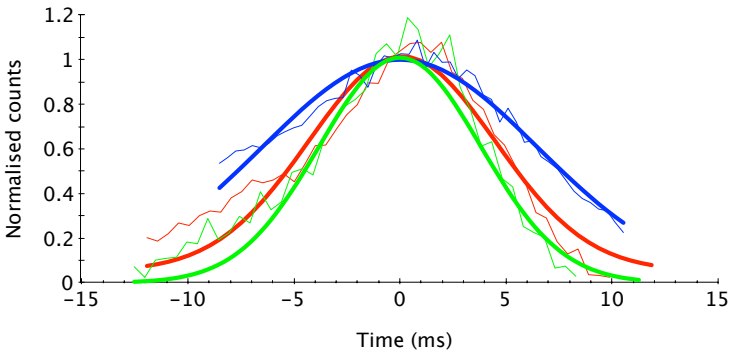


Figure 4.2 Envelope of the atom cloud passing through the cavity for three different launch velocities. Shown are the normalised SPCM counts against time (where $t = 0$ is defined as the centre of the atom cloud intersecting the cavity mode), with relative Gaussian fits. The STIRAP and repump beams are continually pulsed, and the SPCMs continually monitor the cavity output. The widths for the three cases, as determined by the fits, are $\sigma = \{5.4, 6, 6.7\}$ ms for the {green, red, blue} cases. The slowest launch velocity (blue) results in the longest interaction times.

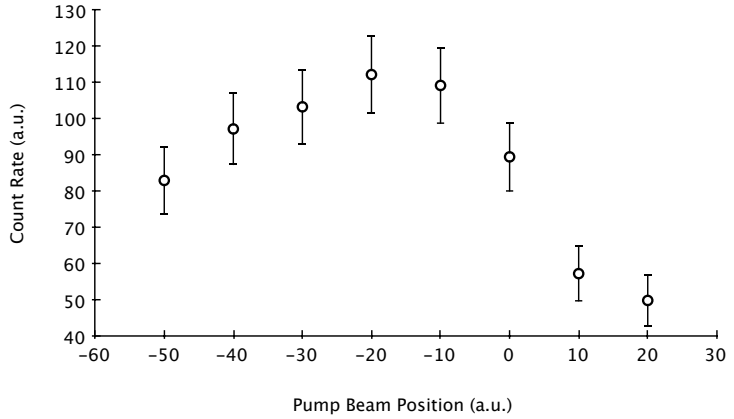


Figure 4.3 Optimisation of the position of the STIRAP pump beam. Shown are the average number of total photons detected per 100 atom cloud launches against a relative vertical position.

to intersect transversely with the cavity axis using a piezo-driven mirror mount (Newport AG-M100N), to allow for fine positioning of the pump beam relative to the cavity mode centre. A polarising beamsplitter (PBS), (extinction ratio of 1000:1), and $\lambda/2$ waveplate are used to ensure a high degree of polarisation purity, and the beam is focussed using a 300 mm achromat. This combination allows for good overlap between the focussed pump beam waist and cavity mode waist ($w_{pump} =$

19.9 μm, $w_{cav} = 18.4\,\mu$m) whilst ensuring that minimal clipping on the cavity mirror edges ensues. Fig. 4.3 shows the optimisation of the vertical position of the pump beam relative to the cavity mode.

4.2.3 Zeroing of the Magnetic Field

It was discovered, somewhat too late for easy rectification, that the bolts used to fasten the viewports to the chamber were not of the non-magnetic stainless steel variety. This had ramifications for the compensation of the magnetic field in the chamber, due to a significant inhomogeneity in the static field around the science cavity and MOT. One method for zeroing the magnetic field in the chamber involves scanning the values of the current in the X, Y and Z compensation coils and optimising a Sisyphus-cooling based optical molasses. The behaviour of the molasses is quite heavily dependent upon the value of magnetic field, and the temperature of the molasses provides feedback on the presence of a field. An alternative method

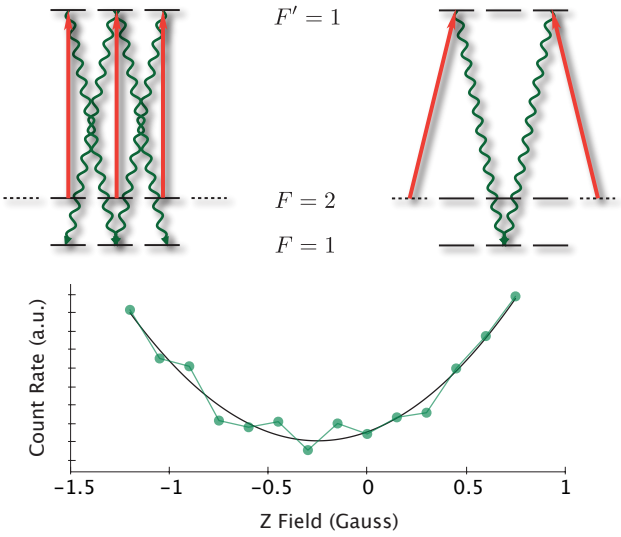


Figure 4.4 The upper left figure shows the levels we wish to drive, the right figure shows the unwanted sub-level transitions. Below is a plot showing the relative excitation rates for π and $\sigma_{+,-}$ transitions.

is based upon the production of single photons from the atom-cavity system. By selecting only certain magnetic sub-levels to pump, one is able to tune the magnetic field and polarisation of the pump beam to ensure that only certain transitions are driven. Fig. 4.4 shows the relevant magnetic sub-levels and polarisation of the pump beam involved in the process. An iterative process whereby the field and polarisation of the pump beam are adjusted allows a zero point of the field to be found. The results from the field balancing are also shown in Fig. 4.4.

4.3 Correlation Measurements

It is clear that any source which one intends to use within the framework of quantum information processing should have a number of very well defined properties, namely: the photons should be emitted from the source one by one (i.e. they exhibit *anti-bunching*); they should be delivered at the behest of the experimentalist (i.e. the source should be on-demand and deterministic); they should have well-defined spatial, temporal and polarisation modes, with well-defined frequencies and, for certain photon storage architectures, a small bandwidth. Generally speaking, the emitted photons should be *indistinguishable* from one another. The atom-cavity system and adiabatic photon production process provide us *ab initio* with many of the tools necessary to fulfil these prerequisites, as we shall see. However, the task of characterising the photons produced from the atom-cavity system, or indeed any single-photon emitter, is in itself complex. There are two main tools at the disposal of the experimentalist which enable him to carry out such a endeavour, both of which will be explicated in the following sections: the interferometer first described by Hanbury Brown and Twiss, and that realised by Hong, Ou and Mandel.

The experimentalist's first task in seeking to characterise his or her photon source should be to ensure that it is indeed functioning as a true single-photon emitter. It should be perspicuous that different states of light will necessarily have differing photon statistics, depending upon the properties of their source. These may be measured in some way by looking at the correlations between photons emanating from any particular emitter. In 1956, Hanbury Brown and Twiss demonstrated that there was a positive correlation between the signals measured by two spatially separated detectors when looking at light from a distant star [86, 87]. This was the first work demonstrating the 'bunched' nature of light emitted from thermal sources, and was followed up by a number of experiments verifying these results [88]. Anti-bunching of resonance fluorescence light was demonstrated in 1977 by Kimble et al. [4], with the first demonstration of true sub-Poissonian fluorescence shown in 1983 [89]. It was not until 1986 that the first *single-photon states* were generated in the laboratory however, a feat which was simultaneously carried out by Hong and Mandel [6] and Grangier et al. [5]. These are obviously effects which can only be satisfactorily described quantum mechanically.[1]

Given that photon number-resolving detectors are not currently a viable option,[2] a Hanbury-Brown-Twiss type interferometer is used instead [86, 87]. The second order correlation function, when dealing with the intensities of continuous fields, is given by:

$$g^{(2)}(\tau) = \frac{\langle I_1(t) I_2(t+\tau)\rangle}{\langle I_1(t)\rangle \langle I_2(t)\rangle} \tag{4.1}$$

where I_1 and I_2 are the measured intensities at detectors 1 and 2. The HBT in-

[1] It should be noted that some sub-Poissonian light is not in fact single-photon: some squeezed light may exhibit sub-Poissonian characteristics, but is not indicative of a single-photon source [90].

[2] One could potentially interrogate the photon stream using only the autocorrelation of a single detector, if said detector had an infinitely small dead time and no probability of after-pulsing.

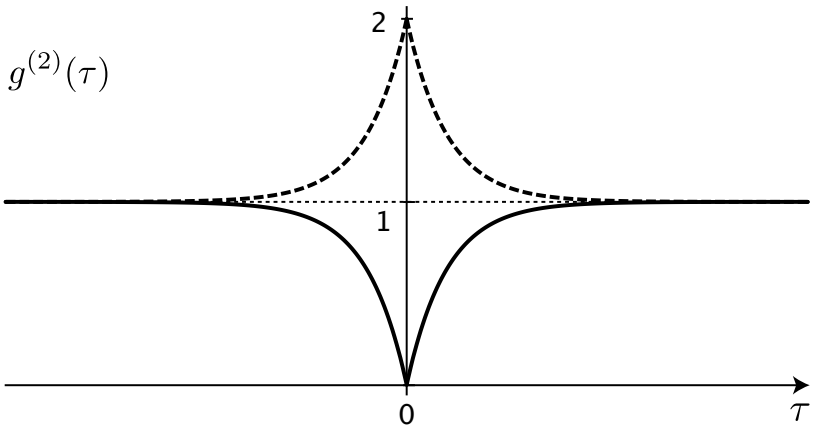


Figure 4.5 Photon statistics exhibited by correlated (dashed line), anti-correlated (solid line), or randomly correlated (dotted line) light sources.

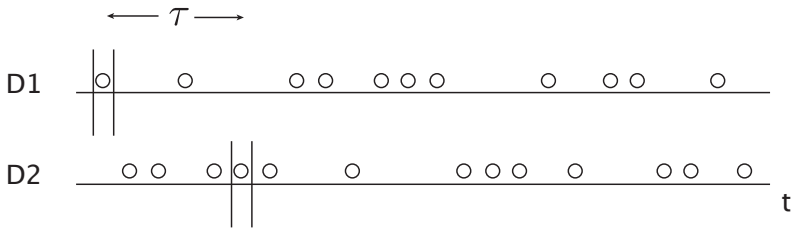


Figure 4.6 Showing the visualisation of a photon stream impinging on detectors 1 and 2 as a function of time for near perfect anti-bunching of a periodic source. The photons are distributed randomly into both arms by the 50/50 beam splitter. The width of the gate is defined by the experimentalist.

terferometer can be seen to examine the correlation in the intensity of a source's output over a given time interval, τ.

Fig. 4.5 shows the expected intensity correlation function for some notable cases. Classical light can be shown to have a $g^{(2)}(\tau = 0)$ greater than $g^{(2)}(\tau \neq 0)$: thermal light behaves in this way and can be said to exhibit bunching (or described as *supra-Poissonian*). This is shown as the dashed line in Fig. 4.5. Light whose statistics are described by the Poisson distribution (otherwise known as *coherent* light) shows a constant level of unity for all τ, and is shown by the dotted line: light from a laser exhibits exactly this behaviour. The dashed line represents light which exhibits antibunching or *sub-Poissonian* statistics, i.e. the second-order intensity correlation function falls below unity for some time intervals τ. Generally speaking, one must invoke the tenets of quantum mechanics in order to explain this behaviour.

Eq. (4.1) describes the second-order correlation function for continuous fields,

and should therefore be modified accordingly to deal with discrete events, as is the case when detecting photons with avalanche photodiodes, for example. Thus, in terms of detector clicks, we find:

$$g^{(2)}(\tau) = \frac{P_{12}(\tau)}{P_1(t)\,P_2(t+\tau)}, \tag{4.2}$$

where P_1 and P_2 are the probabilities of single clicks on detectors 1 and 2, respectively, and P_{12} is the probability of a joint detection, given the count rates of the detectors. An ideal single photon source is thus one which exhibits $g^{(2)}(0) = 0$ with $g^{(2)}(\tau) > g^{(2)}(0)$: this is to be easily interpreted as a source which never emits more than one photon at any given time. The behaviour of any real photon emitter will necessarily deviate somewhat from this ideal, but it can be seen that the value of $g^{(2)}(0)$ will provide some common yardstick with which to evaluate different sources.[3]

4.4 Photon Statistics in Experiment

The output of the cavity is coupled with an 80% efficiency into a single-mode 50/50 fiber-based beam splitter. The cavity mode is collimated using a 200 mm focal length achromatic doublet, and mode-matched using a Keplerian Telescope to a single-mode fiber coupler (Shafter and Kirchoff). A second mechanical shutter is placed at the focus of this telescope to allow the cavity locking beam to be blocked from falling onto the APDs during the MOT loading phase. Without the addition of this mechanical shutter the dark count rate of the photon counters increased significantly during the photon production time.

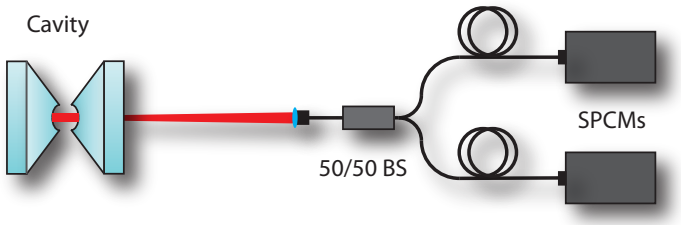


Figure 4.7 A schematic of the HBT set-up showing the 50/50 fiber-based beam splitter and SPCM modules.

Each beam splitter output is connected to a fiber-coupled single photon counting module (SPCM) (Perkin Elmer, 75% QE), as illustrated in Fig. 4.7. Clicks on detectors A and B are digitised by a time-to-digital-converter (TDC) (Agilent TC890),

[3]There is further information which may readily be gleaned from examining Hanbury Brown and Twiss data, which, in this case, is the average atom-cavity interaction time.

which has a timing resolution of 50 ps and is triggered via a digital output from the AWG. After each experimental run, the data from the TDC is transferred to a PC via a PXI interface box, and processed in MATLAB to provide an absolute timing value for each click. For the HBT, the correlations between events on detectors A and B are taken. Fig. 4.8 shows the detector cross-correlations for one experimental set of data consisting of approximately two thousand fountain launches: roughly one hundred photons are emitted from the cavity per launch. It should be noted that, for clarity, the presented data shows only raw correlations and is not normalised to produce the correct $g^{(2)}(\tau)$ correlation function. The envelope arising from the finite atom-cavity interaction time is clearly visible and is roughly Gaussian in shape, as is the pulsed nature of the source. The correlations reduce to zero between the peaks due to a removal of any detection events occurring during the repumping time.

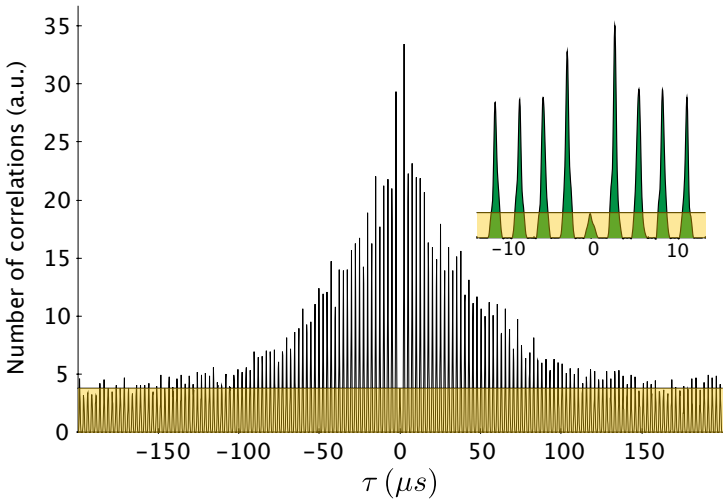


Figure 4.8 Plot showing a histogram of experimentally measured cross-correlations between two detectors for a Hanbury Brown and Twiss-type interferometer. The inset shows the correlations zoomed in around the $\tau = 0$ region. No background subtraction or normalisation of the data has been carried out. The yellow shaded region has been added to show the level of correlations arising from background.

4.4.1 Dark Count Subtraction

The avalanche photodiodes used for the detection of single photons in the NIR are technologically very mature. High detection efficiencies ($> 70\%$) can be coupled with low dark count rates (< 100 Hz). The dark count rate is often the deal breaker, and in any real device is very much inversely proportional to the price of the module. It was found the SPCMs which are used in the experiment have a much higher than specified dark count rate (measured rate $r_m > 1$ kHz, specified rate $r_s < 200$Hz).

There are obviously many potential sources of extraneous detection events, in-

cluding residual background light, scatter from the STIRAP pump beam and detector dark counts. We define detector dark count rates $d_{1,2}$ and detected photon rates $p_{1,2}$. When examining the cross-correlations it is apparent that contributions will arise from both photons (proportional to $p_1 p_2$) and from background counts (i.e. from $d_1 p_2$, $d_2 p_1$ and $d_1 d_2$). In experiments, the background rate is measured with no atoms in the cavity, i.e. without throwing any atom cloud. This then allows for a calculation of the number of 'false' correlations resulting from $d_1 p_2$, $d_2 p_1$ and $d_1 d_2$ over the total data acquisition time, given knowledge of the rates p_1 and p_2. These can then be subtracted from the histogram of the cross-correlations (applicable to both the calculation of the $g^{(2)}(\tau)$ in both the Hanbury-Brown-Twiss and the Hong-Ou-Mandel interferometers) before any normalisation is carried out.

In order to minimise the likelihood of stray light triggering the avalanche photodiodes, a 780 nm bandpass filter (Semrock, transmission $T_{780} = 97\%$) is placed in the single-photon beam path at the single-mode fiber inputs. This also serves to minimise any chance of correlations arising from 'detector flashes': these occur when a photon is detected and manifest themselves as a broadband flash of light emitted by the APD semiconductor chip. All of the fiber delay lines and NPBSs are shielded in custom-made enclosures to ensure any stray light is unable to couple evanescently into them. The shielding also has the secondary benefit of thermally insulating the fibers from the environment, whose temperature fluctuations affect both the polarisation and phase of any optical throughput.

4.4.2 Conditioning on Single Atoms

The time at which an individual atom enters the cavity mode during its ballistic trajectory is obviously not something which may be determined *a priori*. Given that the arrival of atoms into the cavity mode is essentially stochastic and that the atom-cavity interaction time is finite, the apparatus will produce photons only intermittently, its functionality being dependent upon the presence of an atom in the cavity. In reality, this poses no great ontological or practical problems for the pragmatic experimentalist. The deterministic nature of the experimentalist's source is indubitable [91], even if one does have to post-select on the presence of an atom.[4] Furthermore, in practice, the atom-cavity interaction time is most sufficient for allowing a large number of realistic operations to be performed during the transit time of a single atom. Further discussion of this phenomenon is presented in [36], with the addition of proposed repeat-until-success techniques which could well be of great utility for similar periodic sources.

Given these considerations then, we see that the statistics of the emitted photons cannot be said to exhibit sub-Poissonian statistics if one considers the entire duration of the atom-cloud transit. It is necessary to ensure that the flux of atoms entering the cavity is low enough to ensure that the probability of having > 1 atom in

[4] The pedant would perhaps point out that intermittency is inherent in the nature of any such single-photon source, whose proper functionality is dependent upon the necessary (but sadly not sufficient) condition of having a PhD student present in the laboratory.

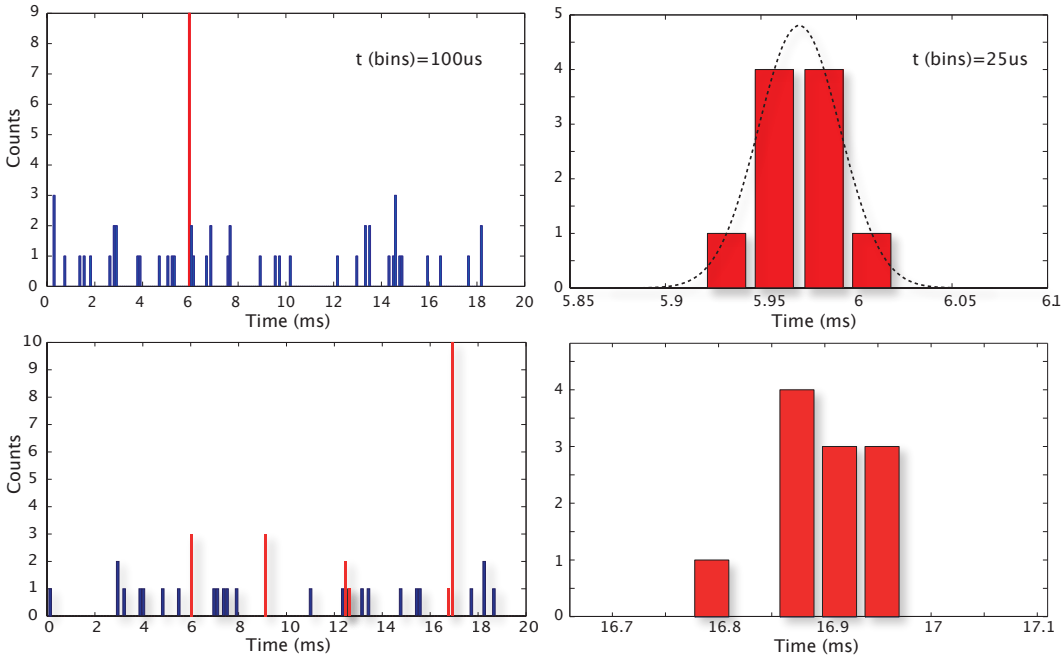


Figure 4.9 Upper figure: The left plot shows a histogram of the detected photons over the whole atom cloud transit time (20 ms) with a time binning of 100 μs. A well coupled atom traversing the cavity is clearly visible at $t = 6$ ms, indicated by the clear spike in detection events. The right plot shows a histogram of the count events, zoomed in around $t = 6$ ms, with a fitted Gaussian overlaid. Lower figure: A Monte Carlo simulation of detector clicks for an atom cloud traversing the cavity. Parameters close to the experimentally measured values are used (atom number, temperature, launch velocity) to calculate the trajectories of 10^5 atoms starting with an initial Maxwell-Boltzmann velocity distribution. The emission probability for an atom interacting with the cavity-mode is calculated from the value of g_{eff} it experiences, and an uncorrelated background dark count added. Photon detection events are shown in red and dark count events in blue. The counts seems to agree qualitatively well with the experimental data.

the cavity is acceptably small, whilst maintaining a reasonable single atom arrival rate. Ergo, for the majority of the time there is no atom coupled to the cavity mode. One can, however, determine when atoms become well coupled to the cavity, allowing the subsequent recovery of the sub-Poissonian nature of the source [75, 91–93]. Examining the hits on both detectors over the duration of a single experimental run often clearly signals when a single atom becomes well coupled to the cavity mode. This is flagged by a clear spike in the count rate as the atom passes through the mode, as illustrated in Fig. 4.9. The data shown is from a single experimental run, and a single atom traversing the cavity mode is clearly discriminated at $t = 6\,\text{ms}$. By zooming into the region around 6 ms and re-binning the detection events, one obtains the histogram shown on the right in Fig. 4.9. It is interesting to note that it is possible to retrieve the transverse Gaussian envelope of the cavity mode by looking at the discrete count events around this time. Qualitatively, this can be simply explained by the fact that g_{eff} is proportional to the electric field at a given point in the cavity mode ($g(r) = \sqrt{\frac{\mu^2\omega_c}{2\epsilon_0 V\hbar}} f(r)$, where $f(r)$ is the cavity mode distribution), and that the production efficiency is roughly proportional to g_{eff} (see section 4.4.4). A Monte-Carlo simulation of photon emission from the cavity is also shown, calculated for 10^5 individual atoms. The measured experimental parameters are used for the calculation.

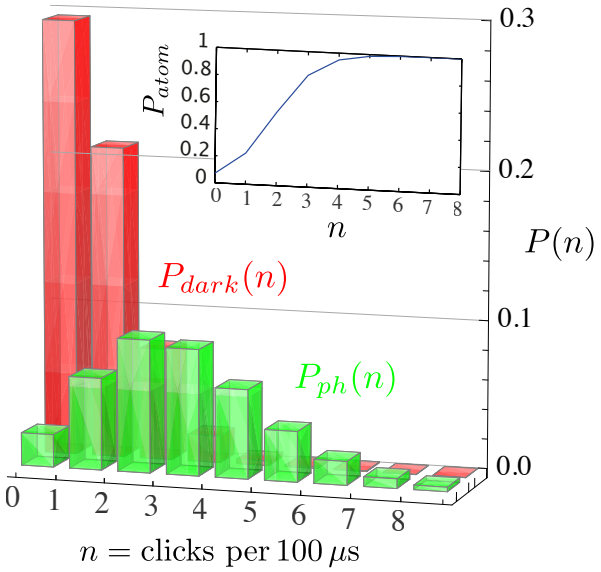


Figure 4.10 Poissonian fits to experimental data showing the relative likelihood of detecting n events in 100 μs with (green bars) and without (red bars) an atom in the cavity. The inset shows the probability that an atom is present in the cavity, given a number of detection events, n.

It is perhaps pertinent to note the effectiveness of post-selecting for well coupled

atoms. One simple checksum to verify the veracity of selecting for single atoms is to examine the relative probabilities of conditioning on dark counts and conditioning on genuine photon emissions. The Poisson distribution, $P_v(n)$, determines the probability of seeing n events within a given time interval in which there is an expected number of events v. Thus, for a dark count rate given by $r_{dark} = 2\,\mathrm{ms}^{-1}$ and a time bin length described by t, the Poisson distribution is given by

$$P_{dark}(n) = \frac{(t\, r_{dark})^n\, e^{-t\, r_{dark}}}{n!}. \tag{4.3}$$

It is also possible to describe the number of photons emitted per atom with the Poisson distribution, given that not all atoms will pass through the centre of the cavity mode and the emission process does not have unit efficiency. Obviously, in the limit of the spurious count rate tending toward zero, $r_{dark} \to 0$, all detection events will be due to single photon emissions. However, in any realistic system, given a number of detection events we can roughly gauge the probability of having a well coupled atom in the cavity:

$$P_{atom} \approx \frac{P_{ph}(n)}{P_{ph}(n) + P_{dark}(n)}. \tag{4.4}$$

If we know the dark count rate for a given set of data, it is possible to fit the remaining data to determine the distribution of detected photons per atom. Fig. 4.10 shows fits to an experimental set of data for time bins of $100\,\mu$s. The inset shows the relative probability of having an atom in the cavity, given the number of counts, n, found in a single time bin. For $n = 5$ detection events, for example, we can be 97.1% certain that there is an atom in the cavity mode.

4.4.3 Discriminated Data

Figs. 4.11 and 4.12 show comparative cross correlations for single sets of data with (right) and without (left) conditioning on the presence of an atom in the cavity. The unconditioned data exhibits a central peak height roughly equal to one, which is expected for correlations arising from noise and multiple atom contributions over a long period of time. The correlations in the right figure are calculated only with respect to the times that an atom is present, using the method outlined above. The height of the central peak then falls significantly below one (essentially disappearing for the data with a low atom flux), demonstrating the conditioned sub-Poissonian nature of the source.

It is also possible to apply a rolling filter to the data, that is, to apply the conditioning algorithm and 'remove' the times in between well-coupled atoms. Correlations can then be made on the data over time periods much longer than the atom-cavity interaction times. Fig. 4.13 illustrates this. Each photon pulse has here been taken as a single bin. The average value away from $\tau = 0$ is then ≈ 1, and again the central peak is missing. The height of the central peak is $g^{(2)}(0) = 0.049 \pm 0.028$.

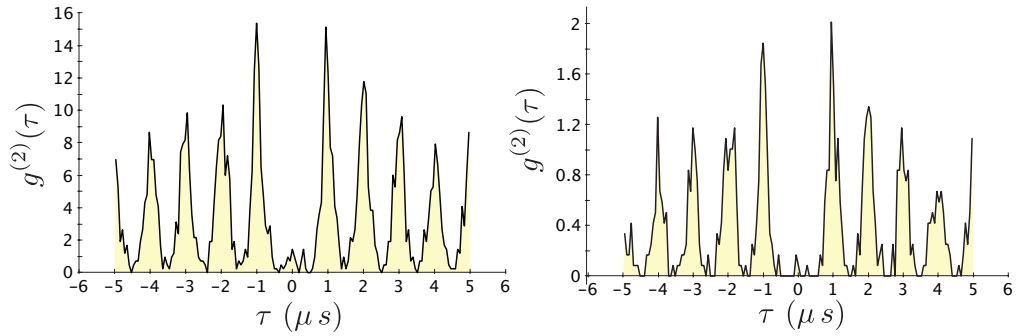


Figure 4.11 Retrieval of the sub-Poissonian nature of the single photon source. The left plot shows the normalised $g^{(2)}(\tau)$ cross-correlation for a set of data with no conditioning on the presence of an atom. The height of the central peak has a maximum of $g^{(2)}(0) \approx 1$, which is a result of background correlations and the Poissonian arrival of atoms. The right plot shows the normalised correlation function for the same data set, having conditioned on an atom being well coupled to the cavity mode. The cross-correlation at $\tau = 0$ is now significantly reduced, demonstrating the sub-Poissonian nature of the conditioned photon source.

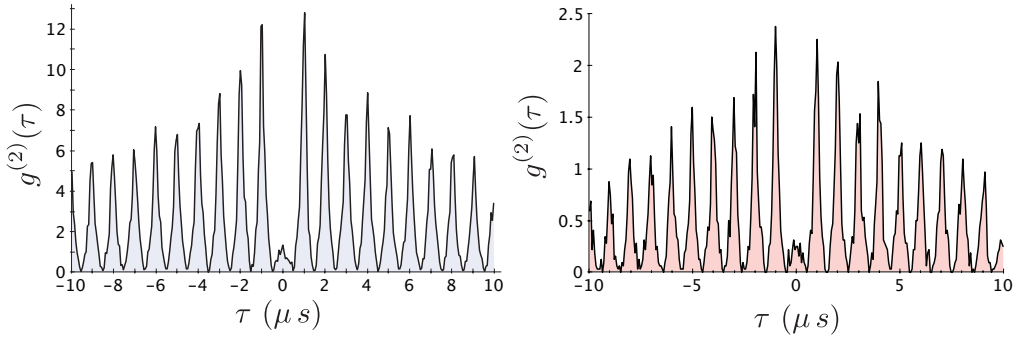


Figure 4.12 A $g^{(2)}(\tau)$ correlation function showing what happens when the atom flux is too high. Both plots as previously. The left shows the intensity correlation function without any conditioning on an atom in the cavity. The right plot shows the obtained $g^{(2)}(\tau)$ after having conditioned on the times that an atom is well coupled to the cavity mode. It can be seen that there are still fairly significant non-zero contributions arising around the central peak.

4.4.4 Photon Production Efficiency

In order to measure the maximum generation efficiency, we can utilise the same technique of conditioning on the presence of an atom in the cavity. The stream of detector counts for each experimental run is taken and a histogram of counts created.

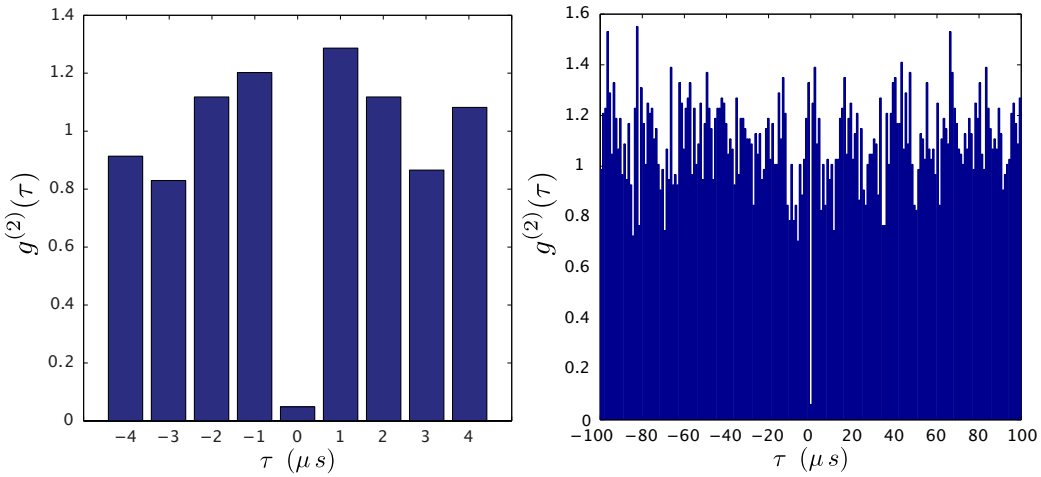


Figure 4.13 A $g^{(2)}(\tau)$ correlation function calculated with a rolling filter. Left and right plots show the same data but at different magnifications. It is quite apparent that the central peak at $\tau = 0$ is missing. The height of this central peak is found to be $g^{(2)}(0) = 0.049 \pm 0.028$ and is fully explained by correlations arising from dark counts.

For bins containing a number of counts greater than a specified value, n_{dis}, Eq. (4.3) tells us the probability of these counts arising from a single atom. Because of the long interaction time it is then possible to, as before, re-bin the data and fit a Gaussian envelope to the detector clicks. The central peak of this fitted Gaussian is taken as the point at which the atom was interacting with the centre of the cavity mode. The probability of detecting photons in the previous and subsequent pulses can then be easily calculated when data from a large ensemble of atom transits is taken. If one incorporates detector efficiencies (75%), fiber coupling efficiencies (80%), beam splitter transmissions (95%) and absorption losses in the cavity (50%), the maximum photon production efficiency inside the cavity is measured to be $P_{max} \approx 85\%$.

4.5 Indistinguishability

A truly quantum phenomenon, two photon interference was demonstrated experimentally in 1987 by Hong, Ou and Mandel with single photons from a parametric downconversion source [94]. It is, in many ways, the embodiment of the manifestation of quantum mechanics at its most fundamental level. Since that time, indistinguishability (or quantum interference) has been demonstrated with single photons from a multitude of systems including quantum dots [95], neutral atom-cavity systems [96], ion traps [97], separate trapped atoms [98], NV centres [99] and molecules [100]. Interference between disparate sources, namely a quantum dot and down-conversion source, has also been recently demonstrated [101]. It is worth noting that particular effort has to be exerted in order to interfere independent sources

of a similar type, e.g. quantum dots and NV centres, given that there is often a spread in centre wavelengths of the devices, and significant spectral filtering often must be implemented. This phenomenon also promises to be the basis for the implementation of controllable gates realised within the framework of LOQC, for example [70, 102, 103]. Given that indistinguishability is essential to the realisation of many of these proposals and computation protocols, it would seem pertinent to investigate the temporal and spectral properties of any particular single photon source. The long temporal length of the photons produced by adiabatic Raman transitions allows for the use of time-resolved two photon interference: this can enable a near complete characterisation of the photon source, or, at the very least, place upper bounds on the quantitative description of many of the photons' desirable properties.

4.5.1 Two-Photon Interference

Let us initially consider two-photon interference without reference to any time-dependence. We consider a beam splitter with two incoming modes A and B, and outgoing modes C and D, as illustrated in Fig. 4.14. If we consider a 50/50 beam splitter, we see that it will act on the input fields with the following unitary transformations:

$$\begin{aligned} \hat{a}_A^\dagger &= (\hat{a}_C^\dagger + \hat{a}_D^\dagger)/\sqrt{2} \\ \hat{a}_B^\dagger &= (\hat{a}_C^\dagger - \hat{a}_D^\dagger)/\sqrt{2} \\ \hat{a}_C^\dagger &= (\hat{a}_A^\dagger + \hat{a}_B^\dagger)/\sqrt{2} \\ \hat{a}_D^\dagger &= (\hat{a}_A^\dagger - \hat{a}_B^\dagger)/\sqrt{2}, \end{aligned} \tag{4.5}$$

or alternatively,

$$\begin{pmatrix} \hat{a}_A^\dagger \\ \hat{a}_B^\dagger \end{pmatrix} = \frac{1}{\sqrt{2}} \begin{pmatrix} 1 & 1 \\ 1 & -1 \end{pmatrix} \begin{pmatrix} \hat{a}_C^\dagger \\ \hat{a}_D^\dagger \end{pmatrix}. \tag{4.6}$$

Two photons impinging simultaneously on ports A and B may be described by application of the creation operators to the vacuum state

$$|1,1\rangle_{A,B} = \hat{a}_A^\dagger \hat{a}_B^\dagger |0,0\rangle_{A,B} \tag{4.7}$$

which, after the beam splitter transformation gives

$$\begin{aligned} \frac{1}{2}\left(\hat{a}_C^\dagger + \hat{a}_D^\dagger\right)\left(\hat{a}_C^\dagger - \hat{a}_D^\dagger\right)|0,0\rangle_{C,D} &= \frac{1}{2}\left(\hat{a}_C^{\dagger 2} - \hat{a}_D^{\dagger 2} - \hat{a}_C^\dagger \hat{a}_D^\dagger + \hat{a}_D^\dagger \hat{a}_C^\dagger\right)|0,0\rangle_{C,D} \\ &= \frac{1}{2}\left(\hat{a}_C^{\dagger 2} - \hat{a}_D^{\dagger 2}\right)|0,0\rangle_{C,D} \\ &= \frac{|2,0\rangle_{C,D} - |0,2\rangle_{C,D}}{\sqrt{2}}. \end{aligned} \tag{4.8}$$

The cases on the right of the first line of Eq. (4.8), $\hat{a}_C^\dagger \hat{a}_D^\dagger$ and $\hat{a}_D^\dagger \hat{a}_C^\dagger$, are indistinguishable (i.e. $\hat{a}_C^\dagger$ and $\hat{a}_D^\dagger$ commute), but interfere destructively because of their opposite signs. This then leads to the two remaining possibilities, with equal probability amplitudes, of the photons both exiting through port C or port D.

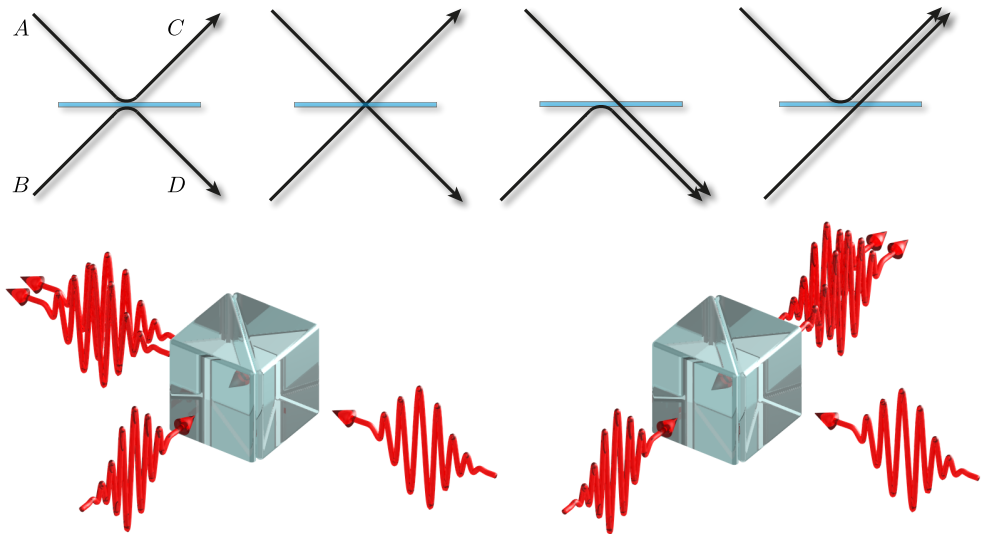


Figure 4.14 Upper: plot demonstrating the addition of probability amplitudes for two photon interference. The first two probability amplitudes interfere destructively for identical photons, which will coalesce and leave one of the output ports together (shown in lower schematic).

4.5.2 Time-Resolved Two-Photon Interference

A full handling of the effect of two photon interference is given in [96, 104, 105] where the equivalence of different possible formulations of the effect are shown. In the following explication, we engage only in a brief and somewhat simplified description of the phenomena [106], and consider the case where two free-running photons overlap on a beamsplitter in the space-time domain. We are interested in the Hong-Ou-Mandel interferometer operating specifically in the time-resolved regime, viz, where the temporal resolution of the detectors is significantly shorter than the length of the photons.[5]

We do not restrict the photons to any particular frequency mode, and thus are able to define creation and annihilation operators specific to an arbitrary spatio-temporal mode: $\hat{a}_k^\dagger, \hat{a}_k$. We can then define a mode function of the field, ζ, which is the product of a real amplitude and a complex phase:

$$\zeta_k(t) = \epsilon_k(t)\, e^{-i\phi_k(t)}. \tag{4.9}$$

[5]In the following experiment, the detectors have a resolution of approximately 100 ps, and the photons a width of around 200 ns. This regime is to be compared to that investigated by, for example, PDC sources, whose ultrafast photons are often orders of magnitude *shorter* than the best SPCM detectors' resolutions. In the latter regime, the extra information gleaned in the time-resolved case through examining those correlations found around $\delta\tau = 0$ is simply averaged over. The coincidences are therefore plotted as a function of some experimentally introduced delay between the arrival times of the two photons at the beam splitter.

The envelope of the mode function we assume to be normalised, that is, $\int dt|\epsilon_k(t)|^2 = 1$. We now consider the detection events that should be seen on detectors placed at the output ports C and D, by taking into account the effect of the beamsplitter on the incoming modes $\zeta_1(t)$ and $\zeta_2(t)$. The probability of detecting an initial photon at port C at a time t_0, for example, is simply defined by the individual mode functions:

$$P_C(t) = \frac{1}{2}\left(|\epsilon_1(t_0)|^2 + |\epsilon_2(t_0)|^2\right). \tag{4.10}$$

Assuming that we detect a photon with detector C at time t_0, we now ask for the probability of detecting a photon with detector D at time $t_0 + \tau$, given the previous detector click. Now, because this initial photon could have come from either input mode and the detection revealed no which-path information, the system is projected into a reduced superposition state given by:

$$|\Psi_\pm\rangle = \hat{a}^\dagger_{C,D}|\Psi_{in}\rangle \propto \zeta_2(t_0)|1,0\rangle_{A,B} \pm \zeta_1(t_0)|0,1\rangle_{A,B}, \tag{4.11}$$

where the sign is dependent upon which detector fired at t_0, and the initial state, $|\Psi_{in}\rangle = |1,1\rangle_{A,B}$, consists of two photons impinging on ports A and B. This superposition state now evolves in time according to $\zeta_1(t)$ and $\zeta_2(t)$. A detection at time $(t_0 + \tau)$ can therefore happen at port C or D, with a probability dependent upon the relative mode functions.[6] Obviously, these modes may evolve differently with time, and the probability of detection of the secondary photon at detector D, conditioned on seeing the first photon at detector C, is then given by:

$$P_{C,D}(t_0,\tau) = \frac{1}{4}|\zeta_1(t_0+\tau)\zeta_2(t_0) - \zeta_2(t_0+\tau)\zeta_1(t_0)|^2. \tag{4.12}$$

Here we have a remarkably simple expression which describes fully the joint probability of detection for two photons occupying arbitrary field modes when brought together on a beamsplitter. If the two mode functions are identical, then we note trivially that the second detection will always occur at the same port as the first. However, with some phase relationship which evolves with time, or frequency difference, we see that some interesting behaviour may occur. We also note that correlations between the two detectors never occur at zero detection time difference, $\tau = 0$, as the relative phase is defined only upon the first detection.

If the two photons have perpendicular polarisation and do not interfere, then each will exit randomly through either port. The detected coincidences will then have some temporal envelope which is dictated simply by the convolution of the two photon shapes. Conversely, if both photons occupy identical modes and have equal polarisations, then both modes will evolve identically in time: detection of the second photon will then occur in the same output port as the first, and no coincidences will be seen.

[6] One can now interpret this reduced quantum state as a single photon in a path state superposition impinging onto the beam splitter, and thus the subsequent interference can in fact be treated classically.

In Chapter 5 we extend this description of two photon interference to dealing with the preparation of qudits of arbitrary phase: we demonstrate how to actually tailor the properties of the emitted photons, that is, to have almost complete control over both the envelope and the phase, $\epsilon_k(t)\, e^{-i\phi_k(t)}$, and show how these might be useful for quantum networking. In these following sections, we will examine in slightly more detail the phenomenon of time-resolved two-photon interference, and see how we utilise it to characterise the spectral and temporal properties of the photons emitted from the atom cavity system.

4.5.3 Well-Defined Frequency Offset

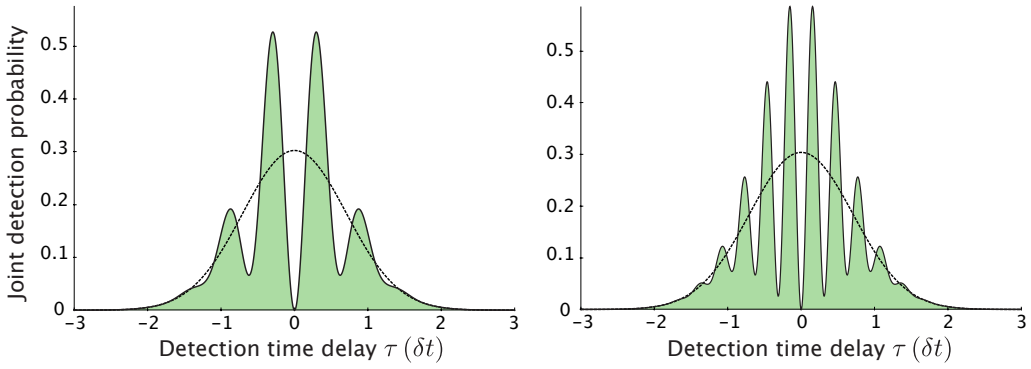


Figure 4.15 The average joint probability distribution, $P_{C,D}(\tau)$, for two Gaussian-shaped photons arriving at the beamsplitter with a frequency difference of Δ. The left and right plots have values of $\Delta = (10, 20)\,\delta$t, respectively. The oscillatory pattern illustrates the quantum beat of the two photonic modes.

Any frequency difference (or constant change in relative phase) between the two modes will manifest itself as an oscillation in the joint detection probability. If we consider a frequency difference between the two modes given by $\Delta = \omega_1 - \omega_2$, we can see that the temporal interference pattern will consist of the temporal envelope indicative of non-interfering photons, modulated by an oscillation at frequency Δ. Considering Gaussian photons of width δ t, and following on from Eq. (4.12), we find

$$\begin{aligned} P_{C,D}(\tau) &= P_{perp}\left[1 - \cos(\Delta\tau)\right] \\ &= \frac{1}{2\sqrt{\pi}} \exp\left(\frac{-\tau^2}{\delta t^2}\right) \left[1 - \cos(\Delta\tau)\right], \end{aligned} \tag{4.13}$$

which arises from the simple result that the convolution of two Gaussians is itself Gaussian. An example of this effect is shown in Fig. 4.15 for two different values of Δ.

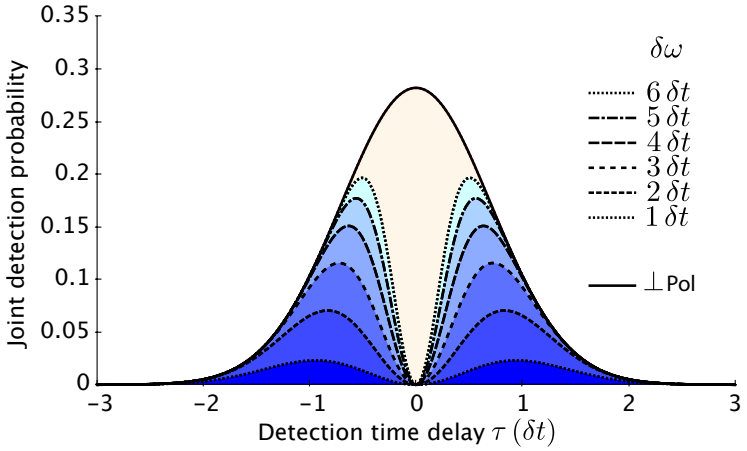


Figure 4.16 Showing the average joint detection probability, $P_{C,D}(\tau)$, for photons with differing frequency jitters, where $\delta\omega = \{1 \rightarrow 6\}\,\delta t$.

4.5.4 Jitter

Simply due to the nature of the atom-cavity system (and indeed almost any such source), the stream of photons emitted from the cavity will, on an individual basis, vary somewhat from the ideal. Variations in the driving pulse, the value of g_{eff} experienced by the atom, laser noise and perturbations to the atomic levels may all be contributing factors to such an effect. Any distinguishability between photons will result in imperfect two-photon interference - something easily probed with the use of the Hong-Ou-Mandel interferometer.

Following directly on from Section 4.5.2, we now turn to the description of the interference of such photons. Any jitter in the photons' parameters, as described above, will manifest itself in some dephasing visible in the two-photon correlation. Again, taking inspiration from [105], where a full description of the effect is given, we consider two streams of photons impinging onto a beam splitter. We assume that each photon stream has some variation in its central frequency, such that any particular photon pair interfering on the beamsplitter will have some discrepancy in frequency given by $\Delta = \omega_1 - \omega_2$. If the jitters in the photons' frequencies (denoted here by $\delta\omega$) are described by a Gaussian distribution, any individual oscillatory interference patterns arising from the two-photon interference will be averaged over during the course of many detection events.

The resultant coincidence pattern will thus exhibit a zero at detection time difference $\tau = 0$, as always, but will then show some dephasing indicative of the Gaussian distribution of the frequencies. The width of this central dip (or the *coherence time*) in the resultant two-photon interference pattern is dependant upon the magnitude of the jitters. The obtained expression describing interfering photon

streams with Gaussian envelopes and jitters of width $\delta\omega$ is thus given by

$$P_{C,D}(\tau) = \frac{T}{2\sqrt{\pi}\delta t}\left[1 - \cos^2(\psi)\exp\left(-\frac{\tau^2}{4/\delta\omega^2}\right)\right]\exp\left(-\frac{\tau^2}{\delta t^2}\right). \tag{4.14}$$

Fig. 4.16 shows the nature of this effect for photons with Gaussian envelopes and Gaussian frequency jitters whose widths range from $1 \rightarrow 6\,\delta t$. The factor ψ has been added in to the above equation in order to account for any discrepancy between the polarisation or spatial modes of freedom of the two photon streams, and is ideally zero for perfectly matched modes.

It should be noted that there is a second possible explanation for the apparent dephasing shown above. A jitter in the emission times of the photons, leading to a jitter in their arrival times at the beam splitter, would also account for the witnessed correlations. This is quite simply explained by the fact that two photonic modes do not overlap perfectly, as required for ideal coalescence, and thus correlations might well be witnessed at times away from $\tau = 0$. The interpretation of any experimental result leading to such a correlation pattern is limited by the fact that there are two possible mechanisms capable of producing the same data. It is however possible to ascribe values to the upper bounds of said phenomena, i.e. the value of frequency jitter which would explain the attained data in the absence of emission time jitter, and vice versa. It should be noted that in reality, both effects will contribute somewhat to the detected coherence time.[7]

4.6 Demonstrating Indistinguishability with Real Photons

In practice, the experimental arrangement to implement the Hong-Ou-Mandel interferometer is shown in Fig. 4.17. The output of the cavity is collimated and sent onto a PBS. Photons are directed at random down either a $1\,\mu$s (200 m, Nufern 780-HP) delay line, or directly to a 50/50 fiber-based polarisation-maintaining beam splitter. The delay line has a fiber polarisation controller incorporated, as small temperature drifts in the laboratory contribute to a rotation of the polarisation of the photons at the fiber output. Although this polarisation is checked regularly, a second PBS is placed after the polarisation controller to act as a filter and ensure that the interfering photons are as carefully matched as possible. The delay line is then coupled in to the secondary input of the fiber-based beam splitter, and in this way subsequently emitted photons from the cavity are spatially and temporally overlapped. The spatial overlap of the two modes is considered to be $> 99\%$ whilst the temporal overlap is carefully calibrated. Finally, the outputs of the fiber-based beam splitter are connected to fiber-coupled SPCMs (as before).

[7] There is perhaps reason to believe that it is frequency jitter that gives rise to the witnessed coherence times, in certain instances. The coherence times, for example, may be on a par with the transform limited bandwidths of the photons alone, implying that the limiting factor is indeed the spread in frequencies of the photons and not their temporal jitter.

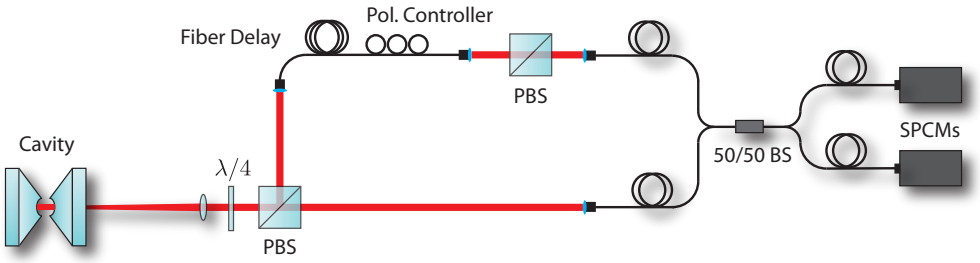


Figure 4.17 A schematic of the HOM set-up. Photons are emitted from the cavity and pass through a $\lambda/4$ plate and polarising beam splitter (PBS). A fiber-based polarisation controller is used to ensure maximum transmission through the second PBS which acts only as polarisation filter. Finally, the delayed arm and cavity output are brought together on both ports of the 50/50 fiber-based beam splitter (Newport F-PMC-780-50).

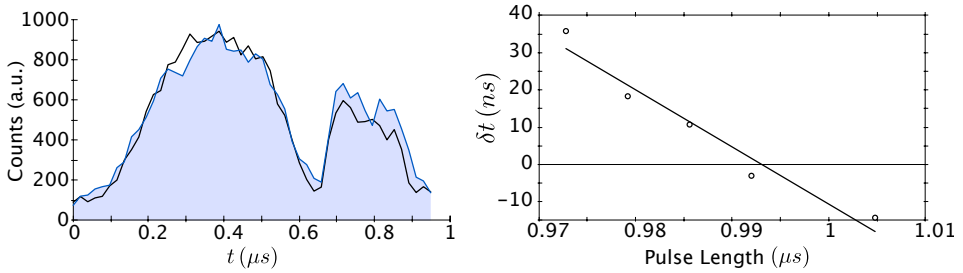


Figure 4.18 Calibration of the repetition rate. Left: Histograms of the arrival times for photons going either straight to the NPBS beam splitter with the 200 m fiber delay line blocked (blue), or vice versa (black). Both the single photon emission and repump contributions are visible in each plot. Right: plot of the measured difference in arrival time versus pulse length.

In order to overlap subsequently emitted photons in time, the time delay of the fiber has to be carefully calibrated and the repetition rate of the experiment carefully matched to it (given that no control over the fiber length is possible). Thus, photons emitted from the cavity are sent down either the delay arm or directly to the beam splitter, with the opposite arm blocked in turn. The arrival times for each of the arms is noted, and the repetition rate of the STIRAP driving pulses optimised accordingly. Fig. 4.18 shows a histogram of the counts for single photons which have travelled either down the delay line or straight to the beam splitter, after optimisation. Obviously, it is important to ensure that this time is as closely matched as possible, given that any incongruity in the arrival times of the photons will have a detrimental effect on the two photon interference which is relied upon for the Hong-Ou-Mandel interferometer [105].

The correlations between counts seen on the detectors during the same pump

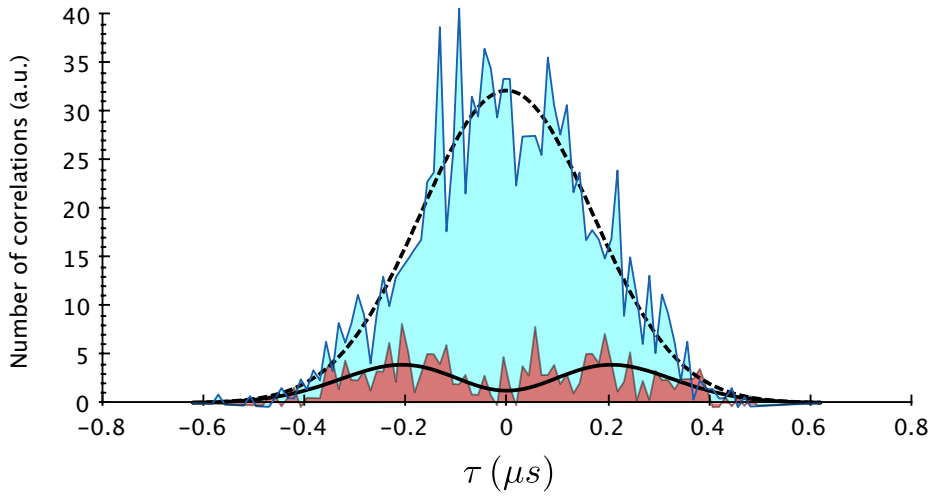


Figure 4.19 Results from a Hong-Ou-Mandel type interferometer for photons of Gaussian shape interfering on a beam splitter. The non-interfering case (perpendicular polarisation) is shown in blue, and the interfering case (parallel polarisation) is shown in red. The width of the corresponding correlation function for the perpendicular case is 250 ns (half width at 1/e), which arises from the convolution of two photons of 180 ns width. The coherence time is determined to be $T_c = 410 \pm 30$ ns and the visibility $V = 0.87 \pm 0.05$.

pulse are then measured, and may be plotted in a histogram to demonstrate the joint detection probability. Fig. 4.19 shows the experimentally measured number of correlation events for the perpendicular (blue) and parallel (red) polarisation cases. Each data set has a total of 2×10^5 detected photons, and correlations arising from dark counts have been subtracted from both. In order to obtain a fit for the coherence time, the perpendicular case is fitted first to determine values for both the amplitude and the width of the correlation function (dashed line). With these, the only free parameter available for fitting in the parallel polarisation case (solid line) is the coherence time, T_c. This is found to be $T_c = 410 \pm 30$ ns. A value of $\cos^2(\psi) = 0.96$ has been used to describe the mismatch between the modes. Normalisation of the data is achieved by scaling relative to the number of correlations in the ± 1 peaks of the (un-normalised) $g^{(2)}$ cross-correlation function (shown in Fig. 4.20). This method should accurately reflect the number of correlations obtained over an entire experimental run, and should be insensitive to variations in background count rate, etc. [93].

Fig. 4.20 shows a set of data where the correlations have been plotted against a larger detection time delay, $\tau = \pm 100\,\mu$s, in a manner analogous to the previous Hanbury Brown and Twiss data. It is clear that the two photon interference plot shown in Fig. 4.19 is, in general, a special sub-set of the plot shown in Fig. 4.20.

We define the visibility V_{2ph} as one minus the ratio of the areas under the cor-

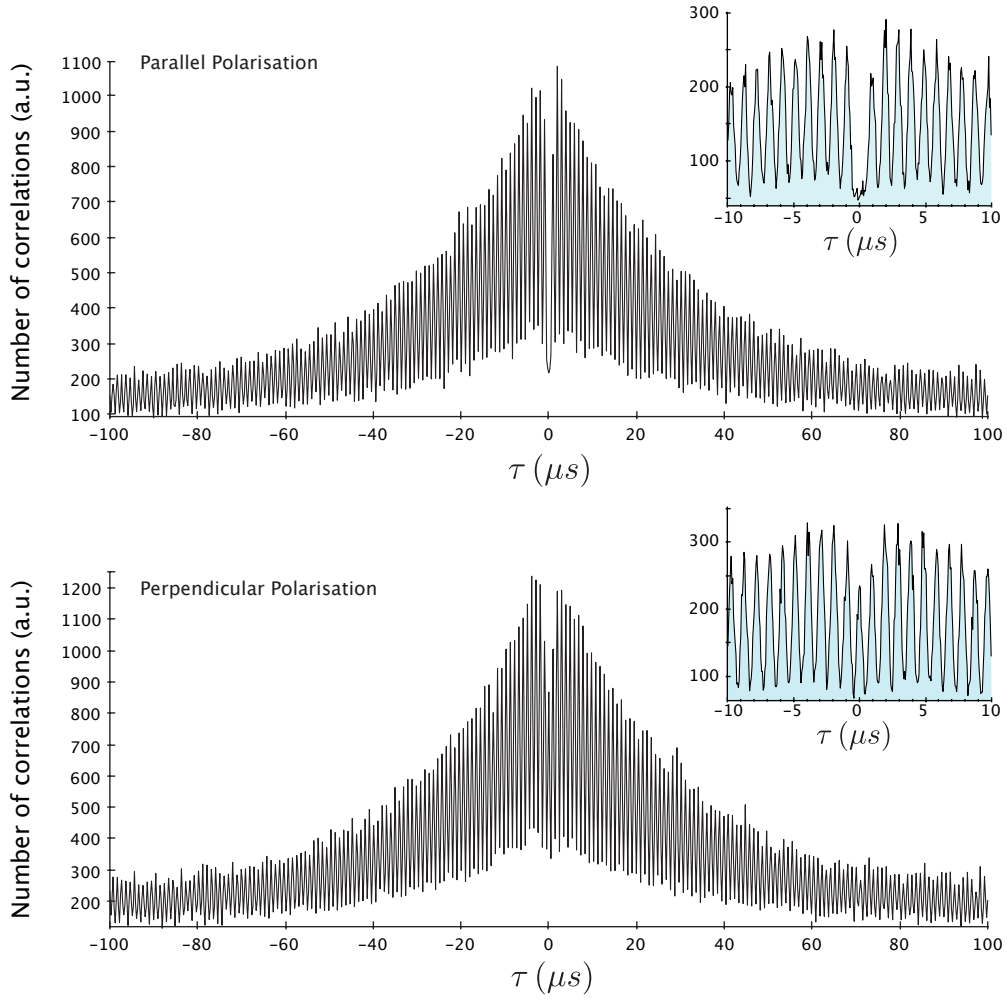


Figure 4.20 Experimentally measured cross-correlations for perpendicular and parallel polarised photons. Both insets show the same data, zoomed in around the $\tau = 0$ region. Neither data set is normalised or has had any background subtracted.The central peak (or lack thereof) is the salient feature of the corresponding plots, indicating that the photons either coalesce on the beam splitter or leave either port randomly, depending on their polarisation state. Note the significant background level present at $g^{(2)}(0)$ which is partly explained by correlations from dark counts, but is mostly a result of contributions from background atoms (the atomic flux through the cavity was set at too high a level for this particular set of data). The corresponding visibility in the HOM type interferometer, after having corrected for background, is thus only $V_{2ph} = 0.69$.

relation curves of the completely distinguishable and completely indistinguishable cases:

$$V_{2ph} = 1 - \frac{\int \Phi_{\parallel}(\tau)\,\mathrm{d}\tau}{\int \Phi_{\perp}(\tau)\,\mathrm{d}\tau}, \tag{4.15}$$

where $\Phi_{\perp}(\tau)$ and $\Phi_{\parallel}(\tau)$ are the cross-correlation distributions for perpendicular and parallel polarised photons as functions of the detection time delay τ. This definition allows for the comparison of the experiment with non time-resolved HOM arrangements, (i.e. the depth of the $\tau = 0$ dip in a non time-resolved HOM), as the extra information is simply averaged away. We observe a visibility of $V_{2ph} = 0.87 \pm 0.05$. Taking only the central data points at zero detection-time delay ($\tau = 0$) results in a visibility of $V_{2ph} = 0.96 \pm 0.06$.

This compares very favourably to the visibilities previously achieved with photons from atom-cavity systems ($V_{2ph} = 0.77$, [79]), quantum dots ($V_{2ph} = 0.81$, [95]), individual trapped ions ($V_{2ph} = 0.89$, [107]), single molecules ($V_{2ph} = 0.24$, [100]) and individual NV centres ($V_{2ph} = 0.35$, [99]). However, parametric down-conversion sources with appropriate spectral and temporal filtering have exhibited visibilities exceeding 0.99 [108]. High visibilities are obviously of paramount importance for sources which one intends to use for quantum information processing and networking. It is expected that the visibility of the source could well be improved upon with some optimisation of the experimental apparatus, and post-selecting only on well coupled atoms could well have a meritorious effect on this figure.

4.7 The Quantum Beat between Two Photons

We turn now to the possibility of producing alternating photons of differing frequencies, as looked at in section 4.5.3. Given that the photons are the product of a Raman process, and the cavity has some finite linewidth, it can be immediately seen that some degree of control over the frequency is possible: that is assuming, of course, that the laser linewidth is significantly smaller than that of the cavity (in this case, 100 kHz and 12 MHz for the laser and cavity linewidths, respectively). Through a simple conservation of energy argument, it is obvious that the linewidth of the photon is defined by the linewidth of the driving laser. Fig. 4.21 shows a schematic of the relevant levels involved, with the Lorentzian transmission peak of the cavity shown on the right. The scope of frequency difference which is achievable is thus essentially just a function of the cavity linewidth.[8]

For the experiment, successive photons are produced from the atom cavity system with different frequencies. This is achieved by driving the atom with successive pump pulses tuned above and below the atomic transition, respectively. Thus, any pairs of photons overlapping on the beamsplitter will have a frequency difference given by 2Δ.

[8] This is true for cases where the cavity linewidth is much smaller than the splitting between levels in the upper hyperfine manifold, for instance, although one could also be limited in practise by the limitations of producing pump beams at the requisite frequencies, etc.

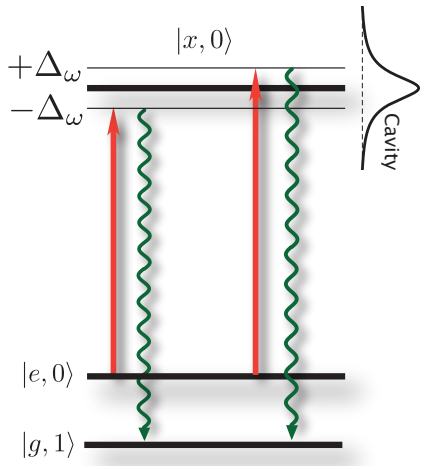


Figure 4.21 Some degree of control over the frequencies of the emitted photons is possible. The condition is such that the photons have to fall within the linewidth of the cavity. Moving further away from the cavity resonance will have the effect of reducing the effective value of g_{eff}, thus rapidly decreasing the photon production efficiency.

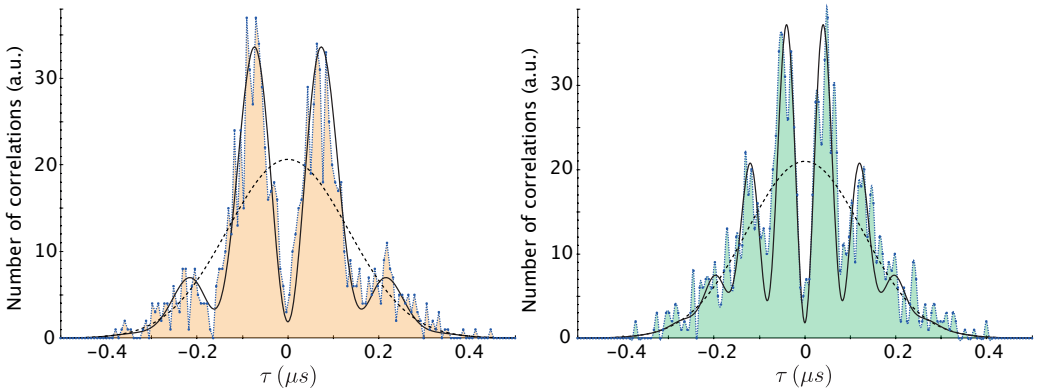


Figure 4.22 Results from a Hong-Ou-Mandel type interferometer for sequential photons with differing frequencies ($2\,\Delta = 6\,\text{MHz}$ and $2\,\Delta = 12\,\text{MHz}$) and widths of $\delta t = 0.18\,\mu\text{s}$. The expected plots for photons of perpendicular polarisation are shown by the dotted lines, whilst fits to the data for coherence time, T_c, are shown by the solid lines. The fits yield values of $T_c = 0.18\,\mu\text{s}$ and $T_c = 0.17\,\mu\text{s}$, agreeing well with those results obtained with photons of the same frequency. In order to account for a small mode mismatch, a value of $\psi = 0.3$ has been used. Fitting for the frequency difference gives values of $2\,\Delta = \{6.23, 11.56\}\,\text{MHz}$, in good agreement with the defined detuning.

The results, as shown in Fig. 4.22, show clearly that control over the frequency of the photons is possible. The expected interference pattern demonstrating the oscillation or 'quantum beat' between the two photon wavepackets is clearly visible.

It is clear that the initial superposition state evolves coherently with time. Fits to the data yield coherence times of 0.18 ± 0.03 and $0.17 \pm 0.04\,\mu$s, which are slightly smaller than the coherence time values obtained for identical photons.

4.8 Conclusion

This chapter has described the process of characterising the single photon source. The optimisation of a number of the working parameters of the system was detailed, before the theoretical background to the Hanbury Brown and Twiss interferometer, and a description of its experimental implementation, was given. It was shown that the source exhibits highly sub-Poissonian photon statistics ($g^{(2)}(\tau) < 0.05$), if one conditions on the presence of an atom in the cavity. A Monte-Carlo simulation of atoms entering the cavity, and a detailed analysis of the photon emission statistics per atom, demonstrated the validity of the atom conditioning method. An analysis of time-resolved interference using a Hong-Ou-Mandel interferometer showed that the photons exhibit excellent indistinguishability, with a measured visibility of $87 \pm 5\,\%$. The coherence time of the photons was found to reach $T_c = 410 \pm 30\,$ns. Finally, it was shown that it is possible to control, to a certain extent, the frequency of the photons emitted from the cavity, and that these interfere coherently in a time-resolved manner.

Chapter 5

Photon Shaping

This chapter documents the theoretical background and experimental implementation of the photon shaping algorithm proposed in [72]. Inverting the rate equations describing the dynamics of the atom-cavity system allows one to derive an analytical expression for the time-dependent Rabi frequency needed to produce photons of near-arbitrary, user prescribed temporal shape. The algorithm for obtaining this expression is outlined in section 5.1. Sections 5.2 and 5.3 consider the specified emission efficiency of the process, and the effects of variations in the value of g. It is shown in section 5.4 that photons of near arbitrary temporal shape can be produced from the atom-cavity system, agreeing excellently with theory.

5.1 Photon Shaping

In Chapter 2, the basic STIRAP mechanism utilised for producing single photons was outlined. Under the right circumstances, the application of a time-varying control field allows the production of a single photon from the atom-cavity system. It is perspicuous that the amplitude profile of the emitted photons is determined by the temporal shape of the driving pulse. There are many potential applications whereby a high degree of control over the amplitude profile of the single-photon pulses would be desirable. As discussed in Chapter 8, photons promise the experimentalist an information carrier and computational qubit of great flexibility in potentia. In atom-cavity based quantum networking schemes, where states can be mapped from atom to photon and vice versa, ultimate control over the light-matter interface is obviously of great importance. For instance, in order to realise the state mapping proposal of Cirac et al. [16], it had been posited that symmetric photons were needed to achieve a time-reversal of the emission process. In actuality, this is not the case, although there exist numerous proposals in which control over the temporal mode of photons plays a fundamental role. The promise of LOQC with photons of long temporal duration means that command over the temporal shape could be greatly beneficial, and it has also been shown that certain wavepacket shapes can help with

tolerance against mode mismatch: photons with Gaussian temporal envelopes [1] have been demonstrated to be the most robust when considering two-photon interference on a beam splitter, for example [109]. This could well have importance for achieving high fidelities in certain QIP operations. Further, photons with soliton amplitude profiles could also help minimise dispersion during photon propagation in optical fibers.

Work investigating the temporal shaping of single-photon wavepackets in the context of parametric down-conversion sources [110–112] and quantum dots [113, 114] has been demonstrated. Up until this point, however, no thorough examination of photon shaping in the context of atom-based cavity-QED has been carried out.

In the earliest demonstrations of single-photons produced via the mechanism of coherent population transfer, the applied driving field was relatively simplistic: a linear ramp in Rabi frequency, for example, has been used to produce single photons with amplitudes *somewhat* symmetric in time [75, 77] whilst pulses with constant Rabi frequency have additionally been used [115]. Other implementations have utilised driving pulses with $\sin^2(t)$ [79] or Gaussian [116] time dependencies to good effect.

More sophisticated attempts to shape the photons' wavefunctions centre around a recursive feedback method [117], whereby a given driving pulse is assumed and the time-dependent Schrödinger equation (TDSE) solved to find the corresponding photon output. Iteratively optimising the control field using this method leads to a driving pulse which, when applied to the atom-cavity system, produces a single photon with the desired amplitude.

The most extensive experiment detailing single-photon shaping in C-QED is found in [118], where a stream of photons of different shapes were produced from an ion trapped in an optical cavity. However, no work was done on optimising the driving pulse to achieve shaping of the single photons pulses; rather, some relatively complex driving pulses were applied to the ion and the results shown to be consistent with a full numerical simulation of the system. Here we present an analytical method, based on the work presented in [72], which allows one to calculate the driving pulses required to produce photons of near arbitrary shape from atom-cavity systems. What we desire is some method which, upon specifying a single-photon pulse shape, will produce a direct analytical expression describing the time-dependent Rabi frequency of the driving pulse needed to produce said photon. As will be described in the upcoming section, there is indeed a robust, elegant and applicable mechanism which allows us to achieve the above goal.

As previously explicated, three of the main parameters dictating the dynamics of the coupled atom-cavity system, g, κ and γ, are generally static during the production of a photon. The free space decay rate, γ, is dependent only upon the species of atom chosen for the experiment, and the others are essentially impossible to modulate on a timescale comparable to the photon time.[2] Thus, the only parameter

[1] The phrases 'shape' and 'amplitude' are used here in a generally interchangeable manner, and both refer to the form of the time-dependent probability amplitude of the photon.

[2] This is in contrast to optimal pulse shaping for the storage of photons in EIT-based schemes,

which we may reasonably control is the driving laser field and its Rabi frequency, $\Omega(t)$.

We now again consider a three-level lambda-type atom in an optical cavity. We take the three time dependent probability amplitudes $c_e(t)$, $c_x(t)$ and $c_g(t)$ describing the occupation of the states $|e,0\rangle$, $|x,0\rangle$ and $|g,1\rangle$ and arrive at the time-dependent Schrödinger equation (TDSE):

$$\begin{pmatrix} \dot{c}_e \\ \dot{c}_x \\ \dot{c}_g \end{pmatrix} = \begin{pmatrix} 0 & -i\Omega(t)^*/2 & 0 \\ -i\Omega(t)/2 & -\gamma & -ig \\ 0 & -ig^* & -\kappa \end{pmatrix} \begin{pmatrix} c_e \\ c_x \\ c_g \end{pmatrix}. \tag{5.1}$$

We define the wavefunction of our desired single photon, upon emission from the cavity, as:

$$\phi_{ph} = \sqrt{\eta}\phi_0(t), \tag{5.2}$$

where η is the total efficiency of the single photon emission process, and $\phi_0(t)$ the normalised single photon wavefunction (further discussion of the pre-factor η is given in section 5.2). We can relate the photon wavefunction outside the cavity to the probability amplitude of the state $|g,1\rangle$ inside the cavity by

$$c_g(t) = \phi_{ph}(t)/\sqrt{2\kappa}, \tag{5.3}$$

as we know that there is only one state in which there is a photon occupying the cavity field mode. The result arises naturally if one considers the decay of a single photon from an optical cavity, given one mirror with a unit reflectivity.

From the Schrödinger equation, we find

$$c_x(t) = i\left[\dot{c}_g(t) - \kappa c_g(t)\right]/g^*, \tag{5.4}$$

and, from the fact that there are only two decay channels, we obtain:

$$\rho_{ee}(t) = 1 - \rho_{xx}(t) - \rho_{gg}(t) - \int_{-\infty}^{t} [2\kappa\rho_{gg}(t) + 2\gamma\rho_{xx}(t)]dt. \tag{5.5}$$

The elements $\rho_{ii}(t) = c_i^* c_i$ are the state populations, i.e. the diagonal elements of the density matrix. As we have already intimated, because the atom-cavity detuning is set to zero, both $c_g(t)$ and $c_e(t)$ can be taken to be real, whilst $c_x(t)$ is purely imaginary. This allows us to couch the probability amplitude $c_e(t)$ in terms of its respective population

$$c_e(t) = \sqrt{\rho_{ee}(t)}. \tag{5.6}$$

Eqs. (5.3) to (5.6) provide expressions for all of the requisite probability amplitudes of the states of interest. From here, we can straightforwardly obtain an expression for the time-dependent Rabi frequency, $\Omega(t)$, given the desired photon wavefunction $\phi_{ph}(t)$:

$$\Omega(t) = -2i\frac{\dot{c_e}(t)}{c_x(t)} = -i\frac{\dot{\rho_{ee}}(t)}{c_x(t)\sqrt{\rho_{ee}(t)}}. \tag{5.7}$$

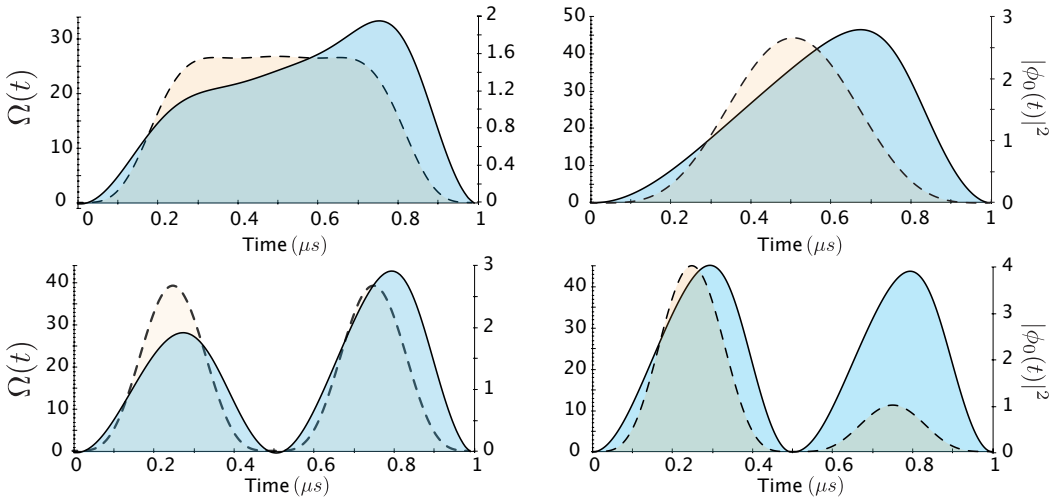


Figure 5.1 Some interesting photon shapes with corresponding driving pulses. For all plots, dashed lines (yellow) show the desired photon wavefunction and solid lines (blue) the required driving frequency $\Omega(t)$. Clockwise from top left: pseudo-top hat photon, modelled by $\phi_{ph}(t) = \sqrt{\eta}\sqrt{\frac{10}{9T}}\left(\sin^2(2\pi t/T) + 1.19\sin^7(\pi t/T)\right)$; $\sin^2$(t); twin peak $\sin^2$(t); asymmetric twin peak with $\sin^2$(t) dependence. The photons all have a length of $1\,\mu$s, with their wavefunctions $\phi_0(t)$ shown by dotted line.

In practice then, what we have derived is an analytical expression [3] which describes how one should drive an atom-cavity system in order to emit a photon with a pre-defined wavefunction of almost arbitrary shape. Further discussion of the limitations and scope of the above scheme are to be found in [72].

5.2 Efficiency

Eq. (5.2) introduces the parameter η, defined as the overall probability for photon emission from the cavity. Given that excitation is conserved, and that there are only two possible decay channels, any excitation not finally contained in the emitted photon is patently distributed between the initial state $|e,0\rangle$ and loss arising from spontaneous emission. In an ideal system which adiabatically follows the dark state $|\phi^0\rangle$ throughout, all of the excitation initialised in the state $|e,0\rangle$ may be transferred to $|g,1\rangle$ and thus be emitted as a photon leaving the cavity, i.e. the emission probability is equal to 100%. However, on the edge of strong-coupling and adiabaticity

for example [20, 119]. Furthermore, there has been work documenting the solution to the discussed problem in relation to STIRAP [120] where one can control the time-varying amplitudes of both the control and the pump beams.

[3] Of course, although this scheme is put forward analytically, it is trivially possible to perform the same operation numerically if it is so desired.

(see section 2.2.2), the system no longer follows exactly the dark eigenstate $|\phi^0\rangle$. The excited state $|x, 0\rangle$ in fact does become populated during state transfer from e to g, and population is inexorably lost from the coherent photon generation process. How trivial or problematic this loss mechanism is depends obviously on the parameters of the atom-cavity system in question.

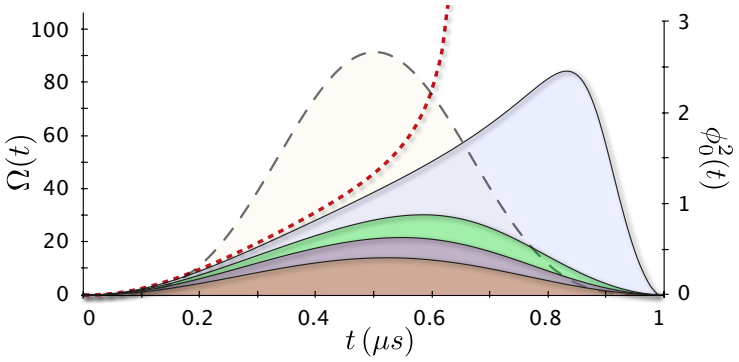


Figure 5.2 Showing the variation in driving pulse with desired efficiency. The atom-cavity system parameters reflect the present set-up. The left axis shows the Rabi frequency of pump pulses required to produce a $\sin^2(t)$ shape at various efficiencies: {orange, purple, green, blue, red} $\rightarrow$ $\eta = \{0.2, 0.4, 0.6, 0.86, 1\}$. The desired photon pulse is shown by the dashed black line (right axis).

Fig. 5.2 shows the derived driving pulse required for a $\sin^2(t)$ photon pulse shape for efficiencies ranging from $\eta = 0.2 \rightarrow 1$. As can be seen, for low efficiencies the initial population is not greatly depleted, and the driving pulse follows the shape of the photon quite closely. As demands on the efficiency increase, the driving pulse begins to become more asymmetric. This can simply be explained by the fact that, as the population in the state $|e, 0\rangle$ is depleted during the photon production, the system needs to be driven more strongly in order to keep proportionally the same rate of population transfer throughout the photon emission time. When the efficiency requirements become overly demanding, i.e. the emission probability exceeds unity, or spontaneous loss from the upper excited state depletes too much population from the system, then the required Rabi frequency encounters a singularity: this situation is illustrated clearly by the dotted line in Fig. 5.2.

5.3 Variation of g

It is assumed that g does not change over the timescale of a single photon emission: an atom-cavity interaction time of around $100\,\mu s$ leads to a maximum variation in g of a few percent over the photon pulse lasting $0.5\,\mu$s. It is clear, however, that the value of g which an atom experiences as it traverses the cavity mode varies from $0 \rightarrow g_{max}$. This variation in g will generally affect the wavefunction of the emitted

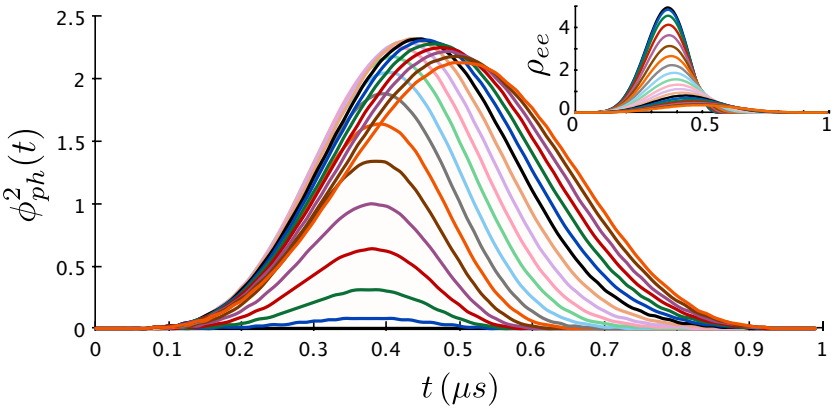


Figure 5.3 Plot illustrating the variation in photon shape for an atom experiencing different values of g_{eff}

photon. Fig. 5.3 illustrates this effect. A driving pulse optimised for the production of $\sin^2(t)$ photon pulses with an effective value of $g = 2\pi \times 15\,\text{MHz}$ is applied to the system with the atom experiencing a range of g values, from $2\pi \times \{1 \rightarrow 15\}\,\text{MHz}$. As can be seen, both the photon shape and the overall production probability change substantially. For atoms experiencing a lower value of g, the photon emission generally occurs earlier in the pulse: for these cases the Rabi frequency of the driving pulse greatly exceeds that required for the given atom-cavity coupling and the population transfer from $|e\rangle$ to $|g\rangle$ is no longer sustained (generally speaking, the population is lost from the system through radiative excitation from the excited state $|x\rangle$, as shown in the inset). It can be seen from Fig. 5.3 that both the width of the emitted photon and its temporal distribution change. The general shape stays approximately similar however, and the variation in output could well be modelled by a jitter in photon arrival times, in reference to section 4.5.4.

5.4 Experimental Verification

The experimental investigation of the photon shaping algorithm is investigated in the following way: using the same set-up as is implemented for the Hanbury Brown and Twiss interferometer (shown in Fig. 4.7), the photon stream emitted from the cavity system is fiber coupled and sent through a 50/50 NPBS. The outputs of the NPBS are interrogated with photon counters, and the detection events collated and binned into histograms showing the detection event times relative to the start of the driving pulse. Driving pulses for a selection of desired photon shapes, $\phi_0(t)$, are calculated for a given efficiency using the relevant atom-cavity parameters. These are loaded onto the AWG, with the linearity of the AOM's amplitude response ensured through careful calibration and interpolation. The repetition rate, repump

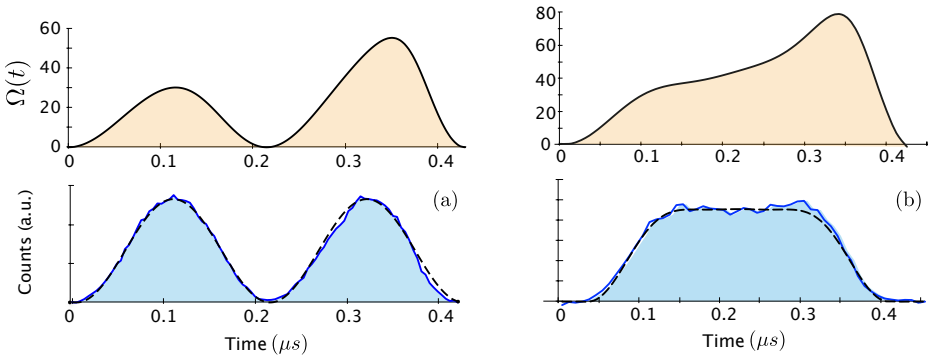


Figure 5.4 Showing the experimentally measured temporal profile of two different photon shapes with their corresponding analytically calculated driving pulses. Plot (a) shows the experimentally measured envelope for twin peak photons after a total of *circa* 10^5 detection events. The dashed line is a $\sin^2(t)$ line of best fit to the measured histogram data. Plot (b) shows the same plot for a pseudo-top hat photon, of the form given in Fig. 5.1, for *circa* 6×10^4 measured photons.

characteristics, MOT loading and fountain launching parameters are retained from previous correlation measurements.

Fig. 5.4 shows a selection of photons produced using the above method. It can be seen that excellent agreement between the desired photon shape and experiment is obtained. Both sets of data have had a constant background level contribution removed. The $g^{(2)}(\tau)$ for each data set is checked to ensure single-photon production, and agree well with previous results. It is worth noting that the shaping method uses a somewhat simplistic model of the atom, without the inclusion of extra levels in the upper hyper-fine manifold or Zeeman sublevels, for example. In order to investigate the validity of the scheme, a full numerical simulation of the photon emission process, including both the relevant magnetic sublevels and excited states, was carried out [85]: an analytically calculated driving pulse, $\Omega(t)$, was taken and the emitted photon shape $\phi_{ph}(t)$ calculated numerically. The resultant photon shape varied from that desired by only a few percent, sufficiently quashing any doubts as to the model's validity. Further, the experimental results shown here seem to justify sufficiently this assumption. The overlap between the experimental data and the desired photon shapes can be calculated by examining the similarity, defined as $S(p_x, q_x) = \left(\sum_x \sqrt{p_x q_x}\right)^2 / \left(\sum_x p_x \sum_x q_x\right)$. For both the twin peak and square pulse shown in Fig. 5.4, $S > 99\%$.

It is possible to produce photon wavefunctions of even greater complexity: a number of these are shown in Fig. 5.5, and it should be noted that the lengths of the bottom two photons are correct to within an order of magnitude. It can be seen that there is some degree of smoothing present on the shapes of the detected photons. This is a direct result of limitations imposed by the finite bandwidth of

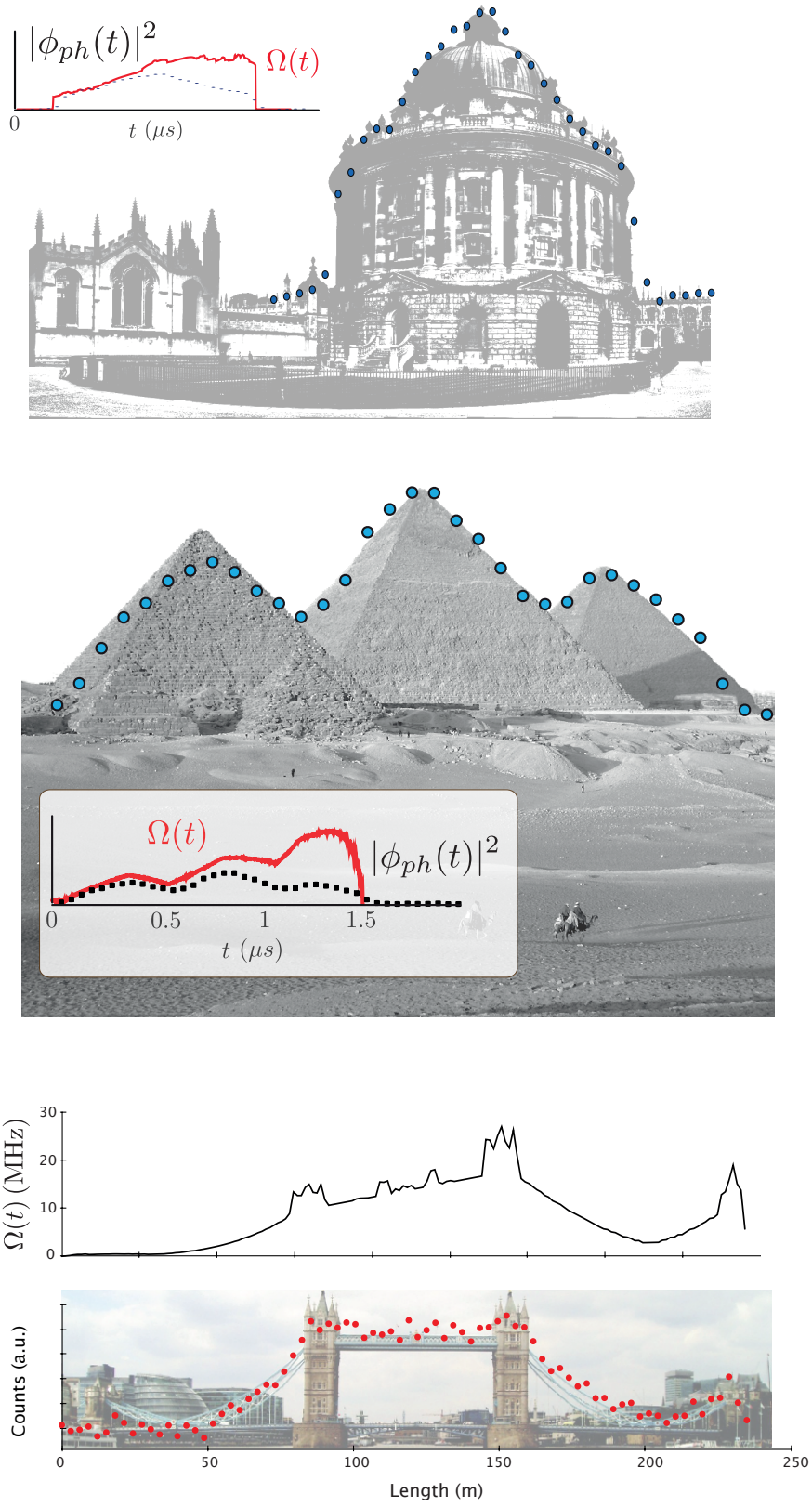


Figure 5.5 Various landmarks reproduced with single photon wavepackets. The respective driving pulses are shown inset for each plot.

the AOM used to produce the driving pulses (around 6 MHz). This is simply a practical limitation however, with the ultimate bottleneck provided by the atom-cavity coupling, g. It is clear that this represents a significant advancement relative to previous achievements in the realisation of amplitude control of single-photon wavepackets.

5.5 Conclusion

In the beginning of this chapter, a method for exerting precise control over the amplitudes of the photons emitted from the cavity system was outlined. It was shown that applying these analytically calculated control pulses to the experimental atom-cavity system results in the desired single-photon amplitudes. It is expected that this could greatly increase the suitability of atom-cavity systems for uses in LOQC and some quantum networking applications. It is interesting to note that the twin peak photon shown in Fig. 5.4 is an example of a possible implementation of *time-bin encoding*. Given that there is a 50% probability of finding the photon within either time-bin, the photon's wavefunction can be written as $|\Psi\rangle = \frac{1}{\sqrt{2}}(|01\rangle + |10\rangle)$, where $|01\rangle$ and $|10\rangle$ relate to finding the photon within the first or second time-bin. Depending on the relative heights of the peaks (or more properly the area beneath them individually), it can be seen that this is easily extendable to encoding arbitrary superposition states of the form $|\Psi\rangle = \alpha|01\rangle + \beta|10\rangle$. The potential benefits of this are discussed in the subsequent chapter.

Chapter 6

Phase

We turn now to the possibility of encoding arbitrary quantum information onto our single photons during their generation, and discuss how these could be useful in the context of quantum information processing. The preparation of single qubits for use in LOQC is generally achieved through dual-rail encoding, where superpositions of photon number states are generated (the vacuum state and single-photon Fock state, for instance). Photons, however, offer numerous degrees of freedom in which it might be possible to encode quantum information. Section 5.4 demonstrated how control over the amplitude of photon pulses might be instigated: specifically, it was shown how it is possible to distribute a single photon between a number of time bins, each with adjustable probability amplitudes. In order to encode arbitrary qubits onto these photons however, it is be necessary to additionally garner control over the relative phase between these time bins. Given that the photon wavefunction is dynamically determined solely by the properties of the driving laser, it is perhaps not too naive to assume that modulation of the control beam's phase should lead to a de facto modulation of the photon's internal phase.[1]

Previously, it has been shown that it is possible to modulate the relative phase [121] and amplitude [114, 122] of a single-photon wavepacket with an electro-optic modulator after its production. However, any secondary amplitude modulation of the photonic wavepacket is generally a lossy mechanism (with some exceptions), and it could well be advantageous to exert control over the photons' phase upon emission. One experiment investigating the interference of 'quantum camels' (i.e. twin peak photons) generated from a PDC source with the use of birefringent plates has been demonstrated [123], although with the promise of limited scope. Consequentially, no source has yet exhibited sufficient temporal control over the photonic wave packet - coupled with suitably long coherence times - to allow investigation into the control over both the amplitude and phase simultaneously.

This chapter first describes how the phase of the photons emitted from the cavity system is investigated. The expected behaviour of these photons in the context of the

[1] In fact, the coherent evolution of the superposition states demonstrated for photons of distinct frequencies (section 4.7) demands this interpretation.

Hong-Ou-Mandel interferometer is then discussed, with corresponding experimental results presented in Section 6.2.

6.1 Two-Photon Interference with Variable Phase

We turn now to the interference of twin-peak photons in the Hong-Ou-Mandel interferometer. A schematic is shown in Fig. 6.1. Photons are emitted from the cavity in an alternating sequence: 'reference' photons (with fixed phase relationships throughout) are followed by the generation of 'signal' photons with the requisite phases encoded between time bins. If a photon, travelling down the delay line, is subsequently followed by one travelling directly to the beam splitter, the two will be brought together and interfere. This technique can be thought of single photon 'quantum homodyning', where the local oscillator (LO) is replaced by a reference photon with whom the signal photon interferes [124].

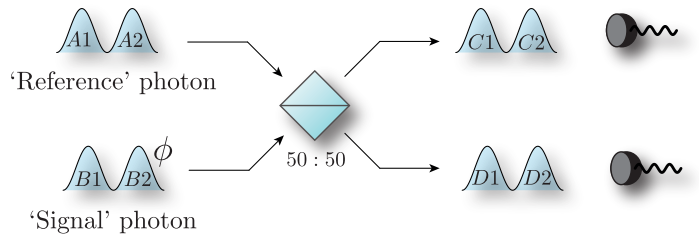


Figure 6.1 A schematic depicting the twin peak field modes and their respective time bins.

Simply, the action of a relative phase between time bins can be interpreted as follows: the two photons interfere at the beam splitter, and an initial click at port C or D collapses the initial joint product state of the two photons, leaving a reduced 'which-path' quantum superposition state. As before, we aim to examine the joint probability distribution function of obtaining a click on, e.g. detector D, given a click on detector C, although we now take into account both time bins and phase shifts. For identical photons the situation is obviously the same as that presented in section 4.5.2, that is, both photons will coalesce and leave through the same output port, regardless of which bins they are detected in. In terms of the time-resolved HOM measurement, the joint detection probability distribution is simply determined, once again, by the convolution of the two photon shapes. When the reference photon and signal photon with imprinted phase interfere, they behave quantitatively differently. Again, because the relative phase is defined only upon the projection of the joint state into a superposition, i.e. upon the detection of a photon, photons detected within the same time bin will always exit through the same port. Patently however, photons detected in opposite time bins will have some relative phase relationship, ϕ, between their respective wavefunctions, and may thus exit distinct output ports

of the beam splitter. Writing this out explicitly, we can express the reference and signal photons as two qubits:

$$|\psi_1\rangle = \frac{1}{\sqrt{2}}\Big(|01\rangle + |10\rangle\Big), \quad |\psi_2\rangle = \frac{1}{\sqrt{2}}\Big(|01\rangle + e^{i\phi}|10\rangle\Big), \tag{6.1}$$

or, in terms of creation and annihilation operators

$$|\psi_1\rangle = \frac{1}{\sqrt{2}}\Big(\hat{a}^\dagger_{A1} + \hat{a}^\dagger_{A2}\Big), \quad |\psi_2\rangle = \frac{1}{\sqrt{2}}\Big(\hat{a}^\dagger_{B1} + e^{i\phi}\,\hat{a}^\dagger_{B2}\Big). \tag{6.2}$$

Applying the beamsplitter transformation to the two states gives us

$$|\psi_1\rangle = \frac{1}{2}\Big[\Big(\hat{a}^\dagger_{C1}+\hat{a}^\dagger_{D1}\Big)+\Big(\hat{a}^\dagger_{C2}+\hat{a}^\dagger_{D2}\Big)\Big], \quad |\psi_2\rangle = \frac{1}{2}\Big[\Big(\hat{a}^\dagger_{C1}-\hat{a}^\dagger_{D1}\Big)+e^{i\phi}\Big(\hat{a}^\dagger_{C2}-\hat{a}^\dagger_{D2}\Big)\Big]. \tag{6.3}$$

Taking the tensor product to find the remaining product state, it can be readily seen that the terms corresponding to both photons being detected in the same time bin by opposite detectors have been cancelled out, and we are left with

$$\begin{aligned}&(\hat{a}^\dagger_{C1})^2 - (\hat{a}^\dagger_{D1})^2 + e^{i\phi}\big((\hat{a}^\dagger_{C2})^2 - (\hat{a}^\dagger_{D2})^2\big)+\\ &(1+e^{i\theta})\hat{a}^\dagger_{C1}\hat{a}^\dagger_{C2} - (1+e^{i\theta})\hat{a}^\dagger_{D1}\hat{a}^\dagger_{D2} + (1-e^{i\theta})\hat{a}^\dagger_{C1}\hat{a}^\dagger_{D2} - (1-e^{i\theta})\hat{a}^\dagger_{C2}\hat{a}^\dagger_{D1}.\end{aligned} \tag{6.4}$$

The first four terms in this equation refer to both photons leaving the beam splitter in the same spatio-temporal mode. The bottom line refers to photons detected in opposite time bins, with clear phase dependence. We find that the probability of detecting the photons in opposite output ports is directly related to the magnitude of this applied phase:

$$P_{3,4} = \sin^2(\phi/2). \tag{6.5}$$

The two extrema, $\phi = 0$ and $\phi = \pi$, correspond to the photons detected in adjacent time bins leaving through either the same or opposite output ports, respectively. The photons can in fact be forced to behave 'quasi-fermionically', as the application of a π phase flip to one of the photons ensures that they leave through different ports if detected in adjacent time bins.

6.2 Results

6.2.1 Qubits

Fig. 6.3 shows normalised correlation distributions as a function of detector time delay, τ, obtained from the Hong-Ou-Mandel interferometer when a sequence of 'signal' and 'reference' photons are emitted from the cavity. It is clear that the magnitude of the applied phase directly affects the joint probability distribution function.

Fig. 6.4 shows the relative heights of the side peaks for different values of ϕ. As expected, maxima and minima in the number of detected coincidences are present

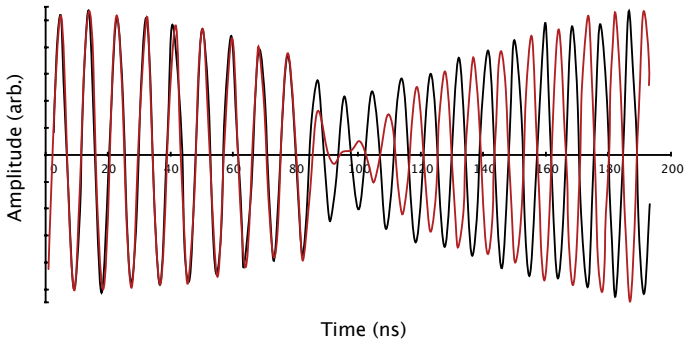


Figure 6.2 The experimentally measured relative phases of the control pulses used to drive the atom cavity system. The measurements are made with a high speed balanced homodyne detector. Black line: no phase change, Red line: π phase change. Figure from [85].

for values of $\phi = 0$ and $\phi = \pi$, respectively. Obviously, if the two photons are detected within the same time bin, then they behave bosonically and coalesce. The maximum number of coincidences obtained with an applied phase shift of $\phi = \pi$ should equal twice the number for non-interfering photons, illustrating the quasi-fermionic behaviour of the photons. In reality, the achieved visibility and number of coincidences are slightly less than the ideal. This can be explained fully by the joint decoherence time of the photons, as discussed in Section 4.6, and the fact that there is some imperfect state preparation. This imperfect state preparation manifests itself in the inability to prepare a superposition state with probability amplitudes exactly equal to $\alpha = \beta = 1/\sqrt{2}$ (which is desired for this particular case). Again, the variability of the shot-to-shot amplitude of the photon wavefunction is a significant contributing factor. Fluctuations in the Rabi frequency of the driving pulse, and the aforementioned variation in g_{eff} both combine to alter the relative distribution of the photon between the two time bins.[2] Nevertheless, even with this imperfect state preparation, the results show good agreement with the ideal. The data are again normalised with respect to the total number of photons detected in the ± 1 peaks of the $g^{(2)}$ correlation function.

One may interpret the experimental set-up in another way (where we move from a picture in the temporal domain to one in the spatial domain), which allows for visualisation of the complexity of the 'quantum circuits' achievable with the implementation of time-bin encoding. A quantum photonic circuit equivalent to the current twin-peak photon interference experiment is illustrated in Fig. 6.5. The left hand of the circuit represents the photon production inside the cavity: the two photon number state modes, (i.e. the vacuum state and $|n = 1\rangle$), which correspond respectively to the first and second time bins, are entangled by being brought to-

[2]The problem is exacerbated with the introduction of greater numbers of time bins, as it becomes more difficult to properly prepare the desired superposition state.

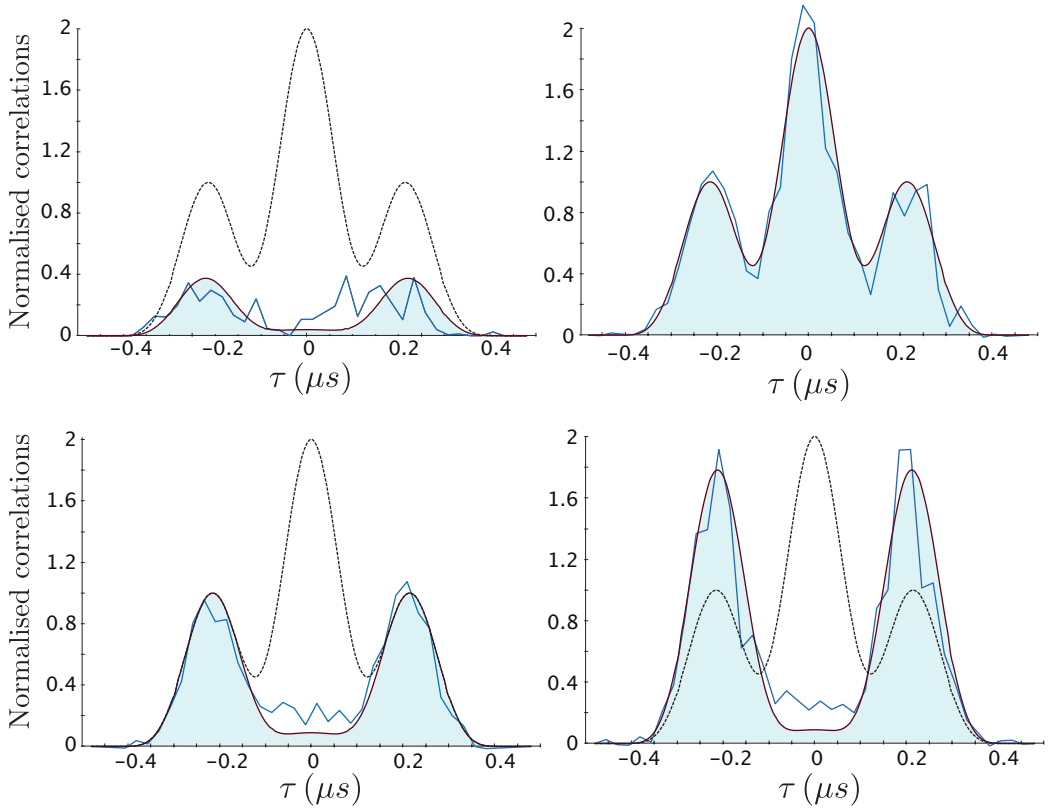


Figure 6.3 Photon coincidences as a function of detection time-delay for twin-peak photons with an arbitrary phase applied. The expected values for non-interfering photons (perpendicular polarisation) are shown in all plots by the dashed line. Top left: parallel polarisation, no applied phase. Top right: perpendicular polarisation. Bottom left: parallel polarisation, $\phi = \pi/2$. Bottom right: parallel polarisation, $\phi = \pi$. For convenience, the data are normalised to ensure the height of the side-peaks in the perpendicularly polarised case is equal to one (i.e. with parallel polarisation and an applied phase of $\phi = \pi$ one expects to see twice the number of reference counts). As can be seen, the heights of the two side peaks change dramatically with the applied phase.

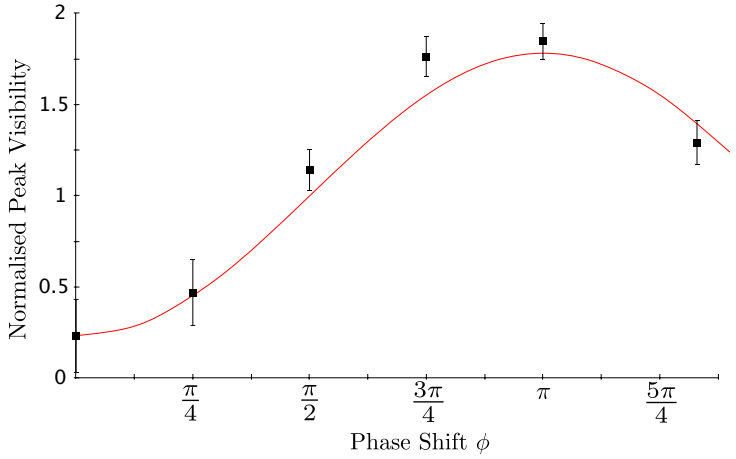


Figure 6.4 Data showing the respective peak heights obtained for values of applied phase. The red line is a sinusoidal fit to the data, showing the expected $\sin^2((\phi/2)$ dependence.

gether on a beam splitter.[3] Both photons are illustrated in this way. The right hand side then represents the physical beamsplitter present in the apparatus where the photons are combined. Detectors $C1$, $C2$, $D1$ and $D2$ represent the detectors firing in the relevant time bin. Furthermore, adding some relative phase is easily depicted in the diagram.

It can readily be seen that a single beam splitter and two detectors in the temporal domain are already equivalent to four beam splitters and four detectors working in the spatial domain. In this particular case, increasing the number of time bins, n, is thus equivalent to increasing the number of beam splitters (to $2(n-1)+n$) and detectors ($2n$), without in reality introducing any great experimental overhead.[4] This is one obvious advantage of the method here propounded in comparison to, for example, PDC based sources which often require physical beam splitters to generate state superpositions.

In direct relation to the discussion of equivalent circuits, one can extract individually the number of correlations obtained between different time bins. Fig. 6.6 shows a visualisation of the distribution of cross-correlation detection events for two twin-peak photons interfering on a beamsplitter. The bins correspond to detection in time bins one and two for detectors C and D, respectively. It should be noted that it is not possible to examine the auto-correlations between clicks on the same detector due to significant after-pulsing of the APDs and their non-trivial dead-time ($\sim 100\,\mathrm{ns}$).[5]

[3] In theory, a photonic time-bin superposition state of any arbitrary dimension can be generated inside the cavity in this way.

[4] Shorter time bins obviously increase the demands on detector and source bandwidths, however.

[5] In the limit of photons with a duration much greater than the dead-time of the detectors this problem would also be nullified. After-pulsing is a well-known artefact of APD-based counters, and

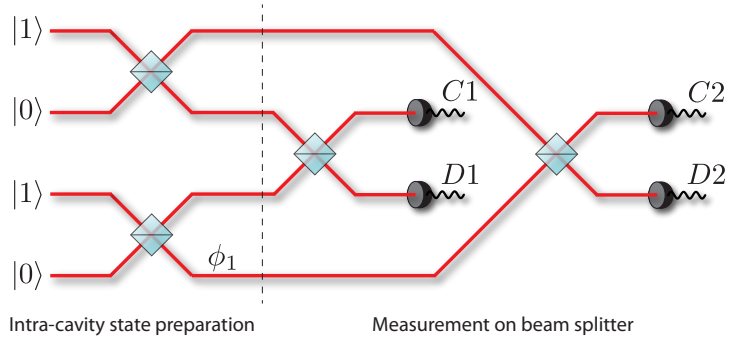


Figure 6.5 Equivalent quantum circuit representing two twin peak photons interfering on a beam splitter. The reference photon (top left) is generated with a stable phase, whilst the signal photon (bottom left) has some arbitrary relative phase encoded between its two constituent rails.

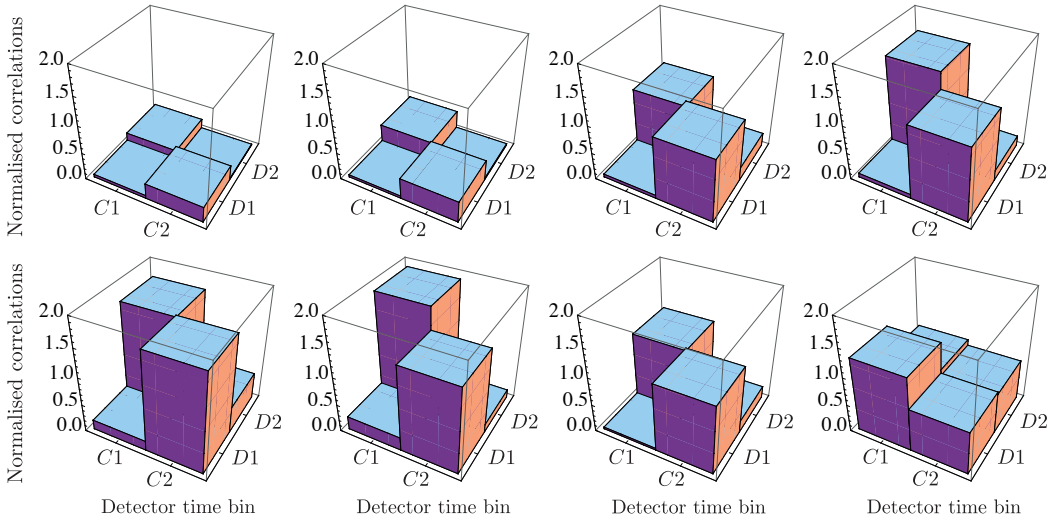


Figure 6.6 Bar charts showing the experimentally measured, normalised distribution of cross-correlations between the two time bins for both detectors. From top left, $\phi = \{0, 1/4, 1/2, 2/3, 3/4, 1, 4/3\}\,\pi$. Bottom right shows perpendicular polarisation.

6.2.2 Fidelity

The fidelity of the time bin encoded qubit state preparation can be calculated by examining the correlation data for both the perpendicular and parallel polarised photons. The density matrix of the state may be reconstructed [85, 125], and the fidelity calculated through $F(\hat{\rho}, \hat{\sigma}) = (Tr(\sqrt{\sqrt{\hat{\rho}}\hat{\sigma}\sqrt{\hat{\rho}}}))^2$. For the qubit with $\phi = \pi$,

could be potentially be overcome by instead using another type of detector.

the fidelity is found to be $F = 0.93$.

6.2.3 Qutrits

We turn now to an extension of this qubit preparation and ask if it is possible to extend the number of time bins to even greater number, that is to say, to prepare qutrits, ququads and so forth. In theory, the photon production algorithm has no upper bound to the number of time bins over which one can distribute a single photon: it is possible to calculate analytically the driving pulse needed to produce a photon occupying an arbitrary number of time bins. Practical limitations however (i.e. the AOM bandwidth), ensure that the efficiency of production for much higher dimension photon states becomes too low to implement viably in experiment. For the two-photon interference to be meaningful, the temporal length of the photons must obviously not exceed too greatly their characteristic coherence time, T_c, in the Hong-Ou-Mandel interferometer. Additionally, the number of peaks it is possible to produce within a given time is limited by the fundamental characteristics of the atom-cavity system (i.e. the rates of g and κ). Nevertheless, it is patently instructive to investigate experimentally the ability of the atom-cavity system to produce such photon states. Most naturally, we now discuss the production of photons distributed

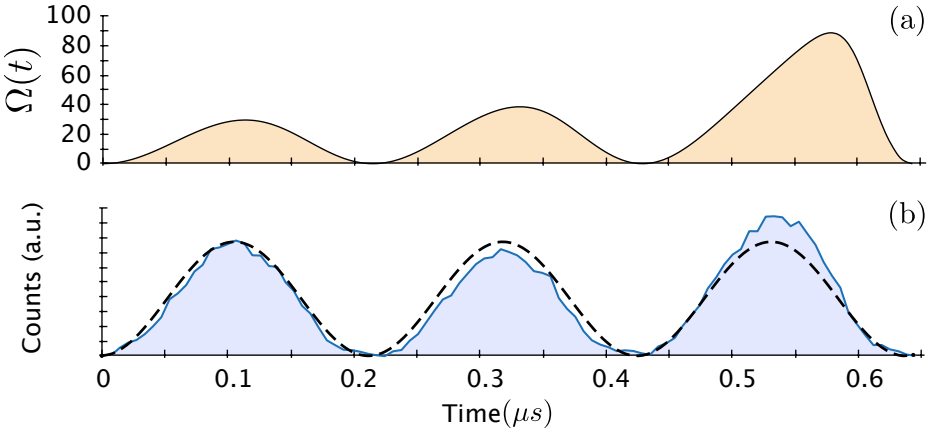


Figure 6.7 (a): Showing the calculated Rabi frequency of the driving pulse needed to produce triple-peak photons. The pulse is calculated for an efficiency of 80% and with atom-cavity parameters as before. (b): The measured clicks on the SPCMs showing the temporal envelope of the triple peak photons, for 7×10^4 detected photons.

between three distinct time bins, i.e. triple-peak photons with a form given by $|\Psi\rangle = \alpha|001\rangle + e^{i\phi_1}\beta|010\rangle + e^{i\phi_2}\gamma|100\rangle$. Fig. 6.7 shows the analytically calculated driving pulse necessary to produce a triple-peak photon with $\alpha = \beta = \gamma = 1/\sqrt{3}$, (that is, with the photon equally distributed over the three time bins), and a histogram of the experimentally measured detector clicks for a stream of non-interfering photons emitted from the cavity, demonstrating the amplitude of the photon wavepackets.

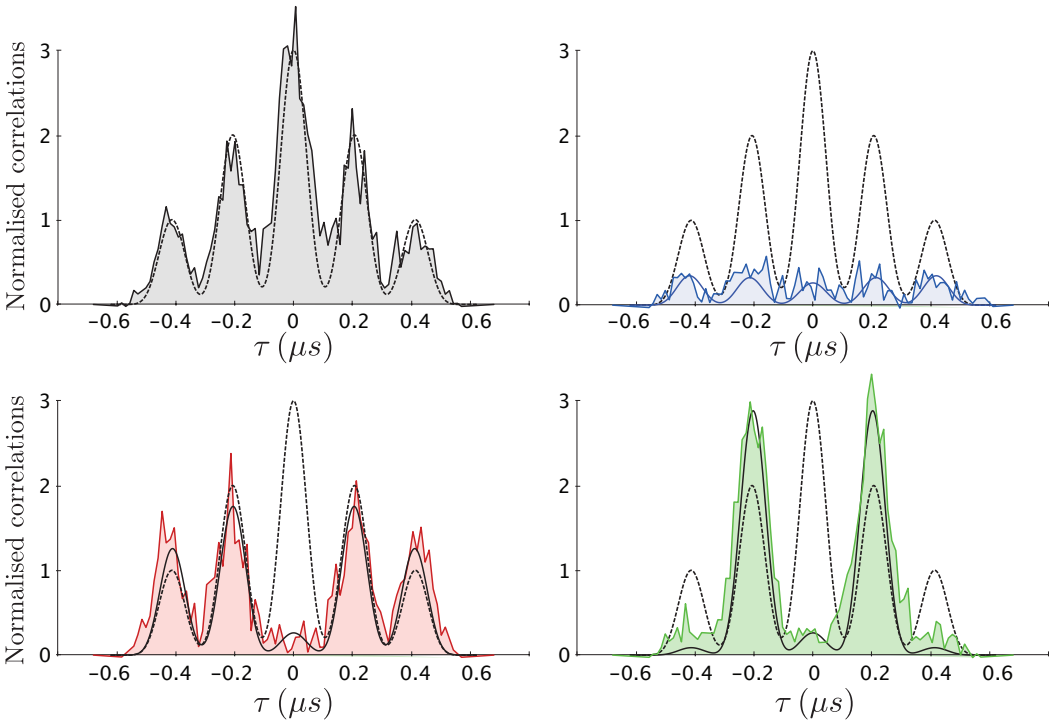


Figure 6.8 Clockwise from top left: Triple peak photon with perpendicular polarisation; parallel polarisation, equal phases throughout; π flip in the central peak; $\pi/2$ in the central peak with a π phase flip in the last peak. In all plots, the dashed line shows the fit for perpendicular polarisation, and the solid line a fit to the respective data. A visibility of $V_{2ph} = 0.78$ is obtained for the perpendicular and parallel polarisations which is impressive given the complexity of the photon shape.

Following the same algorithm outlined in Section 6.2, measurements of the coincidences are taken first for the case of perpendicular and parallel polarisation, with no relative phases applied. These two cases are shown in a the top of Fig. 6.8. The fact that there are now two phases which we can apply means there are further interesting permutations. If, for example, we set $\phi_1 = \pi$ and $\phi_2 = 0$, we can see that as always, all pairs detected in the same time bins will coalesce, all photon pairs detected in adjacent time bins ($\Delta_n = 1$) will behave 'quasi-fermionically', and all pairs detected with a time bin difference of two ($\Delta_n = 2$) will again coalesce. Thus, one expects only to see cross-correlations for photons detected in adjacent time bins. Shown in Fig. 6.8 are the results obtained for exactly this scenario. As is clearly demonstrated, the results impressively agree with the theoretical expectation. Another case which one might like to investigate is where we set $\phi_1 = \pi/2$ and $\phi_2 = \pi$. Adjacent time bins should then have a relative phase difference of $\pi/2$ and those two apart a phase difference of π. The heights of the peaks in the HOM signal should then be even for correlations between bins with a time differences of

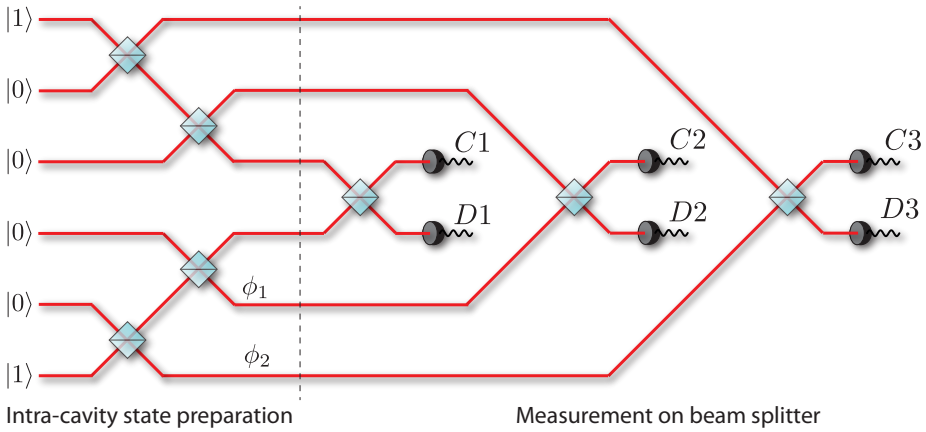


Figure 6.9 Equivalent circuit for the time-resolved two-photon interference of triple peak photons.

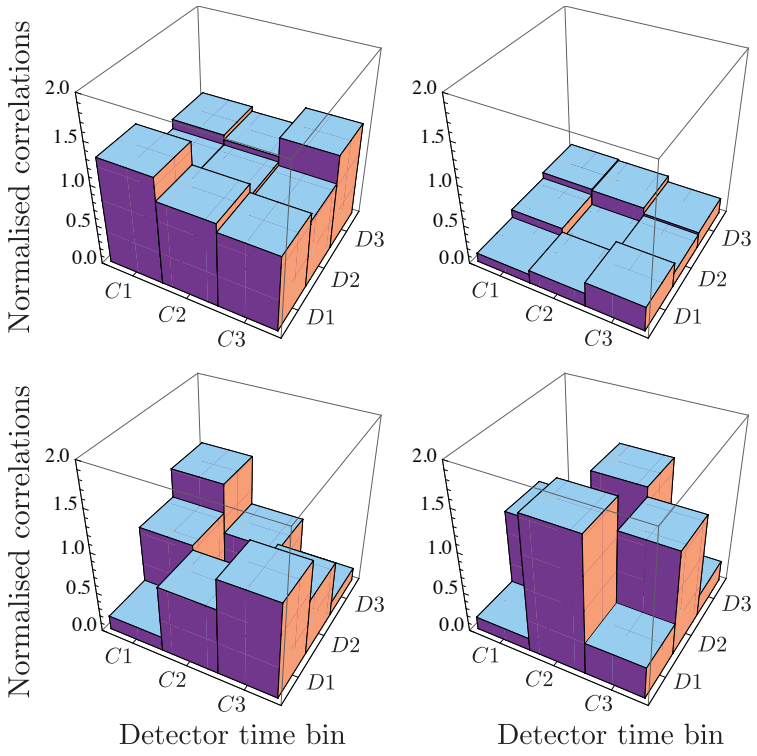


Figure 6.10 Plots showing correlations measured between the detectors for the possible time bin combinations. a) Perpendicular polarisation. b) Parallel polarisation, no phase flip. c) Parallel polarisation, $\phi_1 = 0$, $\phi_2 = \pi$. d) Parallel polarisation, $\phi_1 = \pi/2$, $\phi_2 = 0$.

one and two bins. Again, the results obtained for this case are shown in Fig. 6.8, and impressively agree with the expected behaviour. The solid lines are fits to the data as before: the data are normalised with respected to the number of correlations obtained in the cross-correlation for each case.

The fit lines are then obtained by taking the expected line-shape and calculating the fit only with reference to the coherence time. The obtained values for the coherence time are $T_c = \{0.72, 0.41, 0.65\}\,\mu$s for the three cases, respectively. This spread in values is probably due to imperfect state preparation: this leads to the heights of the peaks deviating from the ideal, which introduces significant artificial error into calculation of the coherence time. Nevertheless, it is apparent that the achieved coherence time is on a par with (and is potentially significantly better than) those obtained for the single- and twin-peak photons after optimising the single-photon source.

Fig. 6.9 shows the equivalent circuit for the production of two of these photons and their interference on a NPBS, following the notation of Fig. 6.5. Again, only two physical detectors are used, but both are represented for each possible time bin. Clearly, the number of correlations one expects to witness between specific time bins is again a function of the relative phase. The results obtained through looking at the correlations between time bins are shown in Fig. 6.10.

6.2.4 Ququads

We can increase the number of time bins further and attempt to produce single photons distributed between four distinct time bins, described by $|\Psi\rangle = \alpha|0001\rangle + e^{i\phi_1}\beta|0010\rangle + e^{i\phi_2}\gamma|0100\rangle + e^{i\phi_3}\epsilon|1000\rangle$. Some preliminary experimental results are shown in Fig. 6.11. As witnessed by the distribution of correlations obtained for the case of perpendicular polarisation, the photon distribution deviates significantly from equality between all four time bins. However, it is still possible to examine the effect of an applied phase. It was chosen to investigate the case with $\phi_1 = \phi_3 = \pi$ and $\phi_2 = 0$, i.e. photons should behave bosonically for $\Delta_n = \{0, 2\}$ and fermionically for $\Delta_n = \{1, 3\}$. The measured time-resolved HOM joint probability distribution and detector time bin cross-correlations are shown for both the perpendicular case and for that described above. It is easily seen that the correlations vary considerably between the two cases, and that the correlations greatly increase for the expected Δ_n.

6.3 Conclusion

In the beginning of this chapter, a proposed scheme for probing the phase of single-photons, based on a 'quantum homodyning' technique and Hong-Ou-Mandel interferometer, was proposed. A theoretical discussion showed that the joint detection probability for photons distributed between distinct time bins should have some clear dependence upon applied phase. It was shown that the experimental results for photons distributed between two time bins agreed excellently with theory, with

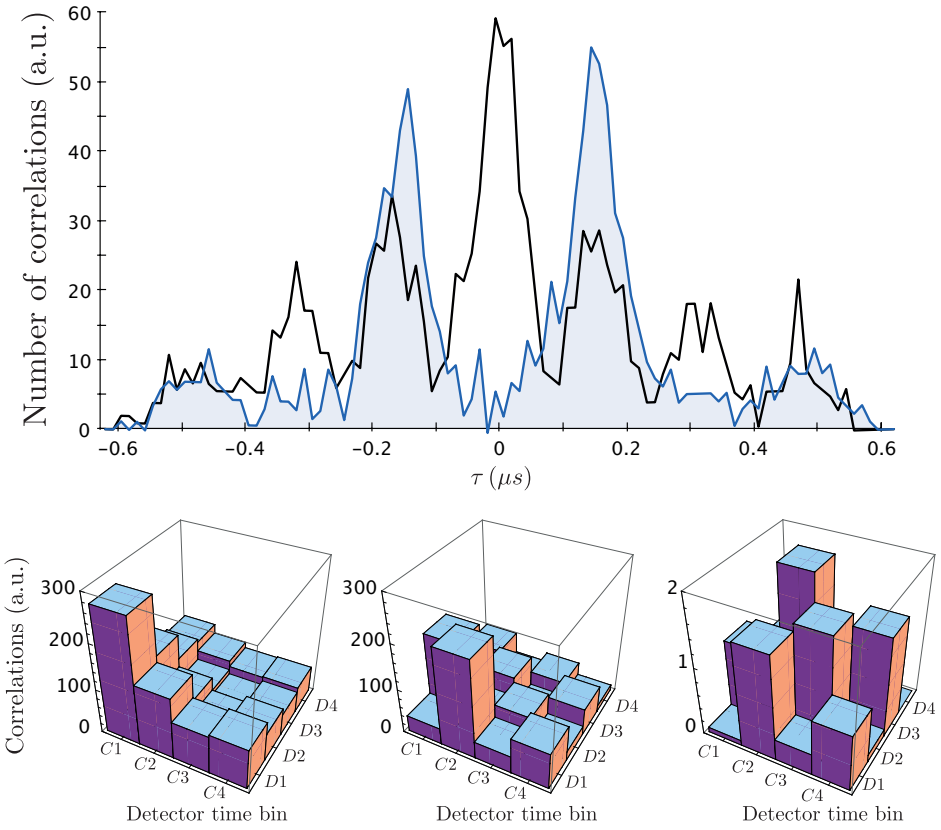


Figure 6.11 Correlations between detectors for quad peak photons distributed between four time bins. Upper plot: standard time-dependent plot of correlations versus detector time delay τ for the perpendicular polarised (black) and parallel polarised with $\phi_1 = \phi_3 = \pi$ (blue) cases. The lower left and middle plots show the detector time-bin correlations for both cases shown above. Right shows the central data, normalised with respect to the number of correlations obtained for the perpendicular case. The expected checker-board pattern becomes obvious, even for correlations between bins separated by greater than the photons' coherence times.

the relative correlations exhibiting the expected $\sin^2(\phi/2)$ dependence and excellent visibility. Together with control over the photon's amplitude, this represents an entirely new method for the creation of arbitrary photonic qubits. Furthermore, the extension of the scheme to allow the preparation of qutrits and ququads was demonstrated, reinforcing the impressive flexibility of the method. This near-complete control over the amplitude and phase of the emitted photons heralds the realisation of the ability to produce arbitrary qudits in the photonic domain, a necessary condition for the realisation of LOQC with single photons.

Chapter 7

Single-Photon Absorption

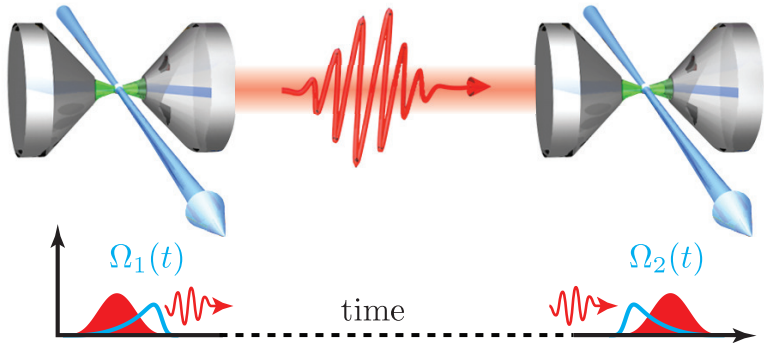


Figure 7.1 The Quantum Internet, showing the state of one atom (stationary qubit) being transferred via a photon (flying qubit) to that of another atom in a separate cavity.

The absorption of single-photons by atom-cavity systems has great relevance to the realisation of a quantum network [16]. However, there exists no general method for determining the optimal control of the classical laser pulses used in the generation and absorption of single photons in these processes, although some work has been done towards this [118, 120, 126–129]. Following on from the single photon generation process described in chapter 5, we here devise an analytical method for finding the control pulse required for the complete absorption of single photons of arbitrary temporal shape $\phi(t)$ impinging on a cavity mirror. We emphasise that this technique applies directly to the implementation of a quantum memory and is pertinent to a variety of cavity-based systems. As will be discussed later, this scheme relates most obviously to mapping Fock-state encoded qubits to atomic states [16, 24], but also very simply extends to other possible superposition states, e.g. photonic time bin or polarisation encoded qubits [22, 27, 130].

This chapter is based on work presented in [131], and contains the following: Section 7.1 describes a formulation of the input-output coupling of an optical cavity

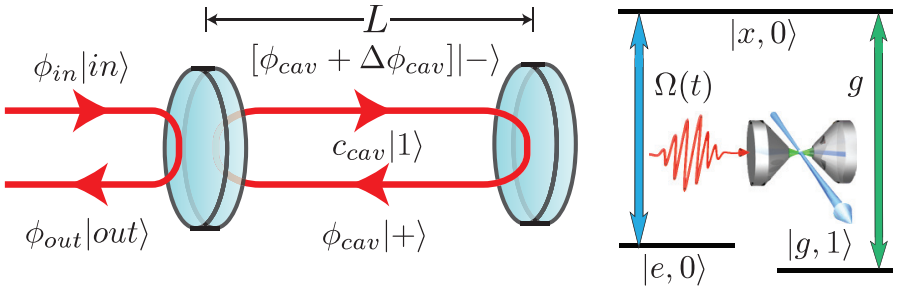


Figure 7.2 The left schematic shows the input-output cavity coupling formulation, whilst the right diagram shows the atomic states $|e\rangle$, $|x\rangle$ and $|g\rangle$ with their respective cavity photon number states $|0\rangle$ and $|1\rangle$. The couplings of the control pulse and cavity are given by $\Omega(t)$ and g respectively.

in the time domain, and extends the atom-cavity coupling found in in the photon shaping chapter. Section 7.2 derives an expression for the Rabi frequency needed to ensure full impedance matching during the absorption of a photon, and section 7.3 discusses the application of this method to some physically realistic photons. Finally, section 7.3.1 discusses the relevance of the technique to the implementation of a quantum memory.

7.1 Input-Output Coupling

Firstly, we shall formulate a brief description of the input-output coupling of an optical cavity in the time domain. Inside the cavity, we assume that the mode spacing is so large that only one single frequency mode is involved, with the probability amplitude $c_{cav}(t)$ for occupying the one-photon Fock state $|1\rangle$ at resonance frequency ω_{cav}. Furthermore, we assume that one cavity mirror has a reflectivity of 100 %, thus ensuring that coupling to the outside field is controlled uniquely by the field reflection and transmission coefficients, r and τ, of the other mirror. It is then very convenient to decompose the cavity mode into submodes $|+\rangle$ and $|-\rangle$, travelling towards and away from this mirror, respectively. In turn, the spatio-temporal representation of the cavity field reads

$$\phi_{cav}(t)|+\rangle + [\phi_{cav}(t) + \Delta\phi_{cav}]|-\rangle, \tag{7.1}$$

with $\phi_{cav}(t)\sqrt{t_r} = c_{cav}(t)$, and $t_r = 2L/c$ the cavity's round-trip time. $\Delta\phi_{cav}$ accounts for any change in $\phi_{cav}(t)$ at the mirror. To properly describe the field outside the cavity, we decompose it also into incoming and outgoing spatio-temporal field modes, with probability amplitudes $\phi_{in}(t + z/c)$ and $\phi_{out}(t - z/c)$ for finding the photon in the $|in\rangle$ and $|out\rangle$ states, respectively. The coupling mirror at $z = 0$ acts

as a beam splitter with the operator

$$a_-^\dagger(ra_+ + \tau a_{in}) + a_{out}^\dagger(\tau a_+ - ra_{in}) \tag{7.2}$$

coupling the four running-wave modes inside and outside the cavity. To relate $c_{cav}(t)$ to the running wave amplitude $\phi_{cav}(t)$, taking $|r| \approx 1 - \kappa t_r$ and $|\tau| = \sqrt{2\kappa t_r}$, we find:

$$\frac{dc_{cav}}{dt} = \frac{\Delta\phi_{cav}\sqrt{t_r}}{t_r} = \Delta\phi_{cav}/\sqrt{t_r}, \tag{7.3}$$

leading to the differential equation

$$\begin{pmatrix} \dot{c}_{cav} \\ \phi_{out} \end{pmatrix} = \begin{pmatrix} -\kappa & \sqrt{2\kappa} \\ \sqrt{2\kappa} & -r \end{pmatrix} \begin{pmatrix} c_{cav} \\ \phi_{in} \end{pmatrix} \tag{7.4}$$

which describes the coupling of a resonant photon into and out of the cavity mode. We emphasise that any deviation from resonance with the cavity mode can be included in time-dependent phase factors of the probability amplitudes. Therefore the above coupling model applies to any case where just one cavity-field mode is involved, using the frequency ω_c of this mode as a carrier. Note that the expansion of this model to both mirrors being transparent is straight forward, but not required for the following analysis.

We can now extend the discussion of the atom-cavity coupling outlined in chapter 5 to incorporate ϕ_{in} and ϕ_{out}. The time evolution of the product states is given by the master equation of the coupled atom-cavity system

$$\begin{pmatrix} \dot{c}_e \\ \dot{c}_x \\ \dot{c}_g \\ \phi_{out} \end{pmatrix} = \begin{pmatrix} 0 & -i\Omega(t)^*/2 & 0 & 0 \\ -i\Omega(t)/2 & -\gamma & -ig & 0 \\ 0 & -ig^* & -\kappa & \sqrt{2\kappa} \\ 0 & 0 & \sqrt{2\kappa} & -r \end{pmatrix} \begin{pmatrix} c_e \\ c_x \\ c_g \\ \phi_{in} \end{pmatrix} \tag{7.5}$$

where all parameters are the same as previously defined.

7.2 Impedance Matching

Our goal is to completely absorb an incoming photon, with its wavepacket given by $\phi_{in}(t)$. Obviously, the condition $\phi_{out}(t) = 0$ must be met at all times to achieve this. We furthermore assume that $r \approx 1$, i.e. the reflectivity of the cavity mirror is nearly one. Using these constraints with Eqn. (7.5), and following on from Eqs. (5.3) and (5.4) we obtain the product

$$\Omega(t)c_e(t) = 2\left[i\dot{c}_x(t) + i\gamma c_x(t) - gc_g(t)\right] \equiv \zeta(t). \tag{7.6}$$

To proceed, we need to consider the initial population of states and the overall continuity of probabilities (by which we mean the excitation is conserved). It is natural to assume that the atom-cavity system is initially prepared in state $|g, 0\rangle$, which lies outside the considered subspace. The photon is completely in the incoming

state $|in\rangle$, i.e. $\int |\phi_{in}(t)|^2 dt = 1$. The portion that couples into the cavity therefore directly populates $|g,1\rangle$, so that the continuity balance yields

$$\int_{-\infty}^{t} [|\phi_{in}(t')|^2 - 2\gamma\rho_{xx}(t')]dt' + \rho_0 = \rho_{gg}(t) + \rho_{xx}(t) + \rho_{ee}(t). \tag{7.7}$$

In order to account for an imperfect state preparation with a small initial population in state $|e,0\rangle$, the offset term ρ_0 has been introduced phenomenologically. The relevance of this term (which is ideally zero) becomes obvious in the following discussion.

Eq. (7.7) now gives a direct analytical expression for ρ_{ee}, and as c_e is real on resonance, we finally obtain

$$\Omega(t) = \frac{\zeta(t)}{\sqrt{\rho_{ee}(t)}} = \frac{2\left[i\dot{c}_x(t) + i\gamma c_x(t) - g c_g(t)\right]}{\sqrt{\rho_{ee}(t)}} \tag{7.8}$$

This is an analytical expression for the Rabi frequency $\Omega(t)$, derived in the same manner as before, but which is now required to achieve full impedance matching over all times and therefore to absorb the incoming photonic wave packet $\phi_{in}(t)$ completely in the atom. Most computer algebra systems (CAS) can be used to obtain a closed expression for $\Omega(t)$ given a functional expression for the incoming photon. Of course, this non-iterative algorithm may also be applied numerically.

7.3 Single-Photon Absorption

We now consider physically realistic photons that are normally restricted to a finite support, i.e. they have a well-defined start time, $t_{start} = 0$ and end time t_{stop}. We also assume they start off smoothly, i.e. with $\phi_{in}(0) = \dot{\phi}_{in}(0) = 0$ (as described in [72]). However, the second derivative might be non-zero at t_{start}, so that Eq. (7.6) yields $\Omega(t_{start})c_e(t_{start}) \neq 0$. To satisfy the latter inequality a small but non-vanishing initial population is required in the state $|e,0\rangle$. In other words, perfect impedance matching with $\rho_0 = 0$ would only be possible with photons of a physically impossible infinite duration.

To illustrate the power of the procedure and the implications of the constraints to the initial population, we now apply the scheme to a couple of typical photon shapes that one may obtain from atom-cavity systems. To this purpose, we consider a cavity with parameters similar to one of our own experimental implementations, with $(g,\kappa,\gamma) = 2\pi \times (15,3,3)\,\mathrm{MHz}$ and a resonator length of $L = 100\,\mu\mathrm{m}$. As a first example, we assume that a symmetric photon with $\phi_{in}(t) \propto \sin^2(\pi t/\tau_{photon})$ impinges on the cavity. For a photon duration of $\tau_{photon} = 3.14\,\mu\mathrm{s}$, Fig. 7.3 shows $\phi_{in}(t)$, $\Omega(t)$ and the probability amplitude of the reflected photon, $\phi_{out}(t)$, as a function of time. The latter is obtained from a numerical solution of Eq. (7.5) for the three cases of (a) an empty cavity, (b) an atom coupled to the cavity initially prepared in $|g,0\rangle$, with $\rho_0 = 0$, and (c) a small fraction of the atomic population initially in state $|e,0\rangle$, with $\rho_0 = 0.5\%$. In all three cases, the Rabi frequency $\Omega(t)$ of

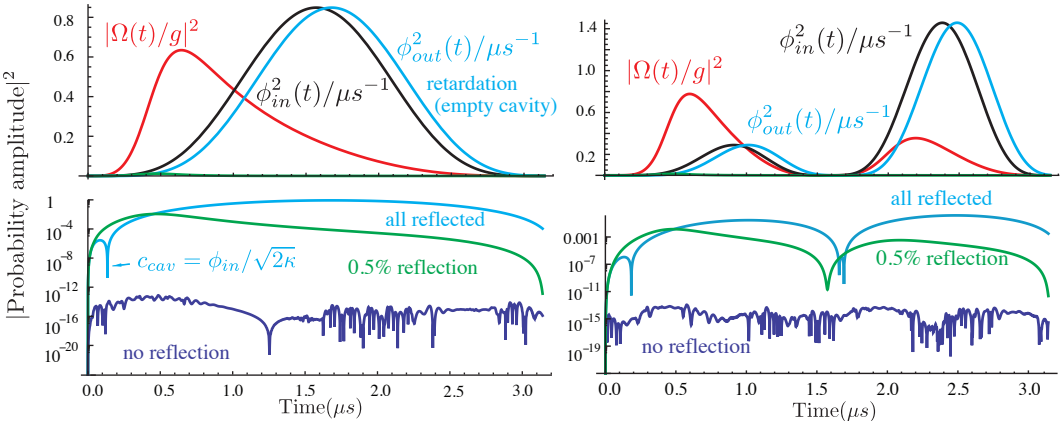


Figure 7.3 Left: A symmetric $\sin^2$ pulse. Black: incoming photon; Light blue: case (a), reflected photon, empty cavity; Green: case (b), reflected photon, system prepared in $|g,0\rangle$; Dark blue: case (c), reflected photon, small initial population of 0.5% in $|e,0\rangle$; Red: Control pulse, derived to match case (c). Right: A twin peak pulse. All traces as as before.

the control pulse is identical. It has been derived analytically assuming a small value of $\rho_0 = 0.5\%$. This choice is arbitrary and only limited by practical considerations, as will be discussed later. From these simulations, it is obvious the photon gets fully reflected if no atom is present (case a), albeit with a slight retardation due to the finite cavity build-up time. Because the direct reflection of the coupling mirror is in phase with the incoming photon and the light from the cavity coupled through that mirror is out-of phase by π, the phase of the reflected photon flips around as soon as $c_{cav}(t) = \phi_{in}(t)/\sqrt{2\kappa}$. This shows up in the logarithmic plot as a sharp kink in $\phi_{out}(t)$ around $t = 0.13\,\mu$s.

The situation changes dramatically if there is an atom coupled to the cavity mode. For instance, with the initial population matching the starting conditions used to derive $\Omega(t)$, i.e. case (c) with $\rho_0 = 0.5\%$, no photon is reflected. The amplitude of $|\phi_{out}(t)|^2$ remains below 10^{-12}, which corresponds to zero within the numerical precision. However, for the more realistic case (b) of the atom-cavity system well prepared in $|g,0\rangle$, the same control pulse is not as efficient, and the photon is reflected off the cavity with an overall probability of 0.5%. This matches the "defect" in the initial state preparation, and can be explained by the finite cavity build-up time leading to an impedance mismatch in the onset of the pulse.

We emphasise that this seemingly small deficiency in the photon absorption might become significant with photons of much shorter duration. For instance, in the extreme case of a photon duration $\tau_{photon} < \kappa^{-1}$, building up the field in the cavity to counterbalance the direct reflection by means of destructive interference is achieved most rapidly without any atom. Any atom in the cavity will act as a sink, removing intra-cavity photons. With an atom present, a possible alternative is to start off with a very strong initial Rabi frequency of the control pulse. This will

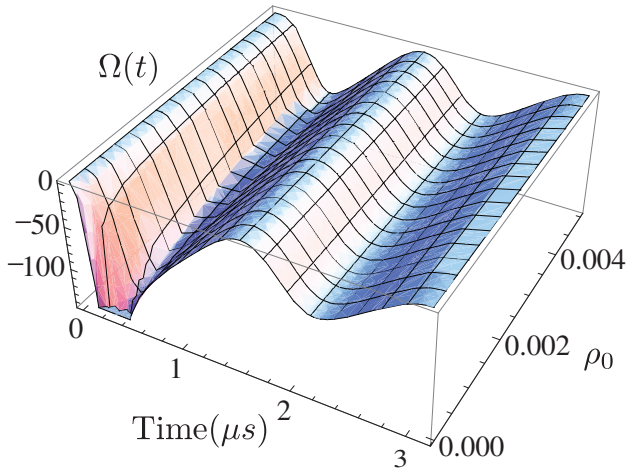


Figure 7.4 Derived Rabi frequency, $\Omega(t)$, as a function of t and ρ_0. In this particular case, the required pulse-shape changes little for values of ρ_0 greater than 0.002.

project the atom-cavity system initially into a dark state, so that the atom does not deplete the cavity mode. Nonetheless, the initial reflection losses would still be as high as for an empty cavity.

Second, we consider a more sophisticated non-symmetric twin-peaked photon impinging onto the cavity, with $\phi_{in}(t) \propto \sin^2(2\pi t/\tau_{photon}) \cos(\pi/2(1-t/\tau_{photon}))$. As in the first example, we simulate the process with a control-pulse Rabi frequency $\Omega(t)$ derived for $\rho_0 = 0.5\%$. From Fig. 7.3, it is obvious the results are the same as before, despite the rather complicated photon shape. This impressively demonstrates the potential of our method, giving one a very simple procedure to derive control-laser pulses for absorbing incoming photons of arbitrary shape.

Finally, we investigate how $\Omega(t)$ changes in the limit $\rho_0 \longrightarrow 0$, which would normally correspond to the initial condition in any implementation. For the twin-peak photons discussed above, Fig. 7.4 shows $\Omega(t)$ for different values of ρ_0. As one would expect from our above discussion of the build-up dynamics, $\Omega(t)$ does not converge to a finite function in the limit $\rho_0 \longrightarrow 0$. Hence for any realistic scenario, one needs to chose ρ_0 to be as small as possible such that a feasible driving pulse shape is obtained. Limits to this are normally the finite laser power and/or the finite bandwidth of the amplitude modulators. For the 'best possible' driving pulse derived in this manner, a numerical simulation starting with the atom-cavity system prepared in $|g, 0\rangle$ then reveals the actual efficiency. In the particular examples discussed here, the photon-reflection losses are comparable to the non-zero ρ_0 used to derive the driving pulse, i.e. at a level below 0.5% which is negligible compared

to the noise affecting current experimental approaches.

7.3.1 Quantum Memory

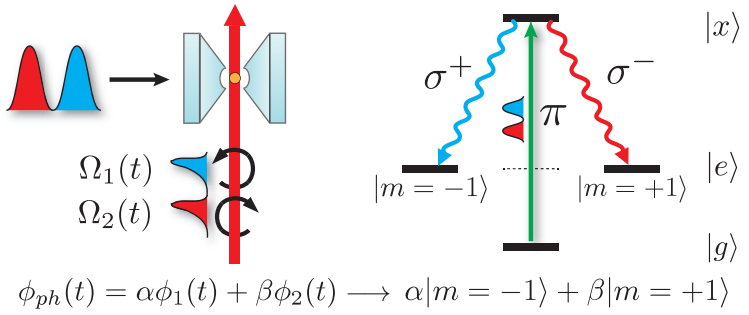


Figure 7.5 Mapping of a photonic time-bin superposition state to a superposition of atomic (spin) states. The left diagram shows a photonic qubit impinging on an atom-cavity system, and the respective driving pulses required in order to map the qubit to the atomic states (right).

We now discuss the application of our scheme to mapping an arbitrary time-bin superposition photonic state [132], $\phi_{ph}(t) = \alpha\phi_1(t) + \beta\phi_2(t)$ to a superposition of atomic spins, $\alpha|m=-1\rangle+\beta|m=+1\rangle$. Assuming a π polarised incoming photon and ϕ_1 and ϕ_2 not overlapping in time, (i.e. they represent two orthogonal field modes), we devise two driving pulses $\Omega_1(t)$ and $\Omega_2(t)$ that map these two field modes into $|m=-1\rangle$ and $|m=+1\rangle$, respectively. As illustrated in Fig. 7.5, the latter can be achieved with $\Omega_1(t)$ and $\Omega_2(t)$ having different circular polarisations. As a simple consequence of the unitarity of the time evolution, successive application of the two driving pulses, together with their respective time bins, results in the desired mapping of photonic to atomic superposition states. We emphasise that the pair of driving pulses only depends on the mode functions $\phi_{1,2}$ describing the two time bins, and not on their relative amplitudes α and β. Further, the three-level systems addressed during the first and second time bin are different from one another, and no cross talk occurs due to the different polarisations of the driving pulses. Hence the numerical simulation depicted in Fig. 7.3 now applies to the two time bins individually, with a specific example of the scheme shown in Fig. 7.6. The plot is calculated using the same values of (g, κ, γ) as before, and demonstrates a storage efficiency of 95.3% with a fidelity of 1. The unit fidelity is a consequence of the fact that the only incoherent process in the model, non-adiabatic excitation and decay to and from the excited state $|x, 0\rangle$, is treated as a loss from the system. Thus it does not contribute any incoherence to the final atomic state superposition, but is incorporated only as a reduction in the efficiency of the mapping.

One could also map a superposition of photonic number states to a pair of atomic states [16, 24]. For instance, $\alpha|0\rangle + \beta|1\rangle$ gets trivially mapped to $\alpha|g\rangle + \beta|e\rangle$; if no

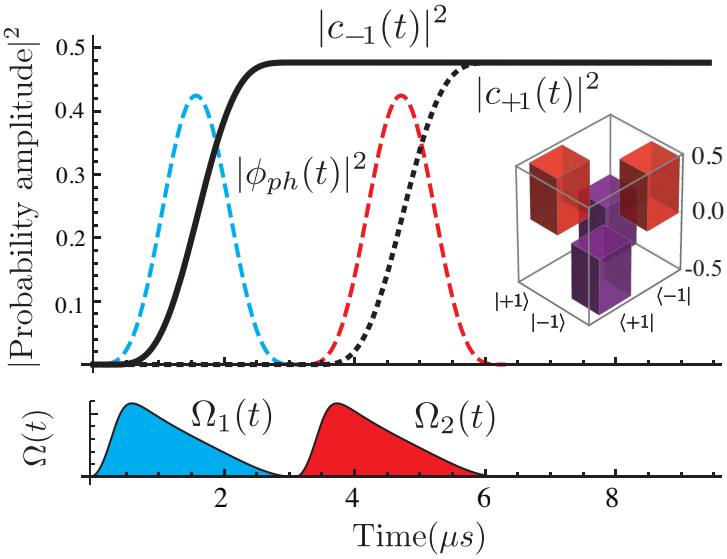


Figure 7.6 Plot demonstrating photon to atom state-mapping utilising the procedure outlined above. The photonic qubit is prepared in the state $\frac{1}{\sqrt{2}}(\phi_1 - \phi_2)$ and mapped onto the atomic spin states $|m = -1\rangle$ and $|m = +1\rangle$. The populations of the atomic states are shown (thick line: $|m = -1\rangle$, thick dotted line: $|m = +1\rangle$), as is the incoming photonic state (thin dashed lines). The two driving pulses are shown below (arb. units), whilst the upper inset shows the atomic state density matrix after the successful absorption of the photon.

photon arrives then the atom remains unaffected (as the atom-cavity system stays in $|g, 0\rangle$), whilst the signed driving pulse assures that a photon arriving in mode $\phi_{ph}(t)$ gets mapped to $|e\rangle$, in the way we depicted in Fig. 7.3. Again, the unitarity of the time evolution assures the accurate mapping of superposition states.

By combining this photon reabsorption scheme with the method for generating tailored photons outlined in [72, 78], we have demonstrated how to calculate analytically the optimal driving pulses needed to produce and absorb arbitrarily shaped single-photons (of finite support) with three level Λ-type atoms in optical cavities; a necessary condition for the implementation of a functioning quantum network. It is expected that this simple analytical method will have significant relevance for those striving to achieve atom-photon state transfer in C-QED experiments, where low losses and high fidelities are of paramount importance.

Chapter 8

Outlook

8.1 Outlook

There are a number of possible future directions which work stemming from the present experiment could take. Given the photon shaping results and photon absorption algorithm presented here, it would seem sensible to try to combine the two in order to implement the basics of a quantum network, with single atoms functioning as memory qubits and single photons as flying qubits. The simplest and most easily obtainable method with which one could demonstrate control over the emission and absorption of photonic qubits would be to utilise one and the same atom in a cavity to both generate and absorb a single photon. Obviously, this would significantly simplify the required experimental set-up in comparison to the requirement for two atom-cavity systems. Fig. 8.1 shows the schematic of a system designed to fulfill this goal. A single photon, emitted from the atom, is sent down a delay line of requisite length and subsequently reflected back toward the cavity. A suitable control pulse should then ensure complete absorption of the wavepacket as it impinges on the cavity. State detection carried out on the atom (possibly in the form of a secondary photon emission) should then inform the experimentalist whether the absorption process has been successful. The described apparatus was set up in the laboratory, but insufficient available time meant that it was not possible to properly investigate its behaviour.

Looking slightly further into the future, the entanglement of two atoms in separate cavities using single photons could be explored. There is currently a second vacuum chamber and atom-trapping apparatus in the laboratory. The addition of an optical cavity to this would open up the possibility of full state mapping between individual atoms. Use of the schemes explored in Chapter 7 would allow direct state mapping, or remote entanglement between atoms could equally be generated through joint measurements on photons [133].

As mentioned in Chapter 1, any realistic quantum network or quantum communication system would have some requirement of qubit storage within the network [36]. One promising candidate for such a task is the storage of photons in

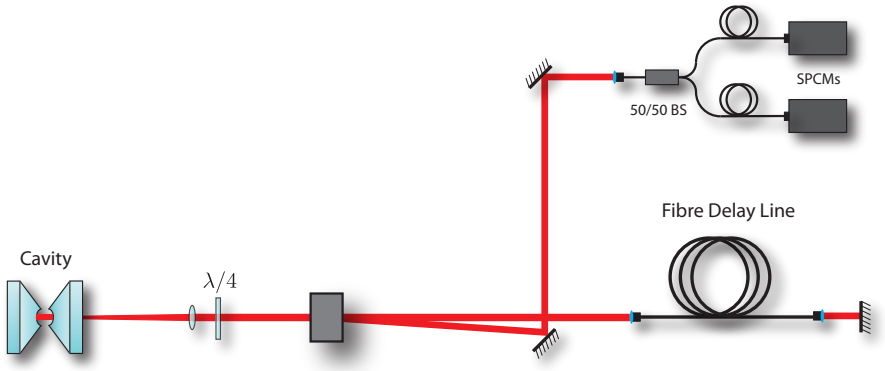


Figure 8.1 A schematic of the set-up proposed for reabsorption. Single photons are emitted from the system and travel down the fiber delay line. The photons are reflected back toward the cavity and are absorbed by the atom via the application of a suitable control pulse. The state of the atom is then detected through a secondary photon emission process, which is sent toward the SPCMs via the use of an AOM-based path switcher.

warm atomic vapour using electro-magnetically induced transparency (EIT). Coherent pulse storage using EIT has been well documented, although true storage of single deterministically produced photons remains to be achieved. If realised, coherence preserving storage of single photons with high efficiency would represent a large step towards viable quantum networking procedures. There is currently an experiment investigating the feasibility of single photon storage within the same laboratory as the photon pistol, and it is hoped that the atom-cavity system and EIT quantum memory could be combined at some stage. Whether the mapping of a photonic qubit onto a dark-state polariton is a phase-coherent interaction, and whether the requisite storage times (μs) and efficiencies can be reached remain open questions.

Alternatively, given the preceding discussion relating to the suitability of the photons for LOQC, integration of the photon pistol with linear optics based components forming rudimentary quantum circuits could prove to be intellectually fecund. The long temporal duration of the generated photons, and the unique control over their properties, mean that domains not accessible with PDC photons might be explored. One potential scheme could implement active feedback during the photon production, that is, modify the phase of a photon during its generation, dependent upon the outcome of particular detection events [125]. Exploring the conjunction of the atom-cavity source with integrated waveguide chips [71] could open up the possibility of implementing quantum circuits and universal quantum gates [69, 103].

What is most certainly clear is that as we transition from a classical information processing paradigm to a quantum one, ultimate control over the quantum systems at our disposal becomes of paramount importance. The atom-cavity system documented in this thesis demonstrates hitherto unrivalled control over the amplitude

and phase of single photons, and hopefully opens new avenues for research.

Appendix A

Photons of Alternating Polarisation

A.1 Photons of Alternating Polarisation

Initial attempts to implement the photon pistol had centered around a scheme previously realised by Wilk et al. [79]. In said scheme photons are produced by driving the atom between alternate $|m_f = +1\rangle, |m_f = -1\rangle$ magnetic sublevels whose degeneracy has been lifted by the addition of a magnetic field. This method provides a number of benefits when compared to the STIRAP process between hyperfine ground states. Firstly, because the atom is simply driven between two Zeeman substates of the same electronic groundstate, no repump time is required to reinitialise the atom cavity system. This has the benefit of increasing the repetition rate of the system, in some case substantially (the repump phase of the experiments outlined above lasts on occasion for as long as the photon production pulse, meaning that the photon production rate could happily be doubled). Secondly, emitted photons will have a well defined polarisation which alternates between subsequent emissions. Not only is this trivially of merit for a Hong-Ou-Mandel interferometer, as subsequent photons always go down the correct delay arm, but it could also be greatly beneficial when producing certain entangled states and superpositions.

Thus, the first attempts at producing single photons were based on the above scheme. The system was characterised by the application of a bias field along the cavity axis, and the scanning of the frequency of the pump beam (polarised perpendicularly to the cavity axis) away from the bare atomic resonance. One expects to see a Lorentzian centred around $\Delta = 0$ arising from the contributions from cycling transitions, whilst at $\Delta = 2\Delta_B$ one expects to see similar peaks corresponding to photon emission arising from the desired Raman resonances. As can be seen in figure A.1, (where the frequency of the pump beam is only scanned in one direction away from resonance), we do seemingly witness the expected behaviour, i.e. there seem to be two clear peaks in the count rates. However, the peaks are not clearly resolved, thus meaning that there is a considerable probability of more than one

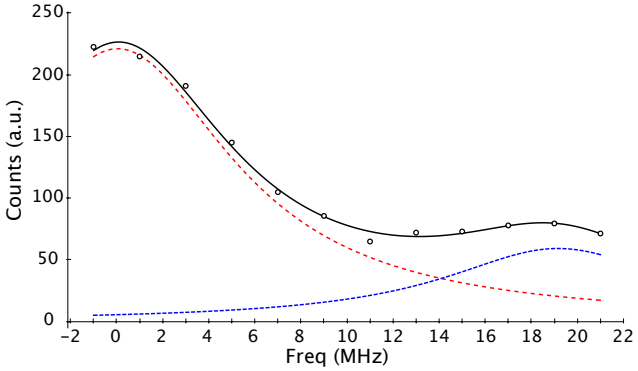


Figure A.1 Showing the count rates for variations in pump frequency for a pump beam of perpendicular polarisation to the cavity axis. The black line is a fit of two Lorentzians (shown individually as the red and blue dotted lines) to the data. The fitted FWFM of the Lorentzians is found to be $\gamma = 12.06\,\text{MHz}$ which agrees very well with value of $\kappa = 12\text{MHz}$ measured through interrogating the optical transmission of the empty cavity. The difference in centres of the peaks corresponds to $\Delta = 19.11\,\text{MHz}$, which corresponds well with the calculated Zeeman shift of $\Delta_B = 10\,\text{MHz}$.

photon emission per atom per pulse.

One could possibly increase the cavity bias field, and ergo, the splitting of the sublevels, to an even greater magnitude: however, problems then arise from mixing of the hyperfine levels in the excited state, leading to a decrease in production efficiency, in addition to the experimental challenge of producing the pump beams.

Bibliography

[1] T. Kuhn, *The structure of scientific revolutions, Chicago, 1962*, Univ. of Chicago Press, 1st edition (1962).

[2] A. Einstein, *Über einen die Erzeugung und Verwandlung des Lichtes betreffenden heuristischen Gesichtspunkt*, Annalen der Physik, **322**, pp. 132–148 (1905).

[3] J. F. Clauser, *Experimental distinction between the quantum and classical field-theoretic predictions for the photoelectric effect*, Physical Review D, **9**, pp. 853–860 (1974).

[4] H. J. Kimble, M. Dagenais, and L. Mandel, *Photon Antibunching in Resonance Fluorescence*, Physical Review Letters, **39**, pp. 691–695 (1977).

[5] P. Grangier, G. Roger, and A. Aspect, *Experimental-Evidence for a Photon Anticorrelation Effect on a Beam Splitter - a New Light on Single-Photon Interferences*, Europhysics Letters, **1**, pp. 173–179 (1986).

[6] C. K. Hong and L. Mandel, *Experimental Realization of a Localized One-Photon State*, Physical Review Letters, **56**, pp. 58–60 (1986).

[7] S. Wiesner, *Conjugate coding*, SIGACT News, **15**, pp. 78–88 (1983).

[8] C. Bennett and G. Brassard, *Quantum cryptography: Public key distribution and coin tossing*, in *Proceedings of IEEE International Conference on Computers Systems and Signal Processing*, pp. 175–179 (1984).

[9] I. Marcikic, A. Lamas-Linares, and C. Kurtsiefer, *Free-space quantum key distribution with entangled photons*, Applied Physics Letters, **89**, p. 101122 (2006).

[10] R. Ursin, F. Tiefenbacher, T. Schmitt-Manderbach, H. Weier, T. Scheidl, M. Lindenthal, B. Blauensteiner, T. Jennewein, J. Perdigues, P. Trojek, B. Ömer, M. Fürst, M. Meyenburg, J. Rarity, Z. Sodnik, C. Barbieri, H. Weinfurter, and A. Zeilinger, *Entanglement-based quantum communication over 144km*, Nature Physics, **3**, pp. 481–486 (2007).

[11] C. Erven, C. Couteau, R. Laflamme, and G. Weihs, *Entangled quantum key distributionover two free-space optical links*, Opt. Express, **16**, pp. 16840–16853 (2008).

[12] D. Stucki, M. Legré, F. Buntschu, B. Clausen, N. Felber, N. Gisin, L. Henzen, P. Junod, G. Litzistorf, P. Monbaron, L. Monat, J.-B. Page, D. Perroud, G. Ribordy, A. Rochas, S. Robyr, J. Tavares, R. Thew, P. Trinkler, S. Ventura, R. Voirol, N. Walenta, and H. Zbinden, *Long-term performance of the SwissQuantum quantum key distribution network in a field environment*, New Journal of Physics, **13**, p. 123001 (2011).

[13] V. Scarani, *The security of practical quantum key distribution*, Rev. Mod. Phys., **81**, pp. 1301–1350 (2009).

[14] N. Gisin, G. Ribordy, W. Tittel, and H. Zbinden, *Quantum Cryptography*, Rev. Mod. Phys., **74**, pp. 145–195 (2002).

[15] H. J. Kimble, *The quantum internet*, Nature, **453**, pp. 1023–1030 (2008).

[16] J. I. Cirac, P. Zoller, H. J. Kimble, and H. Mabuchi, *Quantum State Transfer and Entanglement Distribution among Distant Nodes in a Quantum Network*, Physical Review Letters, **78**, pp. 3221–3224 (1997).

[17] E. M. Purcell, *Spontaneous Emission Probabilities at Radio Frequencies*, Physical Review, **69**, p. 681 (1946).

[18] M. Bayer, T. Reinecke, F. Weidner, A. Larionov, A. McDonald, and A. Forchel, *Inhibition and Enhancement of the Spontaneous Emission of Quantum Dots in Structured Microresonators*, Physical Review Letters, **86**, pp. 3168–3171 (2001).

[19] H. J. Carmichael, *Photon Antibunching and Squeezing for a Single Atom in a Resonant Cavity*, Physical Review Letters, **55**, pp. 2790–2793 (1985).

[20] K. Choi, H. Deng, J. Laurat, and H. Kimble, *Mapping photonic entanglement into and out of a quantum memory*, Nature, **452**, pp. 67–71 (2008).

[21] D. Matsukevich, T. Chaneliere, S. Jenkins, S. Lan, T. Kennedy, and A. Kuzmich, *Entanglement of remote atomic qubits*, Physical Review Letters, **96**, p. 030405 (2006).

[22] T. Wilk, S. C. Webster, A. Kuhn, and G. Rempe, *Single-Atom Single-Photon Quantum Interface*, Science, **317**, p. 488 (2007).

[23] X. Maître, E. Hagley, G. Nogues, C. Wunderlich, P. Goy, M. Brune, J.-M. Raimond, and S. Haroche, *Quantum Memory with a Single Photon in a Cavity*, Physical Review Letters, **79**, pp. 769–772 (1997).

[24] A. Boozer, A. Boca, R. Miller, T. Northup, and H. Kimble, *Reversible State Transfer between Light and a Single Trapped Atom*, Physical Review Letters, **98**, p. 193601 (2007).

[25] N. Piro, F. Rohde, C. Schuck, M. Almendros, J. Huwer, J. Ghosh, A. Haase, M. Hennrich, F. Dubin, and J. Eschner, *Heralded single-photon absorption by a single atom*, Nature Physics, **7**, pp. 17–20 (2010).

[26] M. Mücke, E. Figueroa, J. Bochmann, C. Hahn, K. Murr, S. Ritter, C. J. Villas-Boas, and G. Rempe, *Electromagnetically induced transparency with single atoms in a cavity*, Nature, **465**, pp. 755–758 (2010).

[27] H. P. Specht, C. Nölleke, A. Reiserer, M. Uphoff, E. Figueroa, S. Ritter, and G. Rempe, *A single-atom quantum memory*, Nature, **473**, pp. 190–193 (2011).

[28] A. Fedrizzi, R. Ursin, T. Herbst, M. Nespoli, R. Prevedel, T. Scheidl, F. Tiefenbacher, T. Jennewein, and A. Zeilinger, *High-fidelity transmission of entanglement over a high-loss free-space channel*, Nature Physics, **5**, pp. 389–392 (2009).

[29] X.-M. Jin, J. Ren, B. Yang, Z. Yi, F. Zhou, X. Xu, S. Wang, D. Yang, Y. Hu, and S. Jiang, *Experimental free-space quantum teleportation*, Nature Photonics, **4**, pp. 376–381 (2010).

[30] E. Togan, Y. Chu, A. S. Trifonov, L. Jiang, J. Maze, L. Childress, M. V. G. Dutt, A. S. Sørensen, P. R. Hemmer, A. S. Zibrov, and M. D. Lukin, *Quantum entanglement between an optical photon and a solid-state spin qubit*, Nature, **466**, pp. 730–734 (2010).

[31] S. Ritter, C. Nölleke, C. Hahn, A. Reiserer, A. Neuzner, M. Uphoff, M. Mücke, E. Figueroa, J. Bochmann, and G. Rempe, *An elementary quantum network of single atoms in optical cavities*, Nature, **484**, pp. 195–200 (2012).

[32] N. Sangouard, C. Simon, H. de Riedmatten, and N. Gisin, *Quantum repeaters based on atomic ensembles and linear optics*, Rev. Mod. Phys., **83**, pp. 33–80 (2011).

[33] D. N. Matsukevich, *Quantum State Transfer Between Matter and Light*, Science, **306**, pp. 663–666 (2004).

[34] C. W. Chou, H. De Riedmatten, D. Felinto, S. V. Polyakov, S. J. van Enk, and H. J. Kimble, *Measurement-induced entanglement for excitation stored in remote atomic ensembles*, Nature, **438**, pp. 828–832 (2005).

[35] Z.-S. Yuan, Y.-A. Chen, B. Zhao, S. Chen, J. Schmiedmayer, and J.-W. Pan, *Experimental demonstration of a BDCZ quantum repeater node*, Nature, **454**, pp. 1098–1101 (2008).

[36] M. Himsworth, P. Nisbet, J. Dilley, G. Langfahl-Klabes, and A. Kuhn, *EIT-based quantum memory for single photons from cavity-QED*, Applied Physics B Lasers and Optics, **103**, pp. 579–589 (2011).

[37] U. Schnorrberger, J. D. Thompson, S. Trotzky, R. Pugatch, N. Davidson, S. Kuhr, and I. Bloch, *Electromagnetically Induced Transparency and Light Storage in an Atomic Mott Insulator*, Physical Review Letters, **103**, p. 033003 (2009).

[38] R. Feynman, *Simulating physics with computers*, Int. J. Theor. Phys., **21**, pp. 467–488 (1982).

[39] P. Benioff, *Quantum Mechanical Models of Turing Machines That Dissipate No Energy*, Physical Review Letters, **48**, pp. 1581–1585 (1982).

[40] D. Deutsch, *Quantum theory, the Church-Turing principle and the universal quantum computer*, Royal Society of London Proceedings Series A, **400**, pp. 97–117 (1985).

[41] D. P. DiVincenzo, *Two-bit gates are universal for quantum computation*, Physical Review A, **51**, pp. 1015–1022 (1995).

[42] T. D. Ladd, F. Jelezko, R. Laflamme, Y. Nakamura, C. Monroe, and J. L. O'Brien, *Quantum computers*, Nature, **464**, pp. 45–53 (2010).

[43] D. Deutsch and R. Jozsa, *Rapid Solution of Problems by Quantum Computation*, Proceedings of the Royal Society A: Mathematical, Physical and Engineering Sciences, **439**, pp. 553–558 (1992).

[44] L. Grover, *A fast quantum mechanical algorithm for database search*, in *Proceedings of the 28th Annual ACM Symposium on the Theory of Computing*, pp. 212–219 (1996).

[45] L. K. Grover, *Quantum Computers Can Search Arbitrarily Large Databases by a Single Query*, Physical Review Letters, **79**, pp. 4709–4712 (1997).

[46] P. W. Shor, *Polynomal-time algorithms for prime factorization and discrete logarithms on a quantum computer*, SIAM J. on Comp., pp. 1484–1509 (1997).

[47] L. M. K. Vandersypen, M. Steffen, G. Breyta, C. S. Yannoni, M. H. Sherwood, and I. L. Chuang, *Experimental realization of Shor's quantum factoring algorithm using nuclear magnetic resonance*, Nature, **414**, pp. 883–887 (2001).

[48] B. Lanyon, T. Weinhold, N. Langford, and M. Barbieri, *Experimental demonstration of a compiled version of Shor's algorithm with quantum entanglement*, Physical Review Letters, **99**, p. 250505 (2007).

[49] C.-Y. Lu, D. E. Browne, T. Yang, and J.-W. Pan, *Demonstration of a Compiled Version of Shor's Quantum Factoring Algorithm Using Photonic Qubits*, Phys. Rev. Lett., **99**, p. 250504 (2007).

[50] A. Politi, J. C. F. Matthews, and J. L. O'Brien, *Shor's quantum factoring algorithm on a photonic chip*, Science, **325**, p. 1221 (2009).

[51] J. I. Cirac and P. Zoller, *Quantum Computations with Cold Trapped Ions*, Physical Review Letters, **74**, p. 4091 (1995).

[52] D. Jaksch, J. I. Cirac, P. Zoller, R. Côté, and M. D. Lukin, *Fast Quantum Gates for Neutral Atoms*, Physical Review Letters, **85**, pp. 2208–2211 (2000).

[53] L. Brandt, C. Muldoon, T. Thiele, J. Dong, E. Brainis, and A. Kuhn, *Spatial light modulators for the manipulation of individual atoms*, Applied Physics B Lasers and Optics, **102**, pp. 443–450 (2010).

[54] R. Dumke, M. Volk, T. Müther, F. B. J. Buchkremer, G. Birkl, and W. Ertmer, *Micro-optical Realization of Arrays of Selectively Addressable Dipole Traps: A Scalable Configuration for Quantum Computation with Atomic Qubits*, Physical Review Letters, **89**, p. 097903 (2002).

[55] S. Bergamini, B. Darquié, M. Jones, L. Jacubowiez, A. Browaeys, and P. Grangier, *Holographic generation of microtrap arrays for single atoms by use of a programmable phase modulator*, JOSA B, **21**, pp. 1889–1894 (2004).

[56] J. Clarke and F. K. Wilhelm, *Superconducting quantum bits*, Nature, **453**, pp. 1031–1042 (2008).

[57] C. Monroe, D. M. Meekhof, B. E. King, S. R. Jefferts, W. M. Itano, and D. J. Wineland, *Resolved-Sideband Raman Cooling of a bound atom to the 3D zero-point energy*, Physical Review Letters, **75**, p. 4011 (1995).

[58] D. Leibfried, B. DeMarco, V. Meyer, D. Lucas, M. D. Barrett, J. Britton, W. M. Itano, B. Jelenkovic, C. Langer, T. Rosenbrand, and D. J. Wineland, *Experimental demonstration of a robust, high-fidelity geometric two ion-qubit phase gate*, Nature, **422**, pp. 412–415 (2003).

[59] F. Schmidt-Kaler, H. Häffner, M. Riebe, S. Gulde, G. P. T. Lancaster, T. Deuschle, C. Becher, C. F. Roos, J. Eschner, and R. Blatt, *Realization of the Cirac-Zoller controlled-NOT quantum gate*, Nature, **422**, pp. 408–411 (2003).

[60] H. Häffner, W. Hänsel, C. F. Roos, J. Benhelm, D. Chek-al kar, M. Chwalla, T. Körber, U. D. Rapol, M. Riebe, P. O. Schmidt, C. Becher, O. Gühne, W. Dür, and R. Blatt, *Scalable multiparticle entanglement of trapped ions*, Nature, **438**, pp. 643–646 (2005).

[61] D. Stick, W. K. Hensinger, S. Olmschenk, M. J. Madsen, K. Schwab, and C. Monroe, *Ion trap in a semiconductor chip*, Nature Physics, **2**, pp. 36–39 (2005).

[62] S. A. Schulz, U. Poschinger, F. Ziesel, and F. Schmidt-Kaler, *Sideband cooling and coherent dynamics in a microchip multi-segmented ion trap*, New Journal of Physics, **10**, p. 045007 (2008).

[63] A. Friedenauer, H. Schmitz, J. T. Glueckert, D. Porras, and T. Schaetz, *Simulating a quantum magnet with trapped ions*, Nature Physics, **4**, pp. 757–761 (2008).

[64] R. Blatt and D. Wineland, *Entangled states of trapped atomic ions*, Nature, **453**, pp. 1008–1015 (2008).

[65] R. Blatt and C. F. Roos, *Quantum simulations with trapped ions*, Nature Physics, **8**, pp. 277–284 (2012).

[66] E. Knill, R. Laflamme, and G. J. Milburn, *A scheme for efficient quantum computing with linear optics*, Nature, **409**, pp. 46–52 (2001).

[67] P. Kok, K. Nemoto, T. C. Ralph, J. P. Dowling, and G. J. Milburn, *Linear optical quantum computing with photonic qubits*, Rev. Mod. Phys., **79**, pp. 135–174 (2007).

[68] J. L. O'Brien, A. Furusawa, and J. Vučković, *Photonic quantum technologies*, Nature Photonics, **3**, pp. 687–695 (2009).

[69] A. Politi, M. Cryan, J. G. Rarity, S. Yu, and J. L. O'Brien, *Silica-on-silicon waveguide quantum circuits*, Science, **320**, pp. 646–649 (2008).

[70] J. C. F. Matthews, A. Politi, A. Stefanov, and J. L. O'Brien, *Manipulation of multiphoton entanglement in waveguide quantum circuits*, Nature Photonics, **3**, pp. 346–350 (2009).

[71] B. J. Smith, D. Kundys, N. Thomas-Peter, P. G. R. Smith, and I. A. Walmsley, *Phase-controlled integrated photonic quantum circuits*, Optics Express, **17**, pp. 13516–13525 (2009).

[72] G. S. Vasilev, D. Ljunggren, and A. Kuhn, *Single photons made-to-measure*, New Journal of Physics, **12**, p. 063024 (2010).

[73] A. Kuhn, M. Hennrich, T. Bondo, and G. Rempe, *Controlled Generation of Single Photons from a Strongly Coupled Atom-Cavity System*, Applied Physics B Lasers and Optics, **69**, pp. 373–377 (1999).

[74] M. Hennrich, T. Legero, A. Kuhn, and G. Rempe, *Vacuum-Stimulated Raman Scattering Based on Adiabatic Passage in a High-Finesse Optical Cavity*, Physical Review Letters, **85**, pp. 4872–4875 (2000).

[75] A. Kuhn, M. Hennrich, and G. Rempe, *Deterministic single-photon source for distributed quantum networking*, Physical Review Letters, **89**, p. 067901 (2002).

[76] E. T. Jaynes and F. W. Cummings, *Comparison of Quantum and Semiclassical Radiation Theories with Application to the Beam Maser*, Proc. IEEE, **51**, pp. 89–109 (1963).

[77] M. Hijlkema, B. Weber, H. Specht, S. Webster, A. Kuhn, and G. Rempe, *A single-photon server with just one atom*, Nature Physics, **3**, p. 253 (2007).

[78] P. B. R. Nisbet-Jones, J. Dilley, D. Ljunggren, and A. Kuhn, *Highly efficient source for indistinguishable single photons of controlled shape*, New Journal of Physics, **13**, p. 3036 (2011).

[79] T. Wilk, S. Webster, H. Specht, G. Rempe, and A. Kuhn, *Polarization-controlled single photons*, Physical Review Letters (2007).

[80] E. Raab, M. Prentiss, A. Cable, S. Chu, and D. E. Pritchard, *Trapping of Neutral Sodium Atoms with Radiation Pressure*, Physical Review Letters, **59**, p. 2631 (1987).

[81] C. J. Foot, *Atomic Physics (Oxford Master Series in Atomic, Optical and Laser Physics)*, Oxford University Press, USA, 1 edition (2005).

[82] S. Chu, L. Hollberg, J. Bjorkholm, and A. Cable, *Three-dimensional viscous confinement and cooling of atoms by resonance radiation pressure*, Physical Review Letters, **55**, p. 48 (1985).

[83] M. Meucci, E. Mariotti, and P. Bicchi, *Light-Induced Atom Desorption*, Europhysics Letters, **25**, pp. 639–643 (1994).

[84] E. Mariotti, M. Meucci, P. Bicchi, C. Marinelli, and L. Moi, *An efficient photo-atom source*, Optics Communications, **134**, pp. 121–126 (1997).

[85] P. Nisbet-Jones, *Shaping Single Photons*, Ph.D. thesis, University of Oxford.

[86] R. H. Brown and R. Q. Twiss, *A test of a new type of stellar interferometer on Sirius*, Nature, **178**, pp. 1046–1448 (1956).

[87] R. H. Brown and R. Q. Twiss, *Correlation between Photons in two Coherent Beams of Light*, Nature, **177**, pp. 27–29 (1956).

[88] B. L. Morgan and L. Mandel, *Measurement of photon bunching in a thermal light beam*, Physical Review Letters, **16**, pp. 1012–1015 (1966).

[89] R. Short and L. Mandel, *Observation of sub-Poissonian photon statistics*, Physical Review Letters, **51**, pp. 384–387 (1983).

[90] D. Walls, *Squeezed States of Light*, Nature, **306**, pp. 141–146 (1983).

[91] A. Kuhn, M. Hennrich, and G. Rempe, *A Reply to the Comment by Harry J. Kimble*, Physical Review Letters, **90**, p. 249802 (2003).

[92] H. J. Kimble, *Comment on "Deterministic Single-Photon Source for Distributed Quantum Networking"*, Physical Review Letters, **90**, p. 249801 (2003).

[93] M. Hennrich, T. Legero, A. Kuhn, and G. Rempe, *Photon statistics of a non-stationary periodically driven single-photon source*, New Journal of Physics, **6**, p. 86 (2004).

[94] C. K. Hong, Z. Y. Ou, and L. Mandel, *Measurement of subpicosecond time intervals between two photons by interference*, Physical Review Letters, **59**, pp. 2044–2046 (1987).

[95] C. Santori, D. Fattal, J. Vu vckovi c, G. S. Solomon, and Y. Yamamoto, *Indistinguishable photons from a single-photon device*, Nature, **419**, pp. 594–597 (2002).

[96] T. Legero, T. Wilk, M. Hennrich, G. Rempe, and A. Kuhn, *Quantum beat of two single photons*, Physical Review Letters, **93**, p. 070503 (2004).

[97] D. L. Moehring, P. Maunz, S. Olmschenk, K. C. Younge, D. N. Matsukevich, L.-M. Duan, and C. Monroe, *Entanglement of single-atom quantum bits at a distance*, Nature, **449**, pp. 68–U48 (2007).

[98] J. Beugnon, M. P. A. Jones, J. Dingjan, B. Darquié, G. Messin, A. Browaeys, and P. Grangier, *Quantum interference between two single photons emitted by independently trapped atoms*, Nature, **440**, pp. 779–782 (2006).

[99] A. Sipahigil, M. Goldman, E. Togan, Y. Chu, M. Markham, D. Twitchen, A. Zibrov, A. Kubanek, and M. Lukin, *Quantum Interference of Single Photons from Remote Nitrogen-Vacancy Centers in Diamond*, Physical Review Letters, **108**, p. 143601 (2012).

[100] A. Kiraz, M. Ehrl, T. Hellerer, Ö. Müstecaploğlu, C. Bräuchle, and A. Zumbusch, *Indistinguishable Photons from a Single Molecule*, Physical Review Letters, **94**, p. 223602 (2005).

[101] S. V. Polyakov, A. Muller, E. B. Flagg, A. Ling, N. Borjemscaia, E. Van Keuren, A. Migdall, and G. S. Solomon, *Coalescence of Single Photons Emitted by Disparate Single-Photon Sources: The Example of InAs Quantum Dots and Parametric Down-Conversion Sources.*, Physical Review Letters, **107**, pp. 157402–157402 (2011).

[102] J. L. O'Brien, G. J. Pryde, A. G. White, T. C. Ralph, and D. Branning, *Demonstration of an all-optical quantum controlled-NOT gate*, Nature, **426**, pp. 264–267 (2003).

[103] P. J. Shadbolt, M. R. Verde, A. Peruzzo, A. Politi, A. Laing, M. Lobino, J. C. F. Matthews, M. G. Thompson, and J. L. O'Brien, *Generating, manipulating and measuring entanglement and mixture with a reconfigurable photonic circuit*, Nature Photonics, pp. 1–5 (2011).

[104] T. Legero, T. Wilk, A. Kuhn, and G. Rempe, *Time-Resolved Two-Photon Quantum Interference*, Applied Physics B Lasers and Optics, **77**, pp. 797–802 (2003).

[105] T. Legero, T. Wilk, A. Kuhn, and G. Rempe, *Characterization of single photons using two-photon interference*, Advances In Atomic, Molecular, and Optical Physics, **53**, pp. 253–289 (2006).

[106] A. Kuhn and D. Ljunggren, *Cavity-based single-photon sources*, Contemporary Physics, **51**, pp. 289–313 (2010).

[107] S. Gerber, D. Rotter, M. Hennrich, R. Blatt, F. Rohde, C. Schuck, M. Almendros, R. Gehr, F. Dubin, and J. Eschner, *Quantum interference from remotely trapped ions*, New Journal of Physics, **11**, p. 013032 (2009).

[108] A. Laing, A. Peruzzo, A. Politi, M. R. Verde, M. Halder, T. C. Ralph, M. G. Thompson, and J. L. O'Brien, *High-fidelity operation of quantum photonic circuits*, Appl. Phys. Lett., **97**, p. 211109 (2010).

[109] P. P. Rohde, T. C. Ralph, and M. A. Nielsen, *Optimal photons for quantum information processing*, Physical Review A, **72**, p. 052332 (2005).

[110] M. Bellini, F. Marin, S. Viciani, A. Zavatta, and F. T. Arecchi, *Nonlocal Pulse Shaping with Entangled Photon Pairs*, Phys. Rev. Lett., **90**, p. 043602 (2003).

[111] A. Pe'er, B. Dayan, A. A. Friesem, and Y. Silberberg, *Temporal Shaping of Entangled Photons*, Phys. Rev. Lett., **94**, p. 073601 (2005).

[112] K. G. Köprülü, Y.-P. Huang, G. A. Barbosa, and P. Kumar, *Lossless single-photon shaping via heralding*, Opt. Lett., **36**, pp. 1674–1676 (2011).

[113] M. T. Rakher, L. Ma, M. Davanço, O. Slattery, X. Tang, and K. Srinivasan, *Simultaneous Wavelength Translation and Amplitude Modulation of Single Photons from a Quantum Dot*, Phys. Rev. Lett., **107**, p. 083602 (2011).

[114] M. T. Rakher and K. Srinivasan, *Subnanosecond electro-optic modulation of triggered single photons from a quantum dot*, Applied Physics Letters, **98**, 211103 (2011).

[115] H. G. Barros, A. Stute, T. E. Northup, C. Russo, P. O. Schmidt, and R. Blatt, *Deterministic single-photon source from a single ion*, New Journal of Physics, **11**, p. 103004 (2009).

[116] M. Keller, B. Lange, K. Hayasaka, W. Lange, and H. Walther, *A calcium ion in a cavity as a controlled single-photon source*, New Journal of Physics, **6**, p. 95 (2004).

[117] M. P. A. Branderhorst, P. Londero, P. Wasylczyk, C. Brif, R. L. Kosut, H. Rabitz, and I. A. Walmsley, *Coherent Control of Decoherence*, Science, **320**, pp. 638–643 (2008).

[118] M. Keller, B. Lange, K. Hayasaka, W. Lange, and H. Walther, *Continuous generation of single photons with controlled waveform in an ion-trap cavity system*, Nature, **431**, pp. 1075–1078 (2004).

[119] I. Novikova, N. B. Phillips, and A. V. Gorshkov, *Optimal light storage with full pulse-shape control*, Physical Review A, **78**, p. 021802 (2008).

[120] G. S. Vasilev, A. Kuhn, and N. V. Vitanov, *Optimum pulse shapes for stimulated Raman adiabatic passage*, Physical Review A, **80**, p. 13417 (2009).

[121] H. P. Specht, J. Bochmann, M. Muecke, B. Weber, E. Figueroa, D. L. Moehring, and G. Rempe, *Phase shaping of single-photon wave packets*, Nature Photonics, **3**, pp. 469–472 (2009).

[122] P. Kolchin, C. Belthangady, S. Du, G. Y. Yin, and S. E. Harris, *Electro-Optic Modulation of Single Photons*, Physical Review Letters, **101**, p. 103601 (2008).

[123] H. Becker, K. Schmid, W. Dultz, H. Roskos, and W. Martienssen, *Photons with additional inner degree of freedom*, in *Quantum Electronics Conference, 2004. (IQEC). International*, pp. 461–462 (2004).

[124] W. Wasilewski, P. Kolenderski, and R. Frankowski, *Spectral Density Matrix of a Single Photon Measured*, Phys. Rev. Lett., **99**, p. 123601 (2007).

[125] P. B. R. Nisbet-Jones, J. Dilley, A. Holleczek, O. Barter, and A. Kuhn, *Quantum Homodyning of Photonic Qubits, Qutrits and Ququads Emitted on Demand from an Atomic Source*, arXiv.org, **quant-ph** (2012).

[126] C. Santori, D. Fattal, and Y. Yamamoto, *Single-photon Devices and Applications*, Wiley-VCH (2010).

[127] M. Fleischhauer, S. Yelin, and M. D. Lukin, *How to trap photons? Storing single-photon quantum states in collective atomic excitations*, Optics Communications, **179**, pp. 395–410 (2000).

[128] A. Gorshkov, A. André, M. Lukin, and A. Sørensen, *Photon storage in -type optically dense atomic media. I. Cavity model*, Physical Review A, **76**, p. 033804 (2007).

[129] W. Yao, R.-B. Liu, and L. Sham, *Theory of Control of the Spin-Photon Interface for Quantum Networks*, Physical Review Letters, **95**, p. 030504 (2005).

[130] B. Sun, M. S. Chekhova, and L. You, *Atom-photon entanglement generation and distribution*, Physical Review A, **69**, p. 042316 (2004).

[131] J. Dilley, P. Nisbet-Jones, B. W. Shore, and A. Kuhn, *Single-photon absorption in coupled atom-cavity systems*, Physical Review A, **85**, p. 23834 (2012).

[132] I. Marcikic, H. De Riedmatten, W. Tittel, V. Scarani, H. Zbinden, and N. Gisin, *Time-bin entangled qubits for quantum communication created by femtosecond pulses*, Physical Review A, **66**, p. 062308 (2002).

[133] S. Olmschenk, D. N. Matsukevich, P. Maunz, D. Hayes, L.-M. Duan, and C. Monroe, *Quantum Teleportation Between Distant Matter Qubits*, Science, **323**, pp. 486–489 (2009).